Rochester Institute of Technology

RIT Digital Institutional Repository

8-9-2024

Design and Implementation of a Modular, Standalone Microfluidic Flow Control Platform for Cell Culture Applications

Meng-Chun Hsu
mh4060@rit.edu

R·I·T

Design and Implementation of a Modular, Standalone Microfluidic Flow Control Platform for Cell Culture Applications

by

Meng-Chun Hsu

A dissertation submitted in partial fulfillment of the requirements
for the degree of Doctorate of Philosophy in Microsystems Engineering

Microsystems Engineering Program
Kate Gleason College of Engineering

Rochester Institute of Technology
Rochester, New York
August 9, 2024

**Design and Implementation of a Modular, Standalone Microfluidic Flow Control Platform
for Cell Culture Applications**
by
Meng-Chun Hsu

Committee Approval:

We, the undersigned committee members, certify that we have advised and/or supervised the candidate on the work described in this dissertation. We further certify that we have reviewed the dissertation manuscript and approve it in partial fulfillment of the requirements of the degree of Doctor of Philosophy in Microsystems Engineering.

_____

Dr. Vinay Abhyankar   Date
Director, Biomedical and Chemical Engineering Program

_____

Dr. Steven Day   Date
Professor, Biomedical Engineering

_____

Dr. Robert Carter   Date
Associate Department Head, Mechanical Engineering

_____

Dr. Michael Schertzer   Date
Associate Professor, Mechanical Engineering

_____

Dr. Xudong Zheng
Associate Professor, Mechanical Engineering   Date

Certified by:

_____

Dr. Stefan Preble   Date
Director, Microsystems Engineering Program

_____

Dr. Doreen Edwards   Date
Dean, Kate Gleason College of Engineering

ABSTRACT
Kate Gleason College of Engineering
Rochester Institute of Technology

Degree: Doctor of Philosophy   **Program**: Microsystems Engineering

Authors Name: Meng-Chun Hsu

Advisors Name: Vinay V. Abhyankar

Dissertation Title: Design and Implementation of a Modular, Standalone Microfluidic Flow

Control Platform for Cell Culture Applications

Microfluidics, a technology of manipulating small quantities of fluids (0.1-10 µL), has drawn interest as an emerging platform for biomedical and chemical applications since its debut due to several advantages, including better precision in flow rate control, smaller required sample sizes, lower costs of analyses, and shorter turnaround times. Well-defined fluid flows are the hallmark feature of microfluidic culture systems and enable precise control over biophysical and biochemical cues at the cellular scale. One key demand for microfluidics is to control the delivered fluid flows to downstream applications. This is generally achieved via two major components – valves and pumps. Valves provide the essential flow rectifications for microfluidics, and pumps enable the necessary driving of working fluids in microfluidic systems. My dissertation introduces a passive, one-of-a-kind, in-line magnetic microvalve and a tunable, stand-alone pneumatic pump that features a 3D-printed micro-pressure regulator (µPR) to address the demand for an accessible, plug-and-play flow control platform (valving and pumping).

Valves for microfluidics are typically achieved via commercial check valves, which often suffer from leakage flows when encountering low backpressure. A one-of-a-kind in-line one-way passive valve was created via a biocompatible magnetic nanocomposite microcapsule to target the low-pressure/low-flow regime. The microcapsule features a magnetic nanocomposite core with Fe_3O_4 nanoparticles immersed in polyethylene-glycol (PEG) encapsulated by a biocompatible parylene-C shell.

Pumping fluids for microfluidics is generally achieved using displacement-based (e.g., syringe or peristaltic pumps) or pressure-controlled techniques that provide numerous perfusion options, including constant, ramped, and pulsed flows. However, it can be challenging to integrate these large form-factor devices and accompanying peripherals into incubators or other confined environments. Since microfluidic culture studies are primarily carried out under constant perfusion conditions and more complex flow capabilities are often unused, there is a need for a simplified flow control platform that provides standard perfusion capabilities and can be easily integrated into incubated environments. My dissertation introduces a tunable, 3D printed micro pressure regulator (µPR) and shows that it can provide robust flow control capabilities when combined with a high-pressured source to support microfluidic applications. This system is shown to (i) demonstrate a tunable outlet pressure range relevant for microfluidic applications (1–10 kPa), (ii) highlight dynamic control capabilities in a microfluidic network, (iii) and maintain human umbilical vein endothelial cells (HUVECs) in a multi-compartment culture device under continuous perfusion conditions.

ACKNOWLEDGMENTS

I thank my advisor, Dr. Vinay Abhyankar, for his guidance, support, and patience throughout my study. His insightful feedbacks and expertise have been invaluable in this dissertation. I am also very grateful to the members of my committee, Dr. Steven Day, Dr. Schertzer, and Dr. Carter, for their constructive criticism and suggestions.

I thank my family and friends, especially my parents for their consistent support.

I thank my brother for always being there for me during the highs and lows of this journey.

I would also like to thank my lab members and colleagues Neil, Mehran, Poorya, Dinindu, Sami, Nuzhet, Farzad, Jing, who have helped me so much during this journey.

Special thanks to my former post-doctoral fellows Dr. Ahmed Alfadhel and Dr. Arpys Arevelao for their camaraderie and for creating a stimulating and collaborative environment.

List of publications

First Authored Peer-reviewed Journal Publications (2)

[1] **M. C. Hsu**, A. Alfadhel, F. Forouzandeh, and D. A. Borkholder, "Biocompatible magnetic nanocomposite microcapsules as microfluidic one-way diffusion blocking valves with ultra-low opening pressure," Mater Des, vol. 150, no. 5, pp. 86–93, Jul. 2018, doi: 10.1016/j.matdes.2018.04.024.

[2] **M. C. Hsu**, M. Mansouri, S. Larson, I. Joshi, A. Ahmed, D. A. Borkholder, and V. V. Abhyankar, "A miniaturized 3D printed pressure regulator (µPR) for microfluidic cell culture applications," Sci Rep, vol. 12, no. 1, Dec. 2022, doi: 10.1038/s41598-022-15087-9.

Co-Authored Peer-reviewed Journal Publications (2)

[1] A. Ahmed, I. Joshi, M. Mansouri, N. Ahamad, **M. C. Hsu**, T. Gaborski, V. V. Abhyankar, "Engineering fiber anisotropy within natural collagen hydrogels," Am J Physiol Cell Physiol, vol. 320, no. 6, pp. C1112–C1124, Jun. 2021, doi: 10.1152/AJPCELL.00036.2021.

[2] F. Forouzandeh, N. N. Ahamed, **M. C. Hsu**, J. P. Walton, R. D. Frisina, and D. A. Borkholder, "A 3D-printed modular microreservoir for drug delivery," Micromachines (Basel), vol. 11, no. 7, 2020, doi: 10.3390/mi11070648.

First Authored Conference Presentations (4)

[1] **M. C. Hsu**, A. Alfadhel, F. Forouzandeh and D. A. Borkholder, "Biocompatible Magnetic Nanocomposite Microcapsules as Highly Customizable Microfluidic One-way Diffusion Blocking Valves," in Association for Research in Otolaryngology, San Diego, 2018.

[2] **M. C. Hsu**, A. Alfadhel, F. Forouzandeh and D. A. Borkholder, "A Passive Microfluidic One-Way Valve with Diffusion Blocking Capability and Ultra-Low Opening Pressure," in Advanced Functional Materials, Los Angeles, 2017.

[3] **M. C. Hsu**, N. Ahamad and V. V. Abhyankar, "A Modular, Miniaturized Pressure Regulator for Microfluidic Flow Control," in Biomedical Engineering Society, Orlando, FL, 2021.

[4] **M. C. Hsu**, M. Mansouri and V. V. Abhyankar, "A Reconfigurable Tissue Barrier Platform with On-Demand Flow and TEER Measurement Capability," in Microphysiological Systems World Summit, Berlin, Germany, 2023.

Patent (1)
[1] A. Alfadhel, **M. C. Hsu** and D. A. Borkholder, "Capsule, in-line magnetic valve system and method". U.S Patent US11035498B2, 15 06 2021

Chapter 1

Introduction

1.1 Overview of Microfluidics Platform for Cell Culture Applications

Microfluidics, a technology of manipulating small quantities of fluids (0.1-10 µL), has drawn interest as an emerging platform for biomedical and chemical applications since its debut due to several advantages, including better precision in flow rate control, smaller required sample sizes, lower costs of analyses, and shorter turnaround times [1], [2], [3], [4]. Despite being granted with these benefits, microfluidic-based solutions merely see commercial prevalence due to the lack of accessible platforms, the inconvenience of customized fabrication and implementation, difficulties accommodating applications, and initiation costs of setups [2], [5], [6].

One key demand for microfluidics is to control the delivered fluid flows to downstream applications. This is generally achieved via two major components – valves and pumps. Valves provide the essential flow rectifications for microfluidics, and pumps enable the necessary driving of working fluids in microfluidic systems. In **Chapter 1**, the current state of valves and pumps for microfluidic cell culture platforms will be reviewed in detail, followed by a discussion of mobile, battery-less technologies that enable microfluidic-based cell culture applications.

1.2 Valving in Microfluidic Applications

Valving is commonly achieved via powered (active) or powerless (passive) actuations [7], [8]. Among these, active and passive valves can be further categorized via actuation mechanisms. Active valves enable functions such as flow regulations [9], [10], [11], on/off switching [12], and sealing of reagents or chemicals [13], [14]. State-of-the-art active valves commonly employ mechanisms including magnetic[15], [16], [17], electric [18], [19], piezoelectric[20], [21], [22], [23], [24], [25], thermal [26], [27], and chemical[28], [29], [30], [31]. When power is limited or users prefer a more autonomous control with less demand in

maneuverability, passive valves are usually deployed to perform flow directionality or flow rate rectification[8]. Such valving is often achieved based on the built-in preferential route of flow rates based on channel geometrical design, surface modifications, and capillary-driven designs [32]. Passive valves can be categorized by designs with or without moving mechanical parts [33].

1.3 Pumping in microfluidic applications

When searching for a pump for microfluidic cell culture, we look to balance the ease of use, accessibility, and precision of fluidic control. Juggling between these benefits remains an essence when introducing actuation mechanisms into the fluidic driving system. For instance, researchers have explored different powered actuation methods for miniaturized precise proportional fluid control [3]. These actuation methods include electromechanical [34], electrostatic [35], electromagnetic [36], piezoelectric [37], and thermal-based [38]. The necessary power sources, and design-specific fabrication processes, along with the associated complexities and costs make these devices challenging to be widely implemented. On the other end of the spectrum, researchers shed light on passive mechanisms to realize portable and user-friendly fluidic driving. Capillary-force-based, built-in-pressure-driven, and gravity-driven are among the most common passive pumping mechanisms designated for microfluidic platforms [39], [40], [41]. Despite the lower costs and ease of use, passive pumping mechanisms are usually designated for applications tolerant to flow instabilities as they often lack control over the fluid driving rates [41], [42]. Moreover, capillary-force-based devices generally suffer from backflows [43]; gravity-driven and typical built-in-pneumatic-pressured pumps exhibit descending flow rates during pumping. These limitations make them unsuitable for long-term usage that requires continuous perfusion. Since attaining precise control of fluidic driving pressure enables proportionally-controlled liquid flow rates applicable for a variety of fluidic applications, i.e. microfluidic cell culture of HUVECs [44], [45], [46], [47], [48], [49], we look to create an accessible, power-free, miniature system with low-complexity fabrication processes while possessing tunable fluidic control capability. [50], [51]

Pumps provide the necessary driving force for working fluids in microfluidic systems. Precise and tunable pumping for microfluidic applications is commonly achieved with displacement-based (e.g., syringe or peristaltic pumps) or pressure-controlled techniques. However, it can be challenging to integrate these large form-factor devices and accompanying peripherals into confined environments, such as incubators. Thus, miniaturized approaches to simplify the pumping process have also been widely explored. For example, a commercial palm-top refillable iPrecio infusion pump was used to maintain cells in culture. However, the pump was expensive and could not be customized. Alternatively, passive pumping, including hydrostatic and surface tension-based methods, is low-cost and easy to use but lacks long-term stability, deeming them unsuitable for microfluidic culturing applications (> 24 h). Microelectromechanical systems (MEMS) approaches have also been used to create microfabricated pumps. Although these micropumps can provide the long-term control required for lab-on-chip applications, the complexity of the fabrication procedures can make customization and implementation impractical[50], [51].

1.4 Dissertation Synopsis

In this work, improvements have been addressed to both major components of microfluidic flow control (valving and pumping) for an accessible, plug-and-play flow control platform in the realm of cell culturing. For a novel, in-line valving concept, we introduced a passive, one-of-a-kind, in-line magnetic microvalve that can be fabricated without involving conventional MEMS fabrication procedures that may require expensive infrastructures [52]. This magnetic-based microvalve has low forward flow opening pressures suitable for lab-on-chip applications. In regards to driving flows suitable for microfluidic cell culture, we demonstrated a tunable, stand-alone pneumatic pump that features a 3D-printed micro-pressure regulator (µPR). With its downstream connected to a stabilizing liquid-primed microchannel resistor, the µPR is capable of driving fluid flows at different flow rates based on the user-defined regulated pressure. Both the pumping and valving solutions are created to be customizable, easy-to-fabricate, modular, and portable to fit in microfluidic applications.

Chapter 2 covers the in-line passive microvalve for low-pressure/low-flow applications via a magnetic microcapsule. In this chapter, the design logic behind the concept is detailed. Moreover, the fabrication process of this passive, integrable, customizable, in-line microvalve suitable for microfluidic applications is described. The objective is to create a microvalve that effectively blocks backward flows for the low-pressure-flow microfluidic regime. We fabricate the microcapsule (Φ0.75mm x 4mm) with a ferrofluid core and an impermeable flexible shell. This ferrofluid core was created by incorporating iron oxide (Fe_3O_4) nanoparticles into polyethylene-glycol. We pick parylene-c as the shell of the microcapsule to provide flexibility, sealing, and diffusion-blocking capability. We would then use a ring magnet (1.59/3.18-mm ID/OD, 1.59-mm height) to fix the microcapsule at its outlet end in a microtubing (0.79/1.59mm ID/OD). To evaluate the valving efficiency, we would apply differential pressures from both directions and document the resulting flow rates. The differential pressure required to drive liquid flows is applied using a commercial pressure regulator and a pressure gauge.

Chapter 3 covers a portable, controllable pump via a micro pressure regulator. In this chapter, we detailed the design concept and the fabrication processes of a tunable, modular micro pressure regulator that regulates a higher supply pressure to a more suitable range of pressures for pumping fluids in microfluidic systems. In pursuit of a cost-effective benchtop, tunable long-term pumping solution we create an accessible 3D-printed micro pressure regulator (μPR) (Φ12mm x 20mm) that regulates the higher pressure from a miniature air compressor down to a range of repeatable pressure (1 to 10 kPa). Regulated pressures drive stable flows for long-term (>24 h) cell culture applications. Ease-of-use pressure tuning can be achieved via manual turnings of a built-in control knob. In the design concept, pressure regulating is achieved using a force-balance mechanism. This mechanism involves the restoring force of the springs and the pneumatic-pressure-induced force. Turning the control knob to different rotational positions changes the springs' restoring force correspondingly. The pneumatic-pressure force changes to match the restoring force to maintain the balance of forces. This reflects the changes in the output pressure accordingly. The calibration of the control knob rotational positions would provide repeatable pressure of a device. During device operation, we supply the high-pressure to the pressure regulator via a commercial dc miniature air

compressor. The pressure regulator would output a regulated, lower pressure to drive a cell media reservoir to achieve desired tunable flow rates.

Chapter 4 introduces a power-free pumping platform via a dual-stage micro pressure regulator. Create a standalone, power-free, continuous flow control system for microfluidic-based cell culture. As *in vitro* studies have shown that cells distinctly change in morphology (aligned and more resembling the *in vivo* status as compared to static cultures) when exposed to mechanical stimuli, we plan to create a benchtop tunable pumping platform that can deliver different stimuli levels for microfluidic perfusion culture. Having a standalone, power-free flow control platform allows researchers to easily transfer in and out of incubators without dealing with the power-cord wiring complications. Through improvements to the system created in **Chapter 3**, we achieve a standalone, power-free flow control system for microfluidic cell culture by incorporating a dual-stage design. We would resolve the power requirements in the work done in **Chapter 3** by replacing the commercial miniature motor air compressor with a leak-free 3D-printed pressurized mini air tank. With a pressure regulator that regulates the higher pressure from the 3D-printed compressed air tank, we can drive fluid flow from a sealed liquid reservoir to a downstream flow stabilizer (fluidic resistor microchannel). The dual-stage pressure regulator can regulate pressure from a 3D-printed pressurized mini air tank (200 kPa) down to a tunable range of pressure (up to 10 kPa) that drives stable fluid flow over 24 hours for (1) proliferation [53] and (2) alignment of HUVECs (5.5-16 dynes/cm^2) [54], [55]. The flow rates can go up to 720 µL/hour, corresponding to the range of regulated pressures to 10 kPa. The pressure regulating principle is like that of **Chapter 3**. By introducing two stages, the pressure regulator suffers less from the supply pressure effect. This allows us to move on from a battery-powered pressure source to a pressurized air pressure chamber.

Chapter 2

Microvalves for Flow Rectification

2.1 Current State of Microvalves

2.1.1 Relevance of Microvalves in Microfluidic Systems

Microfluidic systems have demonstrated their usage in a variety of applications, including biological flow delivery, drug dosing, and chemical analyses[56], [57], [58], [59], [60], [61]. Manipulating fluids in micro or nanoscale has enabled new capabilities and improved effectiveness for downstream applications. Researchers turn to on microfluidic systems over their conventional counterparts due to the reduced reagent volumes required, high precision of dosages, portability of the device, effective flow control, and room for integration with other systems [62], [63]. Microvalves are essential microfluidic components used to rectify flows, on/off switching, and sealing from undesired particles for the platforms [7], [8]. Moreover, deploying microvalves in a system can prevent cross-contamination between liquids caused by backward flows. State-of-the-art valves are classified into two major categories - active and passive, each with its advantages and limitations. Active valves provide robust valving efficiency but generally require an external power source to operate. Such power consumption adds undesirable size, weight, and wire routing complexities, making these valves difficult to integrate into some lab-on-chip devices [64]. Passive valves, on the other hand, require no external power for actuation. Instead, they rely on design features for flow rectification.

2.1.2 Active valves and mechanisms

Active valves and their commonly implemented mechanisms are documented in the following Table 1.

Actuation Method	Actuation Components	Response Time	Pressure/Force/Deflection	Flow Rate	Applied Power Supply	Leakage Flow	Leakage Pressure	Reference
Electromagnetic	NiFe diaphragm membrane	Not reported	7.5E-13 kPa	Not reported	Not Reported	Not reported	Not reported	Yanagisawa 1995
Electromagnetic	PDMS diaphragm membrane	Not reported	2.3 kPa	Not reported	0.06 A	Not reported	Not reported	Bae 2003
Electromagnetic	Ni Ball	Not reported	Not reported	1300 mL/min	1 A	1 μL/min	21 kPa	Oh 2006
Electromagnetic	Fe pinch	Not reported	Not reported	836 mL/min	0.16 A	0	207 kPa	Oh 2005
Electromagnetic	NiFe integrated membrane	Not reported	3.15	Not reported	0.25 A	3.9μL/min	4.1 kPa	Choi 2001
Electrostatic	Indium Tin Oxide/PDMS membrane	0.9 s	6 psi (42 kPa)	185 nL/min	35-40 V	Not reported	(42 kPa)	Chang 2009
Electrostatic	Parylene diaphragm membrane	0.3 s	20 kPa	2 nL/min	60 V	Up to 9% of pressure	>20 kPa	Yıldırım 2012
Electrostatic	Multilayer parylene membrane	0.1 ms	6.9-34 kPa	1.5-9 μL/min	20-400 V	9 μL/min	21 kPa	Xie 2003
Piezoelectric	PZT disc/ silicon gel hydraulic chamber	2 ms	100 kPa	Not reported	300 V	13.3 nL/min	100 kPa	Rogge 2003
Piezoelectric	PZT stack/ hydraulic chamber	0.1 s	140 N	Not reported	100 V	420 μL/min	600 kPa	Peirs 2000
Piezoelectric	Santoprene deflected by piezobimorph		50 μm	190 μL/min	50-150 V	2 nL/min	1 kPa	Waibel 2003
Piezoelectric	PZT stack/ hydraulic chamber	< 0.1 s	40-80 kPa (192 μm)	0-8.75 mL/min	40-200 V	Not reported	39 kPa	Chen 2016
Electrochemical	Cu/Pt electrodes	~1s	200 kPa/(30-70 μm)	Not reported	1.6 V 50 μA	Not reported	200 kPa	Neagu 1997
Electrochemical	Cation selective membrane (Nafion)	15 s	5 psi (35 kPa)	0-55 μL/min	1 V 0.125 mA	0-55 μL/min	35 kPa	Das 2016
Electrochemical	Pt electrodes/ PDMS membrane/ NaCl	6 min	200 kPa	Not reported	2.5 V	Not reported	200 kPa	Lee 2008
Electrothermal	Thermo-pneumatic	< 30 s	0.46 kPa	1.01-5.24 μL/min	0.22 W	Not reported	Not reported	Chee 2015
Electrothermal	Thermo-pneumatic	8 s	20 kPa	1 μL/min	0.2 W	1 μL/min	30 kPa	Takao 2005
Electrothermal	Phase-change Paraffin	15-23 s	107 kPa	Not reported	50-170 W	Not reported	107 kPa	Baek 2013
Electrothermal	Shape memory alloy pinch (NiTi)	~1 s	207 kPa	16.8 mL/min	398 mW	16.8 mL/min	21 kPa	Pemble 1999
Electrothermal	Low melting point alloy	~1 s	140 kPa	Not reported	50 mW	Not reported	140 kPa	Shaikh 2008

Table 2.1. Classifications of Active Valve Mechanisms [26], [27], [28], [30], [31], [65], [66], [67], [68], [69], [70], [71], [72], [73], [74], [75], [76], [77], [78]

As seen from the above table, electricity-driven mechanisms constitute most of the active valving mechanisms. They can be further categorized into electrostatic, piezoelectric, electromagnetic, electrochemical, electrothermal.

a) Electrostatic actuation

Electrostatic microvalves usually comprise a valve-opening/closing membrane along with a pair of electrodes, controlled by a connected circuit[69]. Actuating the valve is realized by controlling the voltage to move the membrane toward the desired level[79]. The electrostatic force between the electrodes was

created by the "pull-in voltage". This voltage scales to the closing force of the valve, which dictates the sealing pressure of the valve. The response time of this type of valve is short (under ms) and the operating energy consumption is low [66]. However, the operating voltage can range from 50 to 220 V, making them dangerous to cell monolayer if leakage current occurs[7].

b) Piezoelectric actuation

Piezoelectric materials, such as PVDF (polyvinylidene fluoride) or PZT (lead zirconate titanate) have been used to realize valving in the microfluidic level[20], [21], [22], [80]. Piezoelectric materials in stacks or discs exert a large force making them suitable for large pressure (MPa) applications[81], [82]. Due to the nature of the piezoelectric actuators, the displacements of the valving components are small (1~10μm) even when actuated by a large voltage (>100V)[83]. Even with a hydraulically amplifying design to increase the displacement of the valve, Chen et al. were only able to drive a maximum valve displacement from 22 to 308μm at 100 V of operating voltage [75]. This makes them difficult to be applied to microchannels or microtubings with larger thickness/ diameter.

c) (Electro)magnetic actuation

Typical magnetic microvalves involve permanent magnets and flexible membranes (or in-line mobile structures) with soft magnetic material[84], [85], [86]. The deflection of the membrane or the movement of the mobile structure (often a stainless-steel sphere) is caused by the control of magnetic forces[15], [16], [87]. Electromagnetic actuation provides a relatively fast response with room for larger displacement of valve body compared to piezoelectric actuation while maintaining a robust seal against large stroking force. For instance, Liu et al. created an electromagnetic valve for pneumatic control of microfluidic with an operating response of ~17 ms[84]. Paschalis et al. introduced a ferrofluid-based valve consisting of a silicone capillary tube, two permanent magnets, and a ferrofluid that can be manually displaced to accommodate the users' desired direction of flows[88]. Since the (electro)magnetic actuators often require at least a coil or a permanent magnet, this makes scaling difficult for miniaturized applications[7].

d) Electrochemical actuation

These actuators operate via reversible electrochemical processes to open/close the passage for fluids to pass through. Electrodes were to electrolyze solution to produce bubbles in sealed chambers [28], [29], [89]. This increases the pressure within and deflects the moving structures, e.g. PDMS membranes, SU-8 cantilevers, for the microvalve to operate [28]. Reduction and oxidation (redox) reactions are involved in the reproducible production and consumption of gas bubbles at the electrodes. By controlling the actuation voltage, users are allowed to precisely control the valve membrane/ cantilever. Since the sealing is based on the production of gas bubbles in a tiny microchamber to reduce the operation time, these valves are not suitable for high backpressure/ high flow rate regime [8]. These actuators are often produced via typical MEMS fabrication processes; this makes a perfect seal against gas leakage challenging for these devices over time. Moreover, the electrochemical reactions can cause the degradation of materials over time, affecting the longevity and reliability of the microvalve.

e) Electrothermal actuation

Electrothermal actuators operate via reversible heating/cooling processes to open/close a microvalve. Bi-metallic [90], shape-memory alloy [77], [91], [92], paraffin [76], and thermopneumatic [26], [27], [93], have been used to realize the electrothermal actuation. Electrothermal actuators used for microvalves present capabilities to provide large displacement actuation.

2.1.3 Passive valves and their mechanisms

Passive valves can be categorized by their actuation methods – mechanical and non-mechanical. Some common non-mechanical passive valves include diffuser-type valves and capillary-effects-based valves [94], [95], [96], [97]. These valves offer flow directionality by introducing imbalanced flow resistance. This can be achieved by the design of geometries or different surface properties (hydrophilic/hydrophobic). Diffuser-based passive valves perform poorly in preventing leakage since the diffuser elements in these valves are always open [8]. Capillary-based passive valves also face similar issues, as the microchannels are normally open. These valves also face difficulties blocking vapor from one side to the other, resulting in cross-contamination of fluids. Conventional passive mechanical valves exploit backpressure to seal the

valve from backward flows. Mechanical actuators for such valves include cantilever-type flaps, membranes, or spherical balls[15], [98], [99]. These actuators generally provide robust rectification against higher backpressure. Current mechanical passive valves (check valves), due to the stiction of the valve/seat interface, can suffer from large opening pressures, making them unsuitable for low operating pressure applications. Moreover, actuating components of these conventional mechanical valves may suffer from poor sealing when encountering low backpressure[13]. This is because these valves rely on backpressure to provide the closing force and would not close against backward flows until they encounter a certain level of backpressure. In general, mechanical passive valves suffer from leakage flows for applications with low operating pressures. The improvements of the passive valves usually come from the materials used, the coating technology breakthrough from stiction prevention, and the miniaturization of the valves to prevent dead volumes.

2.1.4 Choosing passive valves over active valves for implementation

There are pros and cons of choosing active or passive valves. Active valves in general provide robust valving efficiency but require external power to operate. This peripheral power source likely adds undesirable size, weight, and wiring complexities for lab-on-chip applications. Passive valves, on the other hand, are commonly realized by exploiting the geometrical or mechanical differences between the two flow directions. However, these valves are typically more limited in modes of valving (preferred flow directions). Passive valves provide the simplicity of usage without external power sources, reliability because they often encounter few moving parts and no need for external actuation and require less maintenance, and miniaturization that makes them well suited for compact and portable devices [33], [100]. In exchange, we will have less control accuracy in the valving compartment in the microfluidic systems.

2.1.5 Performance evaluation of a passive valve

Several key factors for the passive valve evaluation include its flow rectifying capability, threshold pressure, leakage flow rate, size, and dead volume. Flow rectifying capability, or valving efficiency can be evaluated through the ratio of the forward flow rate over the backward flow rate under the same pressure drop applied

across the microvalve. The threshold pressure, or opening pressure, refers to the minimum pressure required to open the valve. This metric is essential for ensuring the valve operates under specific conditions. Leakage flow rates of the passive valve often occur when it encounters low backward (reverse) flows. This is because check valves, mechanical passive one-way valves, close based on the force generated from backward flows; low-pressure backward flows don't generate enough force to prevent leakage from happening. The size (scaling capability) of the passive valve allows it to fit in smaller form factors. Finally, the dead volume of a passive valve refers to the volume of fluid that remains trapped within the valve when it's not in use. The residual fluid can affect the precision and efficiency of fluid control in microfluidic systems. In general, lower dead volume also comes along with faster response times.

2.2 Technology gap and significance

Current mechanical check valves suffer from dead volume of operating chambers of diaphragm/ rooms for in-line mobile structure, leakage issues under low backpressure regime, and large opening pressure due to the seat/ valve interface stiction [101]. In this dissertation, a new actuation concept for a passive valve is introduced to achieve efficient flow regulation at low pressures while capable of blocking diffusion. This valve, due to the design concept, shows near-zero dead volume. Moreover, the fabrication process of the microvalve is simple compared to the typical MEMS processes required for most check valves and can be easily customized to accommodate different microfluidic systems. The working mechanism of the passive valve is based on the imbalanced deformation of magnetically responsive soft microcapsules from different flow directions. Such microcapsules feature a magnetically responsive core, and a biocompatible, impermeable shell. The Fe_3O_4/polyethylene-glycol (PEG) mixture was chosen as the biocompatible magnetic nanocomposite core and Parylene-C as the biocompatible shell to realize this valve concept [102], [103], [104]. The Parylene-C shell provides enclosure, flexibility, and a barrier between the nanocomposite and the fluid flow. The valve demonstrates effective flow rectification capabilities, low reverse leakage

flows at low pressure, diffusion blocking capabilities, and simplicities in integration into microfluidic systems.

2.3 Concept and theory

A cylindrical magnetic microcapsule is chosen to fit in a microchannel to realize valving. The microcapsule consists of a magnetic nanocomposite core and a polymeric shell. For this device to be biocompatible, superparamagnetic iron oxide (Fe_3O_4) nanoparticles are chosen to be the soft magnetic material. These nanoparticles are suspended in polyethylene-glycol (with an average molecular weight of 1500) to act as the composite core in the microcapsule. The microcapsule features a soft polymeric shell of parylene-c, which has shown biocompatibility and is commonly used in biomedical applications. The fabricated microcapsule is guided into the microchannel and steered to the desired location using a ring magnet (1.32T). The ring magnet is fixed at one edge of the microcapsule as shown in **Figure 2.1(a)**; this edge is now deemed the outlet edge. Since the nanocomposite core is in the liquid phase during operation, the nanoparticles of the nanocomposite can freely move toward, and agglomerate at the microcapsule's outlet edge under the influence of the ring magnet. These nanoparticles at the outlet edge push the polymeric shell of the microcapsule to expand radially. This creates a tight contact between the microcapsule and the microchannel wall. As shown in **Figure 2.1(a)**, this contact creates a firm seal. When encountering forward flow pressures, the path can open easily due to the directionality of the microvalve as shown in **Figure 2.1(b)**. The concept of flow directionality can be explained by the difference in the forces encountered in the forward vs backward flow scenarios.
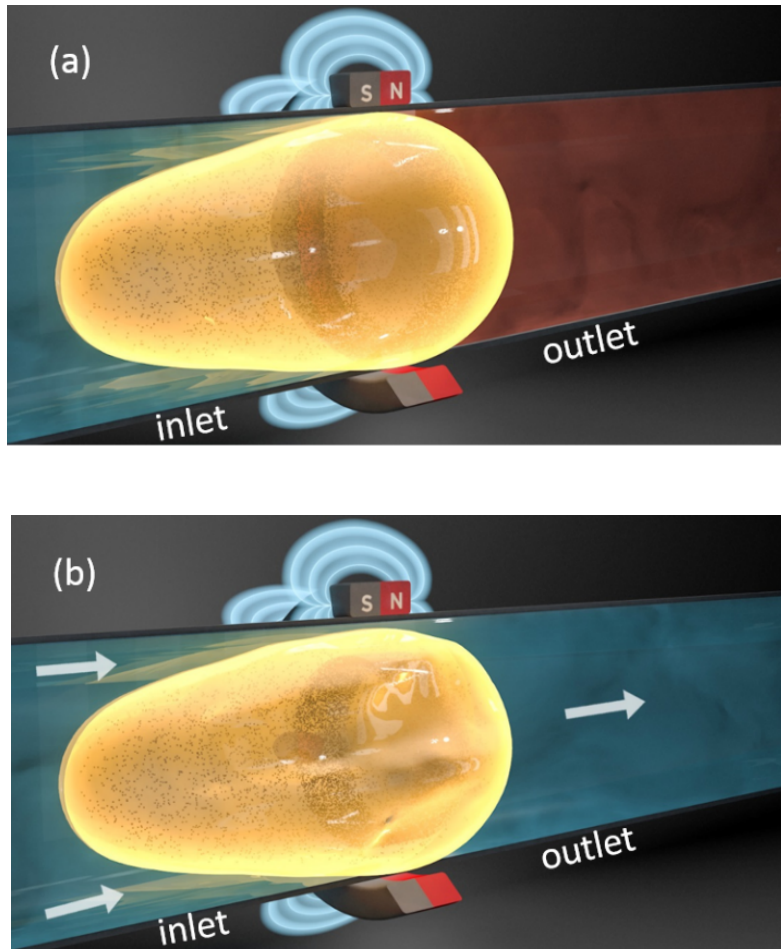
Figure 2.1 (a) 3D Illustration of the valve with a magnetic field gradient source applied at the outlet edge. This magnetic field gradient source (ring magnet) expands the microcapsule at the outlet edge and seals the microchannel. **(b)** 3D illustration of the microvalve. The valve demonstrates flow directionality – opens for forward flows.

2.3.1 Balance of Forces to Realize the Novel Valving Concept

In this following section, the forces involved in the theory of this new valving concept are discussed. These forces include the magnetic force provided by the ring magnet, the frictional force between the microcapsule and the microtubing, and the flow-pressure-induced forces on the microcapsule.

a) Magnetic force

The microvalve sealing is governed by the magnetic attraction force $\vec{F}_{mag}$. The ring magnet exerts the magnetic force $(\vec{F}_m)$ on each nanoparticle as represented in **Equation 2.1**.

$$\vec{F}_m = \nabla(\vec{m} \cdot \vec{B}) \qquad \text{(Equation 2.1)}$$

where $\vec{m}$ is the magnetic dipole moment of a single nanoparticle, $\vec{B}$ is the magnetic field.

Since the size of the nanoparticle allows it to align with the magnetic field lines, **Equation 1** can be rewritten as the form of **Equation 2.2**.

$$\vec{F}_m = (\vec{m} \cdot \nabla)\vec{B} \qquad \text{(Equation 2.2)}$$

Each nanoparticle is interpreted as a small sphere. This allows us to portray $\vec{m}$, the magnetic dipole moment of the nanoparticle, as shown in **Equation 2.3**.

$$\vec{m} = \rho v \vec{M} = \rho \frac{4\pi}{3} a^3 \vec{M} \qquad \text{(Equation 2.3)}$$

where ρ is the particle's density, v is the volume of the particle, $\vec{M}$ is the magnetization of the particle per unit weight, and a is the radius of the nanoparticle.

The microcapsule is discussed in cylindrical coordinates due to its geometry. The magnetic force that contributes to the sealing of the valve is in the radial direction, combined with **Equations 2.2** and **2.3**, which are shown in **Equation 2.4**.

$$\vec{F}_m = \rho \frac{4\pi}{3} a^3 \vec{M} \frac{\partial}{\partial r} \vec{B} \qquad \text{(Equation 2.4)}$$

The total magnetic force of all encapsulated nanoparticles $\vec{F}_{mag}$ is represented as in **Equation 5**.

$$\vec{F}_{mag} = \sum_N \vec{F}_m \qquad \text{(Equation 2.5)}$$

where N is the number of nanoparticles encapsulated in the microcapsule.

23

The number of encapsulated nanoparticles is concentration- and volume-dependent, as seen in **Equation 2.6**.

$$N = \frac{CV}{v}$$

<div align="right">(Equation 2.6)</div>

where C is the concentration of nanoparticles in the nanocomposite, V is the total volume of the nanocomposite.

b) Frictional force and pressure-induced forces

The introduced valving mechanism predicts that the microvalve is suitable for low operating pressures. When the applied inlet (forward flow) pressure is too high, the forward force ($\vec{F}_f$) due to the applied inlet pressure may cause the microcapsule to slide in the microtubing. When sliding occurs during operation, the microcapsule would be flushed away by the applied pressure - a catastrophic mechanical failure of the microvalve. To prevent the microcapsule from sliding, we need to ensure that the pushing force ($\vec{F}_f$) is smaller than the maximum friction force ($\vec{F}_{frmax}$) between the microcapsule and the tubing wall. For a more straightforward depiction of the scenario, we consider the pushing force effective along the z-axis, as radial forces do not contribute directly to the movement of the microcapsule along the microchannel.

The forward force by the fluid, $\vec{F}_f$, is presented in **Equation 2.7**.

$$\vec{F}_f = -\int P \, \vec{n} \cdot \hat{z} \; dA$$

<div align="right">(Equation 2.7)</div>

where P is the applied flow pressure, $\vec{n}$ is the normal vector to the surface, $\hat{z}$ is the unit vector along the z-axis in the cylindrical coordinates, and dA is the infinitesimal area element of the microcapsule's surface exposed to the fluid flow pressure.

Since friction is related to the normal force against the surface and the interface's surface properties, we present the maximum friction to keep the microcapsule as shown in **Equation 2.8**.

$$\vec{F}_{frmax} = \mu_s \vec{F}_n$$

<div align="right">(Equation 2.8)</div>

where $\vec{F}_{frmax}$ is the maximum friction force, μ_s is the coefficient of static friction, and $\vec{F}_n$ is the normal force of the surfaces.

The magnetic force of the nanoparticles pushes the microcapsule shell radially and creates contact with the inner wall of the microchannel. This contact results in a normal force ($\vec{F}_n$) between the microcapsule shell and the microchannel's inner. Since the polymeric shell easily changes shape without providing much resistance, we consider no loss in the force applied - the normal force ($\vec{F}_n$) is considered to have the same direction and strength as the magnetic force.

During operation, the valve allows flows when the opening force ($\vec{F}_p$) exceeds the normal force ($\vec{F}_n$). This opening force, caused by the pressure of the applied flow, opens paths for fluid flow past the valve as shown in **Figure 2.1(b)**. $\vec{F}_p$, induced by the applied flow pressure, is effective in the radial axis, as represented in **Equation 2.9**.

$$\vec{F}_p = -\int P\,\vec{n}\cdot\hat{r}\ dA \qquad \textbf{(Equation 2.9)}$$

where $\hat{r}$ is the unit vector along the radial direction in the cylindrical coordinate, and dA is the infinitesimal area element of the shell's surface exposed to the fluid flow.

When backpressure is applied from the outlet edge, the majority of normal vectors of area elements can be seen along the z-axis. This suggests a much smaller opening force when pressure is applied in the backward direction. This unique valve design offers flow directionality.

2.4 Materials and methods

a) Materials selection

The microvalve setup requires a magnetic microcapsule and a magnetic field gradient source. To fabricate the magnetic nanocomposite as the core of the microcapsule, biocompatible materials are included - polyethylene glycol is chosen with an average molecular weight of 1500 (PEG-1500) because of its melting temperature and Fe_3O_4 nanoparticles. These materials are commonly used for biocompatible applications. Fe_3O_4 nanoparticles are selected for their high saturation magnetization and soft magnetic properties. In this work, Fe_3O_4 nanoparticles are chosen with an average diameter of 300 nm – a size that provides a good

balance between mobility and magnetization. The low mass and small size facilitate the particles' transport within the microcapsule toward the magnetic field source. The high saturation magnetization of selected particles, compared to that of the smaller diameter nanoparticles, is essential to provide sufficient magnetic forces as described in **Equation 2.4**. PEG-1500 is chosen for its phase-change characteristics – solid-phase during shell coating, and molten at a relatively low temperature at 44-47°C. Sustained heating of PEG-1500 for 72 hours at 80°C results in thermal degradation, a phenomenon commonly involved in the breakdown of PEG's molecular chains. This leads to a lower melting temperature lower than room temperature, yielding a liquid-phase nanocomposite microcapsule core. Parylene-C is selected as the encapsulation material due to its role as a gas and liquid barrier [105]. The concept can be realized for a wide range of geometry designs, materials, and dimensions of microfluidic channels. In this work, commercial fluorinated ethylene propylene (FEP) tubing with an inner diameter (ID) of 794 μm and 1.59 mm outer diameter (OD) was selected to demonstrate the capability of this concept. A 1.32T, N42 axially magnetized NdFeB ring magnet (K&J Magnetics 1/8"OD x 1/16"ID x 1/16" thickness) was used to provide the magnetic field gradient required to seal the valve at the outlet end.

b) COMSOL multiphysics simulation

A 2D-axisymmetric stationary COMSOL Multiphysics® simulation was performed to evaluate the valve concept. Via the fluid-structure interaction (FSI) physics model in COMSOL, the mechanical properties of the microcapsule with its liquid core and the polymeric shell and the magnetic load at the end of the microcapsule were investigated. The model was built by encapsulating a bulb of a PEG-like fluid (density = 1000 kg· m^{-3}, dynamic viscosity = 0.001 Pa·s) with a 2-μm-thick Parylene-C (density = 1290 kg·m^{-3}, Poisson's ratio = 0.4, Young's Modulus = 1.67 GPa) layer. The mechanical properties of Parylene-C were obtained experimentally with a tensile test (Series 5560 Load Frame, Instron, Norwood, MA, USA). The microcapsule is modeled as a cylinder with a diameter of 784 μm and a length of 4 mm. The outer boundary is constrained to the inner diameter of the FEP tubing used for experimental verification. This tubing has an inner diameter of 794 μm, leaving a 5-μm gap between the inner wall of the tubing and the microcapsule before the application of the magnetic force. The magnetic force acting on the wall of the microcapsule was

calculated by distributing the magnetic force calculated using **Equation 2.5**, considering the concentration to be 75% wt/wt Fe_3O_4: PEG, by the circumference of the microcapsule. To simplify the load of the magnetic force, the load is chosen to be in the form of the ring load as the magnetic gradient would be the strongest at a certain position. This ring load due to the magnetic force attraction between the nanoparticles and the permanent magnet was calculated to be 3.43 N/m. The load deformed the microcapsule and stretched its shell toward the inner wall of the microtubing; decreasing the gap to 0.7 nm as shown in **Figure 2.2**.
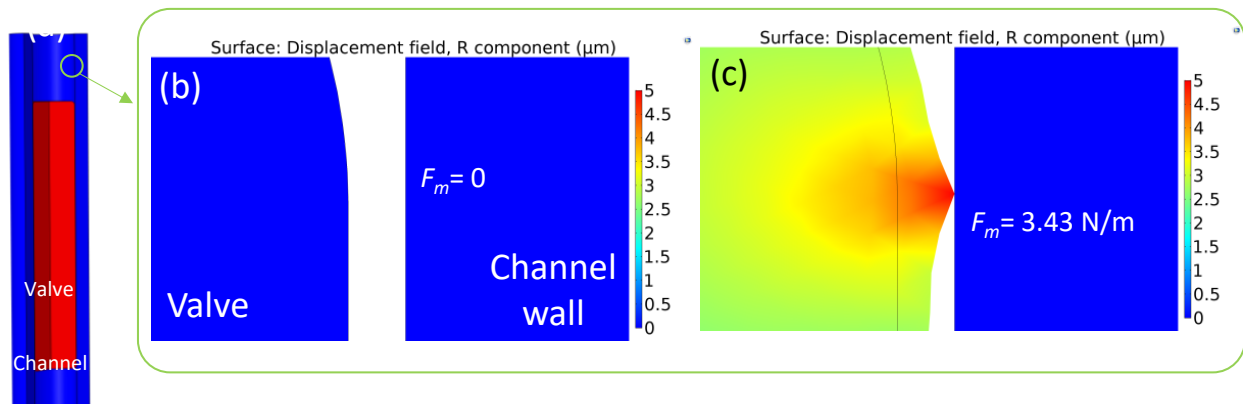

Figure 2.2: **(a)** COMSOL 2D-Axisymmetric model with a 4 mm-long microcapsule **(b)** Zoomed-in view of microcapsule-microchannel wall gap without magnetic force ring load, and **(c)** magnetic force applied to show deformation.

The interaction between the fluid flow within the tube and the capsule was investigated by simplifying the model into a single solid object with an equivalent Young's modulus and mechanical properties as the FSI model. The COMSOL structural model used the same geometry and loading as previously described (3.43 N/m ring force). The capsule's top and bottom were set as fixed. A parametric sweep was performed to ascertain the effective Young's modulus of the single object model to match the deformation of the FSI model. A Young's modulus of 2.15 MPa provided deformations within 0.14% of the FSI model and was used in the fluid flow simulations.

Geometric changes of the solid object model were investigated with differential pressure applied at the inlet and outlet sides of the tubing. As in the FSI model, under zero applied differential pressure, the valve-to-

wall gap was 0.70 nm, effectively sealing the valve to block diffusion. Application of pressure to the inlet

side of the valve walls resulted in microcapsule wall deformation to expand the valve-to-wall gap to 0.42

μm at 15 kPa. When the pressure was applied to the outlet side of the valve walls, the valve-to-wall gap is

significantly reduced to 0.17 μm at 15 kPa. Results of valve-to-wall gap versus applied pressure are shown

in **Figure 2.3**.
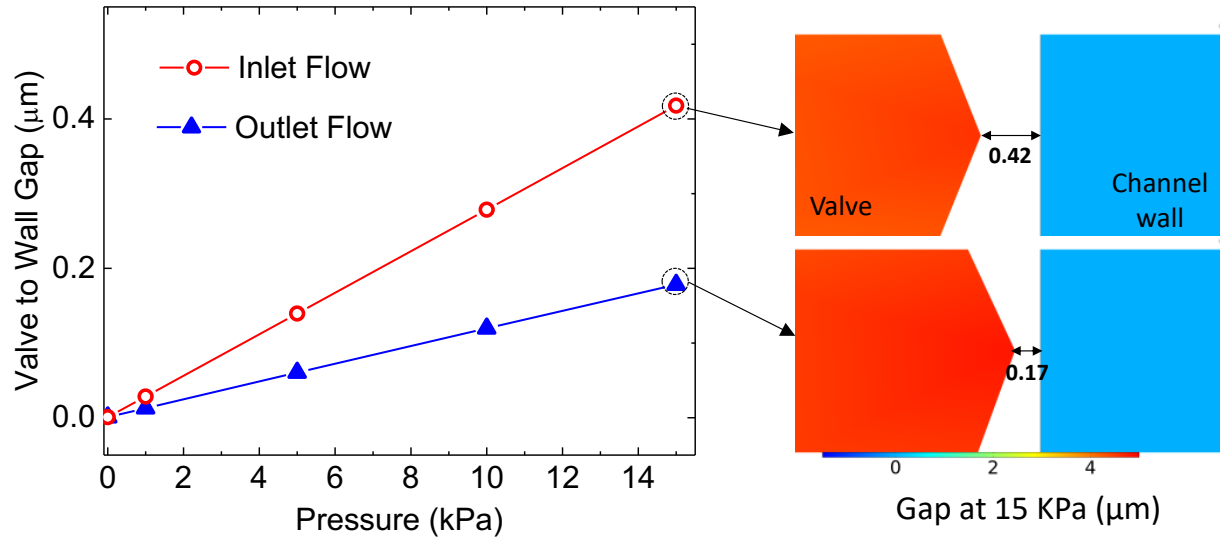
Figure 2.3: Capsule to channel wall gap at the magnetic attraction point (3.43 N/m load) versus applied pressures from inlet or outlet ends (forward and backward flows). The inset showed that the capsule-to-channel-wall gaps at 15 kPa were 0.42 and 0.17 for forward and back flows, respectively.

A corresponding laminar flow model predicted the flow rate of water versus applied pressure based on the

predicted valve deformations. As shown in **Figure 2.4**, the model predicts flow rectification behavior of

300%, with a significantly larger resistance to backpressure-driven flows.

Figure 2.4: Simulated flow rates resulting from pressure applied at the inlet (forward flow) and outlet (backward flow). Flow rectification is achieved with the passive valve design.

c) Fabrication of the microvalve

The fabrication process of the valve is illustrated in **Figure 2.5**. Nanocomposites were prepared by incorporating Fe_3O_4 nanoparticles (300 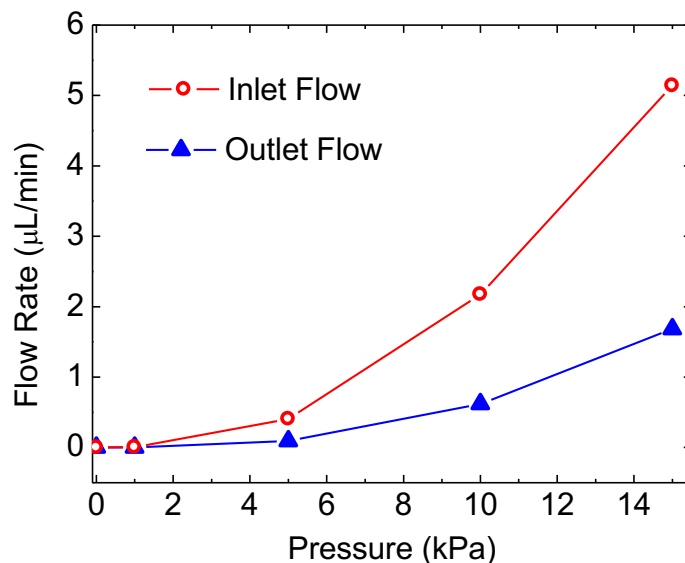nm by Alpha Chemicals) into molten PEG with concentrations of 50%, and 75% Fe_3O_4: PEG weight-to-weight ratio. A heated ultrasonication bath ensured proper mixing and break down of agglomerates. When the nanoparticles exceed 75% wt-wt ratio, the composite becomes brittle and prone to breakage during fabrication. As the nanoparticle concentration reaches the 25% wt-wt ratio, the fabricated microvalve no longer exhibits flow rectification. FEP tubing with a 750-µm inner diameter served as the mold of the nanocomposite. The nanocomposite within the FEP tubing mold was placed in vacuum to eliminate trapped air cavities and cooled down to solidify the PEG. The resulting ingot was pushed out of the tube and manually cut into microcapsule cores with the desired lengths (i.e. 1-4 mm). The microcapsule cores were then encapsulated by ~2 µm Parylene-C (Specialty Coating Systems, Indianapolis, Indiana) using a customized magnetic rotating stage to turn the microcapsules during deposition and achieve a uniform coating using a built Parylene deposition tool. Using magnetic tweezers, the microcapsule was dropped into the target fluidic channel, in this work, 794 µm-inner-diameter FEP tubing. The microcapsule was steered to the desired location in the FEP tubing with pressurized deionized

29

water. An N42 axially magnetized NdFeB ring magnet was used over the FEP tubing to lock the Parylene-C coated nanocomposite from one end. Moreover, the ring magnet provides the necessary magnetic field gradient required for operation. After being locked in place, the microcapsule was heated to melt the nanocomposite allowing the nanoparticles to be attracted to the magnet and agglomerate at the edge forming a sealing point. Short-term heating at 75°C for 72 hours successfully thermally-degraded the PEG polymer, lowering the melting temperature to below room temperature.
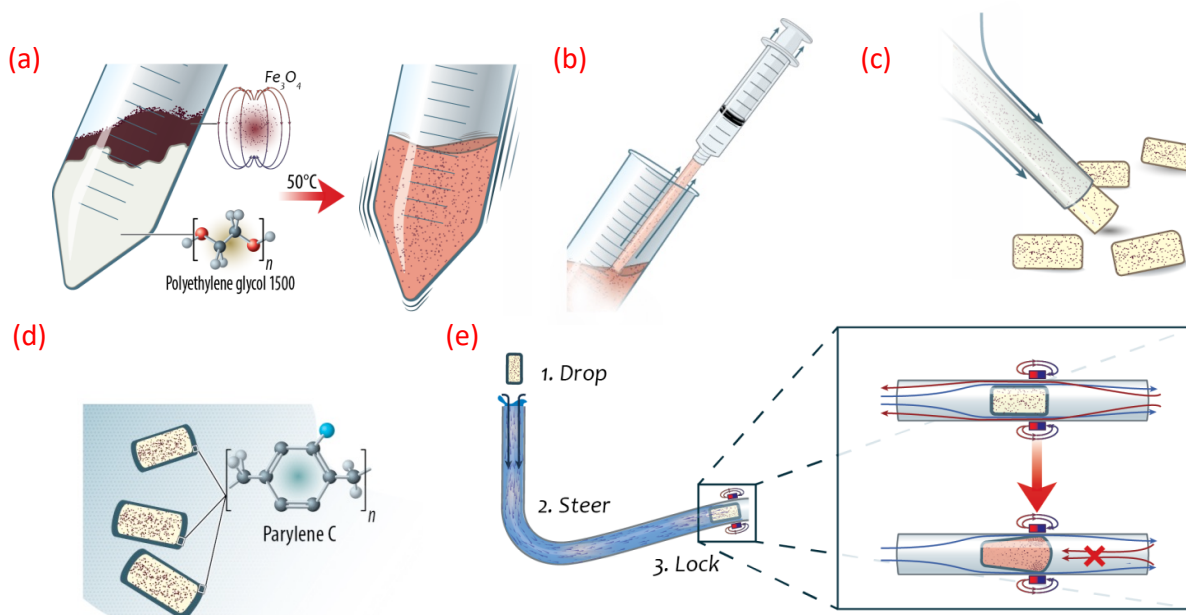
Figure 2.5: Illustration of the fabrication process. **(a)** We incorporated Fe_3O_4 nanoparticles into molten PEG to form the magnetic nanocomposite **(b)** The magnetic nanocomposite was transferred to the FEP tubing mold and cooled under vacuum **(c)** The magnetic nanocomposite is cut into pieces with desired lengths to be used as the core of the microcapsule **(d)** We encapsulate the magnetic nanocomposite cores with Parylene-C to form microcapsules **(e)** The magnetic microcapsule was steered to the desired location, locked in place with a ring magnet, and heated for PEG thermal degradation to ensure the core in the liquid phase.

d) Characterization and experimental setup

Scanning electron microscope (SEM) was used to inspect the quality of the Parylene-C encapsulation shell. We imaged the microcapsules as fabricated and after being used for valving. By using the vibrating sample magnetometer (VSM) to obtain the microcapsules' magnetic properties, the magnetizations from different

concentrations of magnetic nanocomposites are investigated. The number of nanoparticles affects the magnetic force applied to the microcapsule shell hence affecting the valve performance.

Valving performance was documented in a flow rate vs applied pressure experiment using dyed deionized water throughout the FEP tubing. Regulated pressures were applied from the inlet side and then repeated from the outlet side with the recording of the travel distance of the dyed water over time to determine the flow rate. The opening pressure and flow rectification performance were studied as a function of magnetic nanoparticle concentration in the nanocomposite.

To test the valve's diffusion blocking capability, a fluorescein sodium salt solution of 1mg/ml in deionized water was carefully injected into the hole drilled on the tubing at the outlet end of the valve. The diffusion was observed by recording the fluorescence intensity variation over time at the inlet and the outlet ends of the valve using a fluorescence microscope (LEICA DM 2500) at the 515-nm emitting wavelength. The fluorescence intensity of the inlet end of the valve was normalized by the intensity measured at the outlet side at the same time. The diffusion test without the valve was performed similarly, however, a 4 mm air gap was kept between the injected hole of fluorescein solution and the inlet measurement spot. The gap was filled with deionized water using a 34G syringe tip inserted from the inlet side of the tubing right before the fluorescence intensity measurements to avoid the capillary effects and ensure the time origin of the contact between the fluorescein solution and deionized water. The fluorescence intensities of the inlet and outlet measurement spots were recorded instead of the inlet and outlet ends of the valve. The designated inlet measurements of intensities were normalized by the outlet measurements at the same time.

2.5 Results and takeaways

Magnetization of the nanocomposite core in the microcapsule plays a key role in the magnetic attraction force – a key factor that provides the seal of the valve, and controls the operating pressures as well as the operating range. To confirm the uniformity of magnetic nanocomposite from the fabrication process, we utilized the vibrating sample magnetometer (VSM) to characterize the magnetizations of the fabricated

microcapsules. Magnetization measurements are presented in **Figure 2.6**. We investigated the concentration-dependent magnetizations for valves - 19 emu/g and 33.2 emu/g for microcapsules with concentrations of 50%, and 75% wt/wt Fe_3O_4: PEG, respectively. VSM also helped reassure a key hypothetical mechanism - Fe_3O_4 nanoparticles can be attracted and travel freely and accumulate at the designated outlet edge of the microcapsule under the influence of the magnetic field source (ring magnet). To characterize the magnetization distributions of the microcapsules to determine the proper microcapsule length, we cut microcapsules of different lengths into 1-mm-long segments and characterize the magnetizations immediately for two scenarios – right after fabrication and right after operation. A fixed concentration of 75% wt-wt Fe_3O_4: PEG was used for devices with lengths of 2 mm, 4 mm, and 5 mm. As fabricated microcapsules were retained at room temperature in their solid phase, cut, and analyzed. After use, microcapsules were inserted into the 794-μm-ID FEP tubing and locked in place with the ring magnet as previously described. Following thermal degradation, the microcapsules were cooled to room temperature and then frozen in liquid nitrogen to ensure full solidification before cutting and VSM analysis. Magnetizations for each segment are shown in **Figure 2.7.** The as-fabricated samples exhibit a uniform distribution of the nanoparticles. Following use, there is a clear gradient of magnetization - low at the inlet side and peaking at the outlet side of the microcapsule. This demonstrates the Fe_3O_4 nanoparticles migrating toward the magnetic source while PEG is in the liquid phase. The shortest valves (2-mm-long) yielded a lower peak magnetization than the 4-mm and 5-mm valves, suggesting an insufficient magnetic nanoparticle density. The 5-mm-long microcapsule, as shown in **Figure 7(c),** exhibited a non-zero magnetization at the inlet edge (Length 0-1). This suggested that the ring magnet does not possess sufficient magnetic strength to attract all particles in microcapsules of this size. For this configuration (794-μm-ID microtubing, and the selected N42 axially magnetized NdFeB ring magnet), the optimal microcapsule length is 4 mm long.
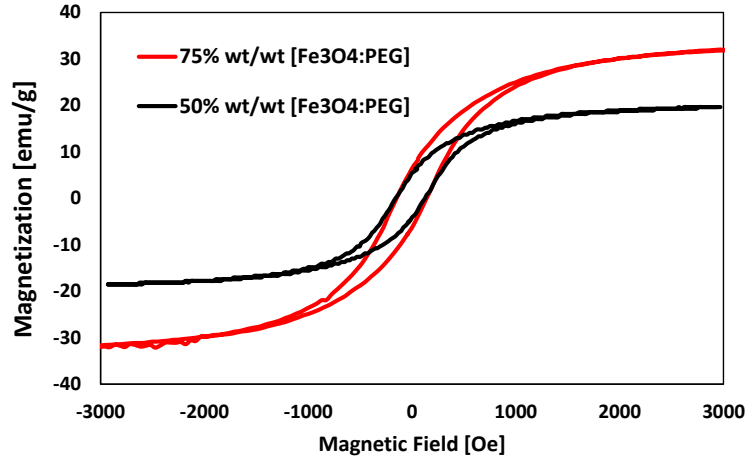
Figure 2.6: Magnetization curves for nanocomposites in microcapsules with concentrations of 50%, and 75% wt/wt Fe_3O_4: PEG characterized using the vibrating sample magnetometer.
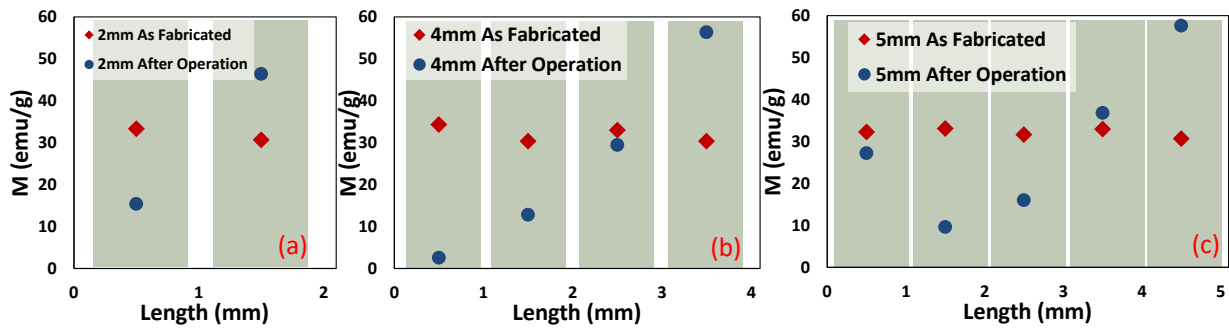
Figure 2.7: Magnetization distributions for microcapsules as-fabricated and after-operation with lengths of **(a)** 2 mm, **(b)** 4 mm, and **(c)** 5 mm.

The shape and morphology of the microcapsules were studied through SEM imaging. **Figure 2.8(a)** shows the fabricated cylindrical shape microcapsule in its solid state. The image shows the uniformity of the Parylene-C encapsulation and the consistent diameter of 750 μm. When inserted into the fluidic channel, the solid microcapsule will add fluid resistance but will not act as a valve. As the microcapsule is heated within the fluidic channel in the presence of the magnetic field source, the geometry changes to provide the valve function. **Figure 2.8(b)** shows the geometry change of the microcapsule, with the outlet side expanding under the force of the magnetic nanoparticles while the inlet side narrows. Texture variation is

33

due to shrinkage of the operated microcapsule after re-solidification (a process that is not done in normal use); microcapsule dimensions are not representative of the actual dimensions in use.

Figure 2.8: Geometries of the microcapsule **(a)** as-fabricated **(b)** following operation with a magnetic field source (PEG in liquid phase) and re-solidification for removal and image analysis.

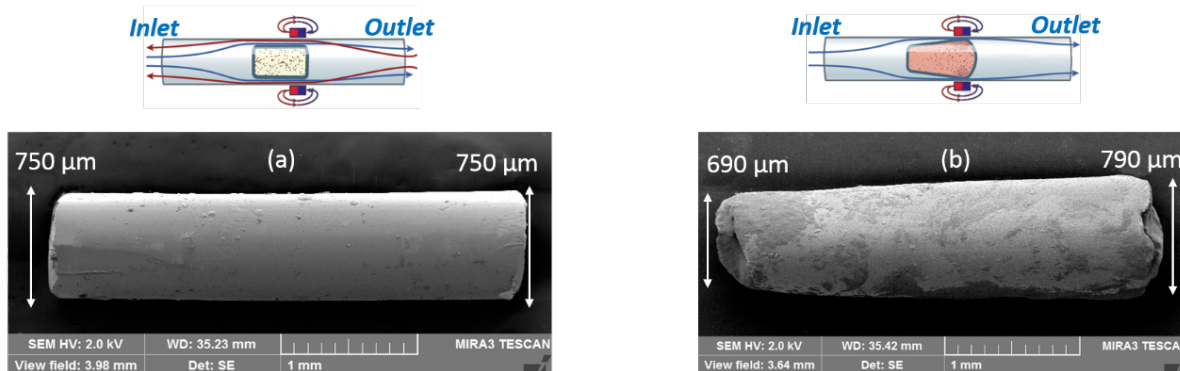Flow rectification and leakage pressure are important parameters for valving efficiency. Flow rate vs. pressure tests were conducted for 4-mm-long 50%, and 75% wt/wt Fe_3O_4: PEG microcapsules with fabricated diameters of 750 μm. As shown in **Figure 2.9(a)**, the 50% formulation provided flow rectification but only achieved an inlet vs. outlet ratio of 4.2 at 14 kPa. The 75% formulation (as seen in **Figure 2.9(b)**) demonstrated outstanding flow rectification with an inlet flow of 5 μL/min and an outlet flow of less than 0.07 μL/min at 14 kPa flow pressure. This yields a 71.4 inlet vs. outlet flow ratio. This enhanced performance is due to the stronger magnetic force attraction, which provides better sealing between the microcapsule wall and the tubing wall. In addition, the microvalve sees extremely low leakage flows from backpressures at a rate of 4.7 nL/min kPa^{-1} for the 75% formulation, solving one of the major challenges passive microvalves encounter – low-pressure range leakage flows that might cause cross-contamination of fluids. The valve successfully blocked backward flows coming from the outlet side at backpressures up to 5.5 kPa, well above the biomedical implant, Lab-on-Chip, and wearable microfluidic application requirements. For example, inner ear drug delivery applications experience backpressure characterized by the endolymphatic pressure; of 0.53 kPa in guinea pigs [106]. The valve's forward-flow opening pressure was recorded to be 2.1 kPa, satisfying our goal to achieve a passive valve under a low

flow rate regime. The results of **Figure 2.9** also demonstrate a relationship between magnetic nanoparticle concentration and forward flow rate, making this a design parameter to be tuned for the specific application.
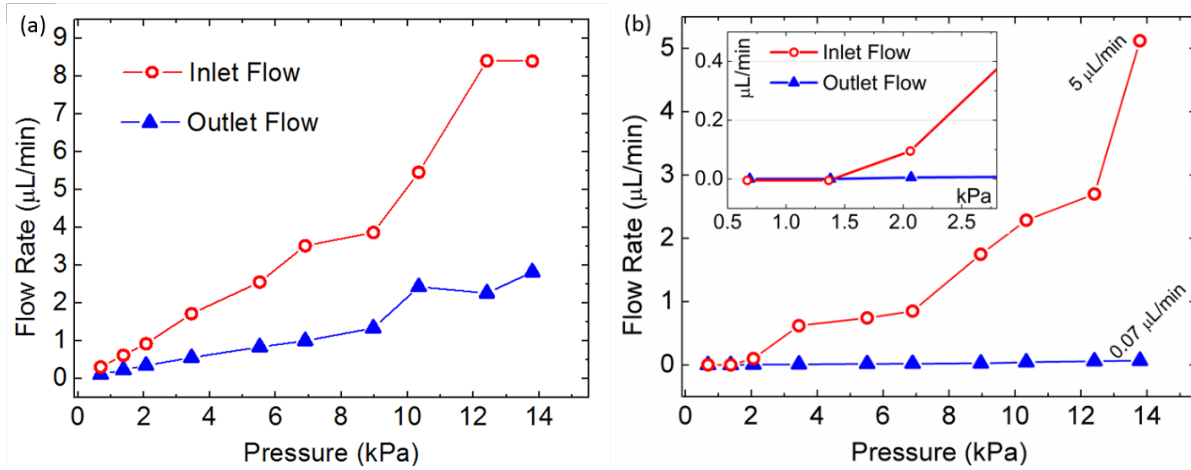
Figure 2.9: Flow rates for forward and backward flows for **(a)** 50%, **(b)** 75% wt/wt Fe_3O_4: PEG microcapsules with diameters of 750 μm as flow rectifying valves.

An important feature of the presented passive valve is its ability to block diffusion. Diffusion tests with fluorescence on the outlet side and fresh water on the inlet side are shown in **Figure 10**. In the absence of the valve, the fluorescence intensity on the inlet side reached the maximal value within one hour. The concentration of the fluorescein solution can be represented as [107].

$$\log(C) = -15.20 + 0.957 \times \log(FI)$$
(**Equation 2.10**)

where C is the concentration of fluorescein, and FI is the fluorescence signal.

The equation can be rewritten as

$$C_1/C_2 = (FI_1/FI_2)^{0.957}$$
(**Equation 2.11**)

where C_1 and C_2 are two concentrations of fluorescein salt, FI_1 and FI_2 are the fluorescence signals.

35

Over 1 hour, the diffusion rate with the valve was measured to be 0.04% of the diffusion rate in the absence of the valve, indicating that the valve had successfully blocked 99.96% of the diffusion for the measurement period. This demonstrates robust sealing of the microcapsule wall to the tubing wall in the no-flow state, providing a unique capability in passive valves.
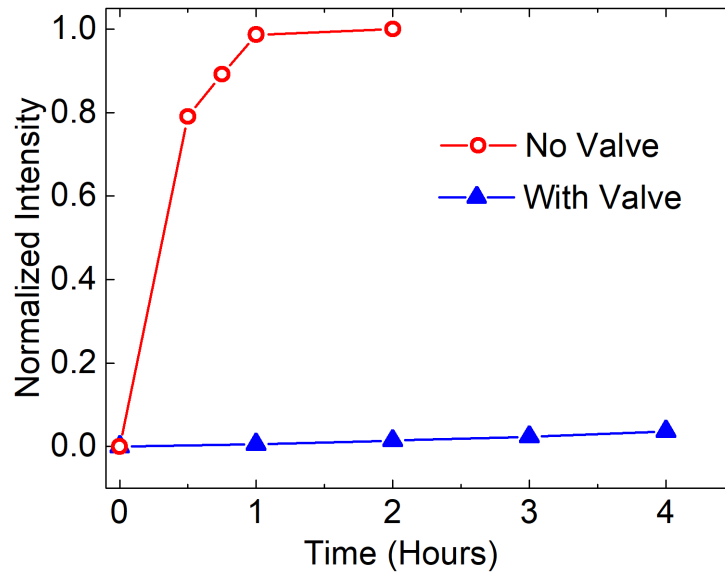
Figure 2.10: Normalized intensity trends with/without the valve are compared. The diffusion was observed by recording the fluorescence intensity variation over time at the inlet and the outlet ends of the valve using a fluorescence microscope (LEICA DM 2500) at 515 nm emitting wavelength.

2.6 Conclusion

In this work, a one-of-a-kind passive and biocompatible valve was developed. The in-line and scalable design is based on a microcapsule with a core of magnetic nanocomposite encapsulated with a soft polymeric impermeable shell. The microcapsule with the magnetic field gradient source demonstrates flow-rectifying capabilities along with an ultra-low forward-flow opening pressure. The forward-to-backward flow ratio was measured to be 71.4 at 14 kPa for valves based on 4 mm long microcapsules with concentration of 75% wt/wt Fe_3O_4: PEG. The valve's forward-flow opening pressure was measured to be

an astonishingly low 2.1 kPa, allowing microfluidic devices to easily actuate flows in the desired direction. The valve also successfully blocked 99.96% of diffusion, one of the major unsolved problems for passive microvalves, making contamination-free microfluidic applications possible. Future work on this valve may focus on further miniaturization and customization of the microcapsule, and alternative polymerization techniques of the polymer shell over the magnetic core. The magnetic-nanocomposite-core microcapsule may have utility in a variety of microfluidic channels to achieve robust flow rectification for precise flow control and diffusion blocking for contamination prevention.

Chapter 3

Pressure Regulator for Pumping in Microfluidics

3.1 Current Pumps in Microfluidic Cell Culture

Pumps provide the necessary driving force for working fluids in microfluidic systems. Precise and tunable pumping for microfluidic applications is commonly achieved with displacement-based (e.g., syringe or peristaltic pumps) or pressure-controlled techniques. However, it can be challenging to integrate these large form-factor devices and accompanying peripherals into confined environments, such as incubators. Thus, miniaturized approaches to simplify the pumping process have also been widely explored. For example, a commercial palm-top refillable iPrecio infusion pump has been used to maintain cells in culture. However, the pumps were expensive and could not be customized. Alternatively, passive pumping, including hydrostatic and surface tension-based methods, is low-cost and easy to use but lacks long-term stability, deeming them unsuitable for microfluidic culturing applications (> 24 h). Microelectromechanical systems (MEMS) approaches have also been used to create microfabricated pumps. Although these micropumps can provide the long-term control required for lab-on-chip applications, the complexity of the fabrication procedures can make customization and implementation impractical.

3.1.1 Relevance of Pumps in Microfluidic Systems

Microfluidic systems have revolutionized as a powerful platform in cell culture, as they provide controlled flow rate over the cellular microenvironment. A key aspect to the functionality of these systems is the driving source, often a pump, to facilitate the controlled delivery of reagents to cells and waste removal. In microfluidic systems, control over fluid flow is typically achieved via displacement-based or pressure-controlled pumping schemes [108], [109], [110]. The displacement-based mechanism is often seen in syringe and peristaltic pumps. Syringe pumps use the rotary motion of mechanical screws to dispense fluid from a syringe barrel at a controlled flow rate (Q), while peristaltic pumps employ a cam mechanism to push or pull fluids through compliant tubing to directly control Q [109], [111]. Although syringe and

peristaltic pumps are frequently used due to their robust flow control capabilities and compatibility with standardized components (e.g., syringes, fittings, and tubing), they can be challenging to integrate into confined environments. In addition, the mechanical oscillations of their rotary motor or cam mechanisms can introduce undesired flow pulsations that result in cell damage [112], [113], [114]. Controlled pressure pumping schemes create a defined pressure drop (ΔP) across microfluidic networks to drive fluid flows. These pumping schemes are typically seen in electroosmotic pumps and pneumatic pressure driven pumps. Electroosmotic pumps offer continuous, pulse-free flows, along with compact size, making them an excellent alternative for microfluidic flow control. However, the high voltage requirement of the pumps may necessitate additional voltage control equipment. Moreover, the high voltage may lead to electrolysis of the cell media, creating bubbles for disruption [115]. When connecting external pneumatic pressure sources, the pressure-driven pumps offer high responsive flow rates. These flow rates are governed by the hydraulic analogy to Ohm's Law, $Q = \Delta P \cdot R^{-1}$, where R is the hydrodynamic resistance of the network [116], [117]. Because of the intrinsic damping nature, pneumatic approaches suffer less from flow pulsations compared to displacement-based methods. However, they also require more complex peripheral equipment, such as a dedicated high-pressure air source (e.g., laboratory air), a closed-loop pressure controller, or precise pressure/flow sensors [118], [119]. Consequently, pneumatic methods are rather difficult to integrate into cell culture environments [6]. Both displacement and controlled-pressure techniques offer excellent flow control capabilities and can be programmed to dynamically adjust flow profiles, including ramped, periodic, pulsed, or even reversed flows. Nevertheless, these features are not often needed in standard microfluidic culture applications. In fact, a constant flow rate is generally used to maintain or stimulate cultured cells [120], [121]. The experimental need for a single controlled flow rate allows us to forgo some of the advanced flow functionalities in favor of a simple and portable pumping solution.

3.1.2 Performance evaluation of a portable pump in microfluidic cell culture

Several key aspects we value when creating a suitable and portable single flow rate system for microfluidic cell culture applications include the accessibility of the system, long-term pumping capability, and simplicity of fabrication. For instance, Sasaki introduced a palm-top system with an infusion micropump

(iPrecio SMP101-L, Primetech, Tokyo, Japan) [122]. However, the pump was expensive (>$300), one-time use, and could not be customized. Passive pumping, on the other hand, provides a more cost-friendly and portable alternative. Unfortunately, despite the lower costs and ease of use, passive pumping mechanisms usually lack control and stability over the flow rates during pumping, making them unsuitable for long-term culturing (> 24 hours) [123], [124]. As such, researchers have implemented microelectromechanical (MEMS) fabrication techniques to enable micropumps [3], [34]. Although these micropumps can provide the long-term control required for lab-on-chip applications, the complexity of the fabrication procedures can make customization and implementation impractical.

3.1.3 Pressure regulating for pumping in microfluidic cell culture

Researchers have utilized a step-down pressure regulator coupled with a compressed air source with higher pressure. The pressure regulator stabilizes and output consistent downstream pressure, which is often coupled with a known stabilizing microchannel to achieve consistent and precise flow rates. Different mechanisms to regulate down the pressure have been proposed by researchers. These mechanisms include diffusion, electromagnetic, mechanical, electrostatic, piezoelectric, and thermopneumatic. The benchmark of some literature examples are covered in **Table 3.1**.

Regulation Method	Description	Cost	Size (mm)	Pressure Accuracy (kPa)	Input/Output Pressures (kPa)	Stability	Compressed Air Line / Power Supply	Commercial Product	Reference
Diffusion	3D-printed casing components were used to make a pressure regulator that can reduce 1-2 bars of pressures by 0-1 bars. Pressure regulating is dictated by the permeability of PDMS membranes.	Not reported	Φ35 x 24	Not reported	100-200 / 0-200	Not reported	Yes / No	No	Podwin 2018[1]
Electromagnetic	A miniaturized pressure regulating valve to lower pressure (glaucoma range) by employing a combination of solenoid/permanent magnet. Fluidic driving was not the major purpose of this work.	Not reported	9.2 x 9.2 x 3.1	Not reported	2.7-4 / 2.7	Not reported	No / Yes	No	Bae 2003[2]
Electromagnetic	Automated pneumatic setup with solenoid valves, pressure regulators, and relief needle valves. The marginal costs of increasing streams are lower than syringe pump networks.	> $700	Network of pressure components	3.5	280 / 3.5-28	Not reported	Yes / Yes	No	Bong 2011[3]
Electromagnetic	The electromagnetically-controlled device regulated input pressure by applying different current to the coil (71Ω). The switching frequency of the valve can be up to 30 Hz. The device can operate at inlet pressure up to 200 kPa (with 300mA current).	Not reported	10 x 10 x 4.3	Not reported	50-200 / 0-125	Not reported	Yes / Yes	No	Fu 2003[4]
Electromagnetic	Kudasik utilized a solenoid valve, a pressurized cylinder, and a buffering cylinder to stabilize required pressures.	Not reported	Network of pressure components	0.1 kPa	1400-2000 / 100-700	0.1 kPa over 18h	Yes / Yes	No	Kudasik 2010[5]

Table 3.1 Benchmark table of compressed-air based flow driving set ups [16], [66], [125], [126], [127]

Regulation Method	Description	Cost	Size (mm)	Pressure Accuracy (kPa)	Input/Output Pressures (kPa)	Stability	Compressed Air Line / Power Supply	Commercial Product	Reference
Electromagnetic	Liu et al. presented control methods, including Bang-Bang, proportional and pulse-width-modulation, and composite control, to electromagnetically control pressures in a micro chamber.	Not reported	3 x 3 x 1 (chamber)	3.15	220-280 / 150	3.15	Yes / Yes	No	Liu 2017[6]
Electrostatic	Anjewierden reported a parylene-based electrostatic device that can operate with pressures up to 40 kPa. Flow rate average recorded at 1.05 mL/min. The flow rate is also dependent on parylene membrane's thickness.	Not reported	20 x 75 x (30, estimated)	Not reported	0-40 / 0-40	Not reported	Yes / Yes	No	Anjewierden 2012[7]
Electrostatic	Yıldırım created an electrostatically-operated normally-closed parylene microvalve that can withstand up to 20 kPa. The actuation chamber for the valve has a radius of 410μm.	Not reported	Not reported	Not reported	0-20 / 0-20	Not reported	Yes / Yes	No	Yıldırım 2012[8]
Electrostatic	Yoshida created an electrostatic microvalve to regulate inlet pressure up to 40 kPa without leakage. By manipulating the duty ratio of the microvalve, Yoshida was able to deliver desired flow rates of methanol.	Not reported	5.5 x 12.5 x 2.3	Not reported	0-40 / 0-40	Dependent on duty ratio	Yes / Yes	No	Yoshida 2010[9]

Table 3.1 Benchmark table of compressed-air based flow driving set ups (cont'd)[70], [85], [128], [129]

Regulation Method	Description	Cost	Size (mm)	Pressure Accuracy (kPa)	Input/Output Pressures (kPa)	Stability	Compressed Air Line / Power Supply	Commercial Product	Reference
Mechanical	Begolo 3D-printed a device with a pumping lid that creates the differential pressure for driving fluids in microchannels. The device was printed with multi-material 3D printer with sealing elastomers built-in.	Not reported	14.73 cm³	2.5	NA / <20	30% over 7 hrs	No / No	No	Begolo 2014[10]
Mechanical	Beswick Engineering provides a commercially available pressure regulator specifically for low pressure applications. The website offers material options for different components of the pressure regulator.	$100	Φ26 x 50	3.5	<3500 / <350	0.1% full scale	Yes / No	Yes	Beswick Engineering[11]
Mechanical	Mavrogiannis introduced system with one inlet and four outlets for microfluidics applications. The flow rates are dictated by the incorporated commercial pressure regulators and fluidic resistances of coupled capillaries. We calculated the stability based on flow fluctuations.	$500	Network of pressure components	3.5	<350 / <100	6.70%	Yes / No	No	Mavrogiannis 2016[12]
Mechanical	**We utilized a mini air pump to supply a pressure to be regulated by our 3D-printed µPR to create an affordable device for flow control. Cost of µPR alone is $1.19.**	**$6.68**	**Φ12 x 20**	**0.7**	**60 / 1-10**	**2% set point**	**No / Yes**	**No**	**Our work**

Table 3.1 Benchmark table of compressed-air based flow driving set ups (cont'd)[130], [131], [132], [133]

43

Regulation Method	Description	Cost	Size (mm)	Pressure Accuracy (kPa)	Input/Output Pressures (kPa)	Stability	Compressed Air Line / Power Supply	Commercial Product	Reference
Mechanical	Thrugood introduced an affordable flow delivery system for microfluidics using a latex balloon reinforced by nylon stockings. The balloon can be manually squeezed to reach desired pressures.	$2	Φ250	Manual	2.5-25 / 2.5-25	9.4% over 9h	No / No	No	Thurgood 2019[13]
Not reported	A usb-powered low-pressure pump up to 50 kPa. The device is compatible with LabVIEW can be coupled with control valves for multi-inlet switching.	$2,500	100 x 60 x 30	Not reported	NA / 0-50	Not reported	No / Yes	Yes	Dolomite Mitos Fluika Pump[14]
Piezoelectric	The device comes with pressure and vacuum inlets can be coupled with flow sensors for driving flows in both directions.	>$20,000	240 x 223 x 80	0.001	150-1000 / 0-20	0.001kPa	Yes / Yes	Yes	Elveflow Systems[15]
Piezoelectric	Evans created a feed-back controlled system with a spring-pressurized reservoir (37mL) as air tank, a piezoelectric microvalve, and a flow sensor to deliver desired flow rates.	Not reported	45 x 85 x 34	Not reported	0-15 / 0-15	3.22% Flow	No / Yes	No	Evans 2010[16]
Piezoelectric	Nafea utilized a pressurized balloon (up to 13 kPa) and a normally-closed piezoelectric microvalve to deliver flows. The device is wirelessly powered by an inductor-capacitor circuit at 10 kHz.	Not reported	22 x 42 x 4	Not reported	13 / Not reported	Not reported	No / Yes	No	Nafea 2018[17]

Table 3.1 Benchmark table (cont'd) [24], [134], [135], [136], [137]

Regulation Method	Description	Cost	Size (mm)	Pressure Accuracy (kPa)	Input/Output Pressures (kPa)	Stability	Compressed Air Line / Power Supply	Commercial Product	Reference
Thermo-pneumatic	Chee utilized an external coil to heat an air reservoir locally to obtain the pressure required to drive flows. The maximum pressure obtained in the device was 0.4 kPa with frequency at 81.6 kHz. Variations in pumping strokes were documented at 2.8%	Not reported	22 x 7 x 4	Not reported	NA / 0-50	2.80%	No / Yes	No	Chee 2015[18]
Thermo-pneumatic	Cooney powered a pump with a coil locally heating the reservoir. The flow rates required a warm-up stage, where a 18% deviation was reported. The device, powered by an alkaline 9V battery, could deliver 1.4 uL/min for at least 4.5 hours.	Not reported	Φ20 x 1 (pump only)	Not reported	NA / 7-42	18%	No / Yes	No	Cooney 2004[19]
Thermo-pneumatic	Henning created a mass flow controller/pressure regulator by combining a normally-open and a normally-closed valve. The device was intended to regulate ultra-low pressure.	Not reported	106 x 40 x 25	1% full scale	172-345 / 1.3	0.1% full scale	Yes / Yes	discontinued	Henning 1998[20]

Table 3.1 Benchmark table of compressed-air based flow driving set ups (cont'd)[26], [93], [138]

The aforementioned pressure regulating mechanisms as pumps can be categorized into active and passive. Active pressure regulating mechanisms usually involve pressure or flow sensors to ensure the output pressure stays at the desired level. Since the designated usage of the pump is to output a constant pressure for steady flow driving, the interesting mechanisms would be the passive types - mechanical and diffusion. Mechanical pressure regulators depend on the balance between the forces. Diffusion-based pressure regulating was realized by Podwin via the gas permeability of the PDMS membrane [125], [139]. Mechanical pressure regulators are preferred over diffusion-based pressure regulating due to the stability of the output pressure.

3.2 Technology gap and significance

Here, we introduce a simple and accessible pneumatic pumping platform that uses a 3D-printed micro pressure regulator (µPR) to provide a tunable ΔP that controls the flow rate in a microfluidic channel network. As 3D printers have become more accessible for research laboratories [140], we anticipate that this 3D-printed µPR can be fabricated and assembled in any research laboratory and tailored to achieve application-specific flow requirements. Our µPR uses a force-balance mechanism to reduce the pressure supplied by a battery-powered miniature air compressor to a controllable pressure range relevant to microfluidic applications. We detail the design and fabrication of the µPR, establish output pressure control and stability, and demonstrate both successful cultures within a microfluidic channel and its dynamic control capabilities.

3.3 Concept and theory

a) A force-balance mechanism enables a range of regulated outlet pressure

Pressure regulators are commonly used in pneumatic circuits to reduce high-pressure air to a lower, controllable pressure setpoint for downstream applications. As with most manual pressure regulators, our 3D-printed µPR uses a force-balance mechanism and is designed to maintain a user-defined setpoint

suitable for standard microfluidic systems (~1-10kPa). As shown in **Figure 3.1**, the µPR consists of a high-pressure air chamber, low-pressure air chamber, and pressure control component. The high-pressure air chamber includes the closing (bottom) cantilever springs, the poppet valve, and the connecting rod. This chamber receives constant pressure from a miniature air compressor. The low-pressure chamber with the pressure sensing diaphragm outputs the regulated outlet pressure. The pressure control component consists of 3D-printed top cantilever springs and the control knob (a bolt and a pairing nut), which is used to control the outlet pressure as described below.
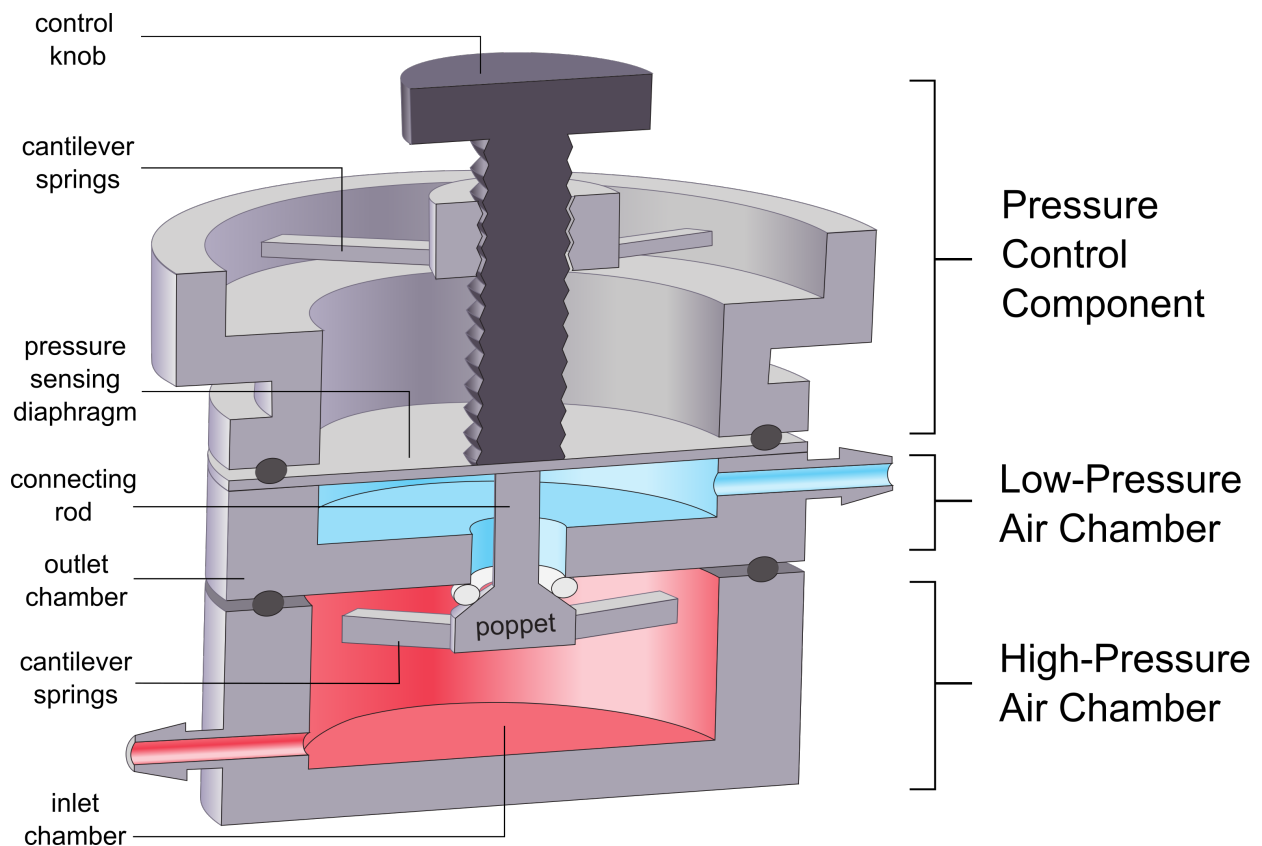

Figure 3.1: Cross-sectional schematic of essential components in the 3D-printed µPR. The high-pressure chamber (red) receives a constant high-pressure air supply from an external source. The low-pressure chamber (blue) outputs air at a constant low pressure. The outlet pressure is controlled by adjusting the pressure control component, consisting of cantilever springs and a control knob.

b) Operating phases of pressure regulator
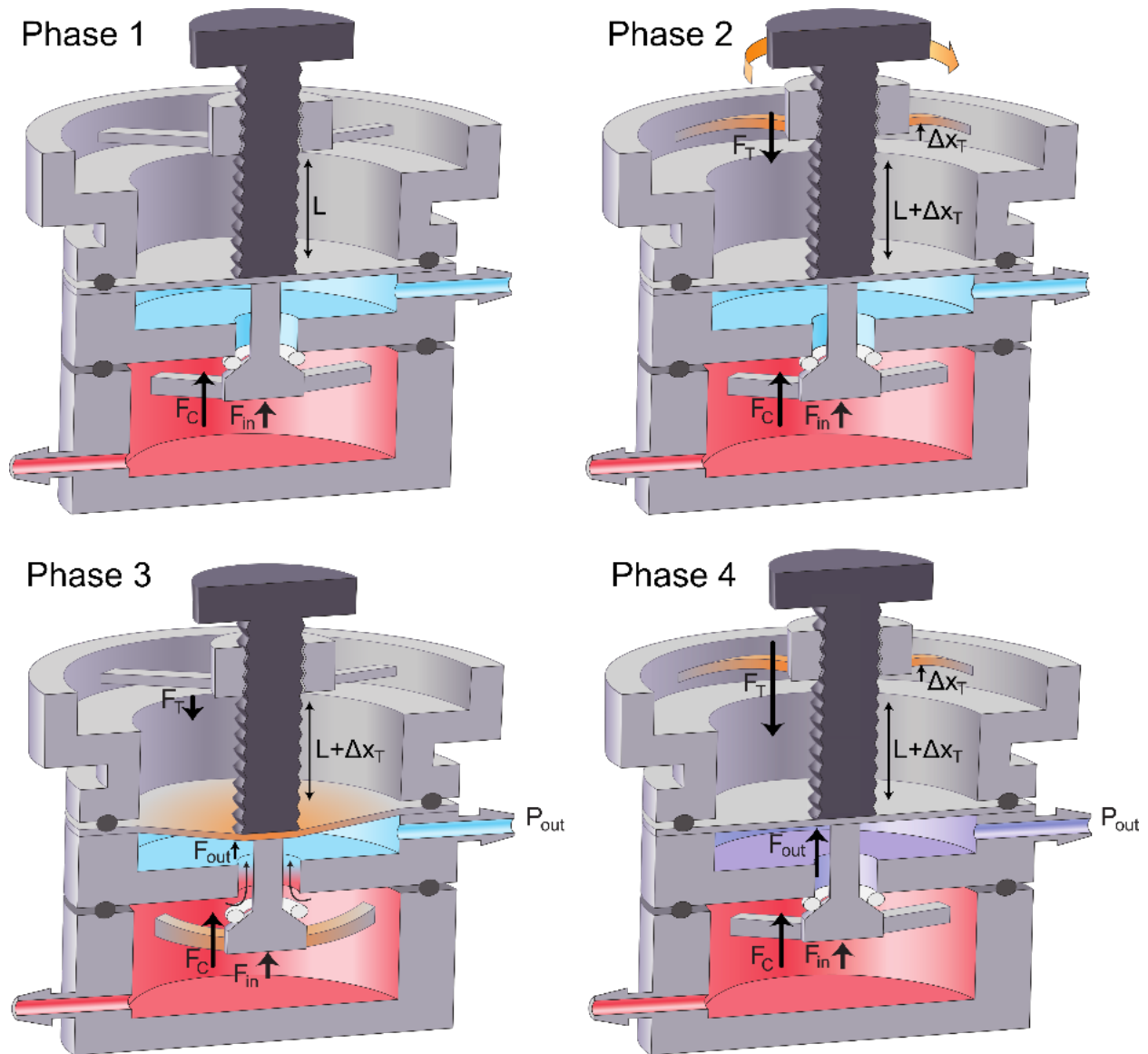
Figure 3.2: Depiction of the four phases of the pressure regulating process. During Phase 1, the air passage is fully closed, while we supply air at a constant high pressure. In Phase 2, the user turns the control knob to displace the top cantilevers. As the top cantilever restoring force (F_T) increases, the air passage between the chambers remains closed. In Phase 3, when F_T surpasses a certain threshold, the air passage opens. Finally, in Phase 4, the pressure in the low-pressure air chamber will reach the desired level indicated by the control knob and the passage will close. Once the pressure is set by the user, the device toggles between Phase 3 and Phase 4 to maintain the desired output pressure.

The operation of μPR can be described in four phases as shown in **Figure 3.2**.

Phase 1

Constant high-pressure air is supplied to the high-pressure chamber using a miniature air compressor. There are two closing forces present at this stage. The inlet pressure force (F_{in}) is an upward force generated by the inlet pressure acting on the poppet. The closing cantilever spring force (F_C) is a constant upward force generated by the displacement of the non-adjustable bottom cantilever springs during assembly. These upward forces press the poppet to the seat and close the air passage between chambers. In this phase, the bolt length under the nut is L and the tip of the bolt rests against the pressure-sensing diaphragm without exerting a downward force.

Phase 2

As we turn the control knob clockwise, the bolt length under the nut is increased to $L + \Delta x_T$ and the top cantilever springs are displaced upward from their relaxed state by Δx_T. This upward displacement of the cantilever springs generates a downward restoring force ($F_T = k_T \cdot \Delta x_T$) on the sensing diaphragm. During this phase, the air passage is still sealed by upward forces (F_{in} and F_C), as $F_T < F_{in} + F_C$.

Phase 3:

When the control knob is rotated further, F_T overcomes the upward forces ($F_{in} + F_C$) and the bolt tip displaces the pressure-sensing diaphragm and the connecting rod. The motion of the connecting rod unseats the poppet valve and opens the air passage, allowing high-pressure air to enter the low-pressure chamber. The pressure (P_{out}) in the low-pressure chamber exerts an upward force F_{out} on the bottom surface of the pressure-sensing diaphragm (area A_d), $P_{out} = F_{out} \cdot A_d^{-1}$.

Phase 4:

P_{out} increases until F_{out} and other upward forces F_{in}, F_C combine to match F_T as shown in **Equation 3.1**. These upward forces lift the poppet valve and block air flow between chambers (**Figure 3.2**). This allows us to set P_{out} by changing the top cantilever spring force ($F_T = k_T \cdot \Delta x_T$), which can be adjusted by the rotational position of the control knob. Since P_{out} is used to pump liquid flow in a downstream primed

microchannel, the exhaust due to pumping decreases P_{out} and triggers μPR to re-enter <u>Phase 3</u> to allow high-pressure air to compensate for the pressure loss. Once Δx_T is set by the control knob, the μPR toggles between <u>Phases 3 and 4</u> to maintain a stable P_{out}.

$$F_T = F_{out} + F_{in} + F_C \qquad \textbf{(Equation 3.1)}$$

Here, the top cantilever spring force $F_T = k_T \cdot \Delta x_T$; k_T is the spring constant of the top cantilever spring, with Δx_T being the spring displacement. The outlet pressure force, $F_{out} = P_{out} \cdot A_d$; P_{out} is the outlet pressure, and A_d is the area of the sensing diaphragm. F_{in} is the inlet pressure force on the exposed area of the poppet, while F_C is a constant closing force from the bottom cantilever springs.

Equation 3.1 can be simplified because the closing cantilever springs in the high-pressure chamber are not adjustable *and* F_C is constant. F_{in} is constant as long as we supply a constant input pressure to the high-pressure chamber. Because both F_{in} and F_C are constants, we can control F_{out} (thus P_{out}) by manipulating the F_T applied to the diaphragm. F_T scales linearly with the displacement (Δx_T) of the top cantilever springs, hence we can tune P_{out} by adjusting the angular position of the control knob.

3.4 Materials and methods

<u>a) Material selection for the μPR</u>

The structural components of the μPR, including the inlet (high-pressure) and outlet (low-pressure) chambers and the pressure control component, were 3D printed using the Formlabs Form 2 stereolithography printer (Formlabs Inc., Somerville, MA, USA). We chose Dental SG resin (Formlabs Inc., Somerville, MA, USA) as the building material due to its gas-impermeable characteristics and Class I biocompatibility (EN-ISO 10993-1:2009/AC:2010). This would allow us to implement the device for cell culture applications. We picked Viton fluoroelastomer O-rings (shore 60A) (McMaster Carr, Elmhurst, IL, USA) as the poppet valve sealing material to prevent pressure leakage between high and low-pressure

chambers. Polyimide with 100-µm thickness was chosen as the pressure sensing diaphragm due to its chemical stability and material robustness.

b) Fabrication of the µPR

The Viton fluoroelastomer (shore 60A) O-ring was fitted over the connecting rod adjacent to the poppet valve of the high-pressure inlet chamber as shown in **Figure 3.3(a) (i)**. An 8-mm-ID/10-mm-OD natural rubber (shore 70A) O-ring (McMaster Carr, Elmhurst, IL, USA) was then placed in the outer groove of the inlet chamber. The low-pressure outlet chamber, shown in **(ii)**, was placed over the inlet chamber with the connecting rod extending through the cavity to form the cross-chamber air passage. Next, a 100-µm thick Kapton (Gizmo Dorks LLC, Temple City, CA, USA) was placed onto the outlet chamber as the pressure sensing diaphragm, in contact with the connecting rod. As shown in **(iii),** an O-ring was placed on top of the diaphragm to help seal the top of the outlet chamber. The pressure control component with built-in cantilever springs was then stacked onto the diaphragm. These cantilevers were 0.5 mm wide, 0.5 mm thick, and 5 mm long. An M2 nut (McMaster Carr, Elmhurst, IL, USA) was glued to the cantilever springs with epoxy adhesive (ClearWeld™ Professional, J-B Weld Company, Sulphur Springs, Texas, USA) **(iv)**. As shown in **(v)**, an M2 bolt was threaded into the nut. A 3D-printed pointer was added to the hexagonal socket head to create the control knob. A laser-cut, 24-position acrylic dial was attached to the pressure control component using pressure-sensitive adhesive (PSA, 3M 468MP Adhesive Transfer Tape, 3M Company, Maplewood, MN, USA). The dial provided indications for rotational positions in 15° increments. Finally, 3D-printed clamps were used to compress the outer O-rings sandwiched between the structural components and complete the assembly as shown in **(vi)**. The assembled device is 12mm in diameter and 20mm in height. **Figure 3.3(b)** shows an image of the assembled device next to a US dime for scale.
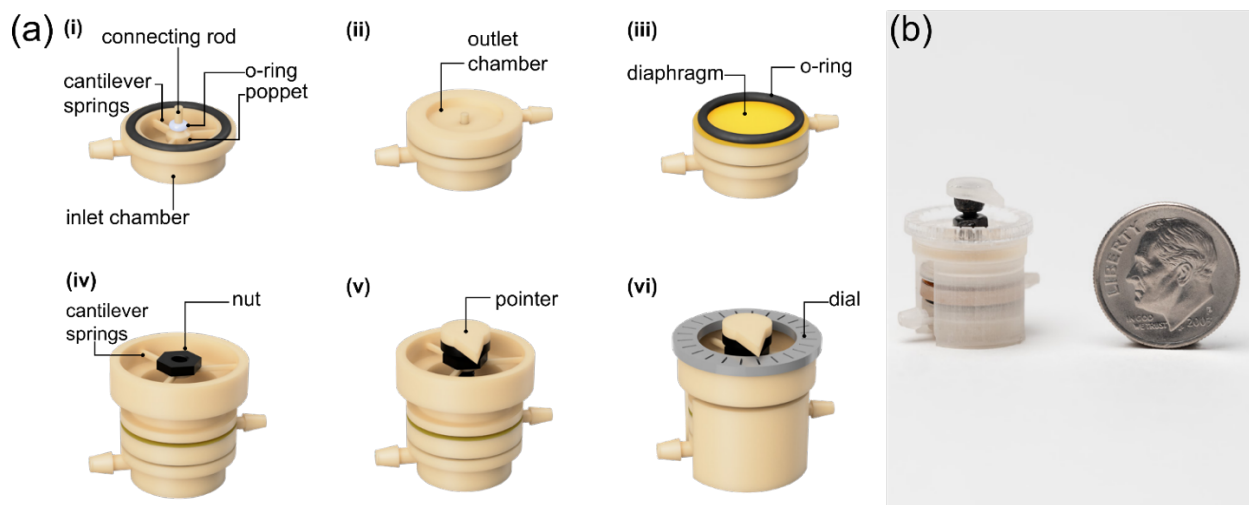
Figure 3.3: (a) Schematic view of the 3D printed μPR and fabrication workflow. (i) The high-pressure air inlet chamber includes a poppet valve, a sealing O-ring (white), and a connecting rod. (ii) The low-pressure air chamber is placed on top of the inlet chamber. (iii) A Kapton diaphragm (yellow) and an O-ring (black) are placed atop the outlet chamber. (iv) The pressure control component, consisting of three built-in cantilevers and a threaded nut, is positioned on top of the O-ring. (v) An M2 bolt with a 3D-printed position indication pointer is threaded into the nut. (vi) The device is then sealed using two 3D-printed compression clamps to achieve an air-tight assembly (Φ12mm x 20mm) and a laser-cut position dial is added. **(b)** Image of the assembled 3D-printed μPR next to a United States dime for scale.

c) Microfluidic channel fabrication

(Poly)dimethylsiloxane (PDMS, Sylgard 184, Dow Inc., Midland, MI, USA) microchannels were fabricated using standard soft-lithography techniques [141], [142]. SU-8 2100 (Kayaku Advanced Materials, Westborough, MA, USA) was spin-coated onto a 4" silicon wafer, soft-baked, and exposed to UV light through a transparency mask (CAD/Arts Services Inc., Bandon, OR, USA) to define channel features and post-baked at 95ºC. The photoresist was then developed (Kayaku Advanced Materials, Westborough, MA, USA). A PMMA sheet with rectangular openings (length = 75 mm, width = 25 mm) was attached to the wafer using PSA to create a molding cavity with a defined height. Upon attachment of the PMMA ring, the mold was then filled with degassed PDMS pre-polymer (10:1 base to catalyst ratio by mass) and cured on a hotplate for 1 hour at 80°C. The PDMS block was then removed from the mold and access ports were cored with a 1-mm biopsy punch (World Precision Instruments, Sarasota, FL, USA).

d) COMSOL flow simulation setup

A 3D simulation was performed using the laminar flow physics (stationary) module in COMSOL Multiphysics. Microchannel geometry (20-µm height, 100-µm width, and 32-cm length) was applied with the material set as water. Pressures (P = 1-10 kPa) are applied to the inlet of the microchannel geometry, while the outlet pressure is defined as atmospheric (P = 0) with suppressed backflow. The other walls in the simulation setup are assigned no-slip boundary conditions.

e) Pressure and flow rate measurement

The general experimental setup featured a µPR and a PDMS microfluidic channel (20-µm height, 100-µm width, and 32-cm length). We supplied pressure to the µPR with a miniature DC air compressor SX-2 (Binaca Pumps, Temecula, CA, USA) operating at 3V and 0.09A. The outlet of the µPR was connected to a three-way connector, with one end feeding the inlet of the PDMS microfluidic channel and the other connected to a Honeywell pressure sensor (TBPDANS005PGUCV, Honeywell International Inc., Charlotte, NC, USA). Silicone tubing (2-mm ID, 5-cm length) was used to connect these components. The PDMS microchannel was primed with a solution of blue dye (McCormick Inc., Baltimore, MD, USA) in deionized water to improve contrast.

f) Characterization of outlet pressure vs control knob position

This characterization followed the aforementioned experimental setup. The Honeywell pressure sensor (TBPDANS005PGUCV, Honeywell International Inc., Charlotte, NC, USA) allowed the characterization of P_{out} based on the rotational position of the control knob. The control knob is turned by 15º increments (indicated with the acrylic dial) while P_{out} is being measured. P_{out} is then allowed to stabilize for 5-minutes for each position after turning. A full cycle of the calibration process included clockwise rotational turns (P_{out} increased from 1 to 10 kPa) and counterclockwise turns (P_{out} decreased from 10 to 1 kPa). 15 full cycles are used to calibrate the outlet pressure readings versus the knob position. To quantify the stability of the regulated pressures, the pressure data from the sensor are collected over 1000 minutes for three designated pressures (P_{out} = 1, 5, and 10 kPa), covering the low, medium, and high set points of the range.

g) Cell culture of HUVECs in μPR microfluidic platform

Detailed design and fabrication of the barrier platform have been described in our group's previous work [143], [144]. The cell culture platform consists of the top and bottom microchannels, separated by an ultrathin nanomembrane (SiMPore Inc., Rochester, NY, USA). The nanomembrane has a thickness of 100 nm and pore size of 60 nm. The device has a core open-well module known as the m-μSiM which can be reconfigured into a fluidic device by adding a flow module into its well and sealing it magnetically using two housings with embedded magnets. The flow module is fabricated using the standard soft lithography method and housings are fabricated using a laser cutter (H-series 20x12, Full Spectrum, CA, USA) [143]. The dimensions of the top channel were, h = 200 μm, w = 1.5 mm, and l = 5 mm, and the bottom channel are, h = 150 μm, w = 2-6 mm, and l = 15 mm. The flow from the media reservoir is connected to the inlet of the top channel using tubing and gauge 21 dispensing tips (Jensen Global, USA).

Before cell seeding, the nanomembrane is coated with 5 μg·cm^{-2} fibronectin (Corning Inc., Corning, NY, USA) for one hour at room temperature, and then rinsed with fresh cell media. Human umbilical vein endothelial cells (HUVECs) (Thermo Fisher Scientific, Waltham, MA, USA) are cultured in EBM-2 Basal Medium (Lonza Bioscience, Walkersville, MD, USA) supplemented with EGM-2 Endothelial Cell Growth Medium-2 BulletKit (Lonza Bioscience, Walkersville, MD, USA) and maintained in a tissue culture flask. Before use, cells were dissociated using TrypLE (Thermo Fisher Scientific, USA) for 3 min and centrifuged at 150 G for 5 min. After re-suspension, cells are seeded onto the membrane surface through the top microchannel and incubated for 1 hour to promote cell attachment.

The μPR is set to an output pressure of 8 kPa (ΔP = 8 kPa), which corresponds to a media flow rate of 1 μL·min^{-1} (shear stress of 0.02 dynes·cm^{-2} at cell monolayer) in the top channel for 24 hours. LIVE/DEAD stain (Thermo Fisher Scientific, Waltham, MA, USA) is used to assess cell viability based on the vendor's protocol. Labeled cells are imaged using an Olympus IX-81 fluorescence microscope with CellSens software (Olympus, Tokyo, Japan) with constant image capture settings across the experimental sets.
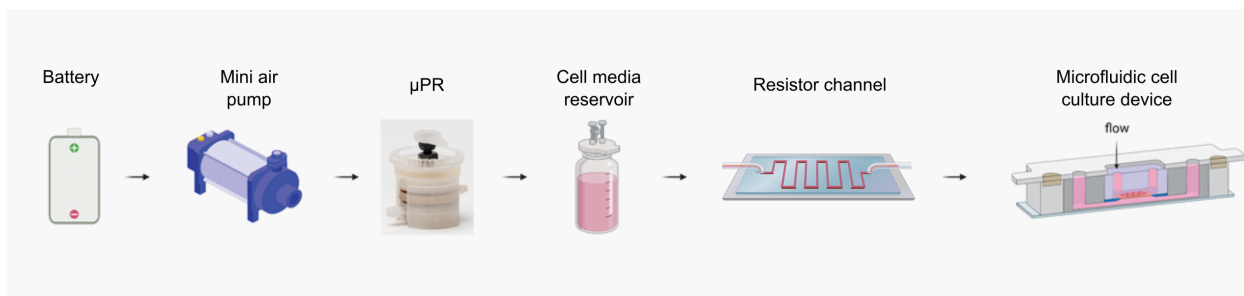
Figure 3.4 Schematic of the cell culture process workflow. The AA batteries were used to power the mini air pump, which a higher pressure to be regulated by the µPR. The µPR pressurized the sealed cell media reservoir to provide necessary media flow to the microfluidic cell culture device.

h) Dynamic flow control

A Y-shaped PDMS microchannel consisting of two 1-cm-long inlet channels and a 1-cm-long outlet channel was connected to two µPRs (P1 and P2) and two battery-powered micropumps. Each µPR was connected to a pressure sensor to measure pressure. P1 was maintained at 1.0 kPa while P2 was varied. We allowed 30 seconds for each P2 stage to provide a sequence of pressures: 1.0 kPa, 1.3 kPa, 1.0kPa, 1.5 kPa, 1.0 kPa, 1.8 kPa, and 1.0 kPa, for a total of 3 minutes and 30 seconds. The liquid-liquid interface between colored streams was recorded with an SMZ-168 stereomicroscope and its camera (Motic Co., ltd., Xiamen, China).

3.5 Results and takeaways

a) Calibration of the µPR, pressure stability, and driven liquid flow

A major goal of our pumping platform is to provide tunable pressure control while maintaining a portable setup. Therefore, we selected a miniature battery-powered air compressor instead of a compressed air line or a pressurized cylinder as the external high-pressure source. Since our µPR operates on the assumption of constant inlet pressure (see **Equation. 3.1**), we first confirmed that the pressure from the miniature air compressor. Running at 3 volts, the pump maintained a stable pressure (41 ± 0.02 kPa) over 5 days. Next, the relationship between the angular position of the control knob and the resulting outlet pressure is being investigated. As shown in **Figure 3.5(a)**, the control knob was rotated by 15˚ increments (corresponding to

increasing or decreasing Δx_T) and the output pressure was being measured. The data revealed two distinct slopes. In the first region of the calibration curve from the 1st to the 9th position (1.0 – 2.2 kPa), the slope was 0.15 kPa per 15° increment; and in the second region from the 10th to 20th position (2.6 kPa – 10 kPa), the slope was 0.70 kPa per 15° increment. These different slopes may be a consequence of the compressibility of the sealing O-ring on the poppet valve. That is, the O-ring may be partially in contact with the valve seat and limiting air flow between chambers (from positions 1 to 9). With increased rotation (positions 10 to 20), the O-ring detaches fully from the valve seat and air can flow between chambers with less resistance, thus creating a steeper slope relationship.
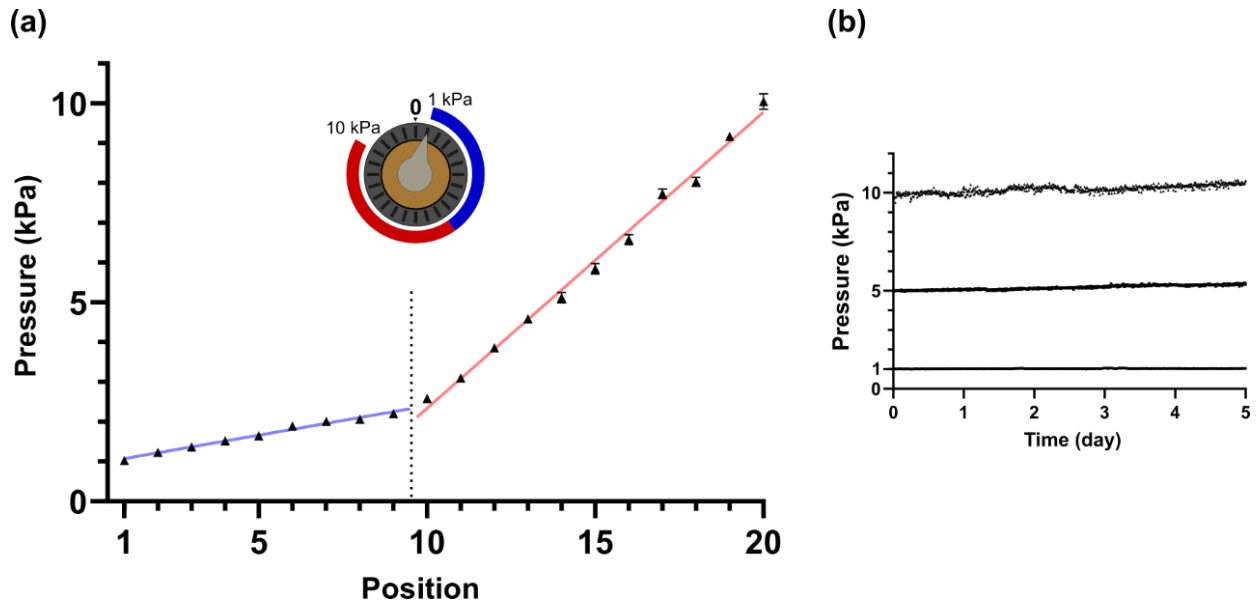

Figure 3.5: **(a)** Outlet pressure vs. control knob positions (15° steps). Pressures increase by 0.15-kPa increments between the 1st and 9th positions (blue), and 0.70-kPa increments between the 10th and 20th positions (red). **(b)** Outlet pressure stability test with pressures set to 1, 5, and 10 kPa, by turning the control knob to the 1st, 14th, and 20th positions following the calibrated results in (a). The pressure was measured over 16 hours to check the stability of the outlet pressure regulated by the device. The three outlet pressures were 1.0 ± 0.01 kPa, 5.1 ± 0.09 kPa, and 10.2 ± 0.16 kPa throughout the 5-day test.

To ensure controlled flow for culture applications, it is important to provide a stable pressure drop ($\Delta P = P_{out} - P_{atm}$) across the microchannel network. Here, the outlet pressure (P_{out}) regulated by the µPR helps establish ΔP. Using the calibration data acquired as shown in **Figure 3.5(a)**, we characterized the stability of P_{out} over 16 hours at three different setpoints, 1, 5, and 10 kPa. As shown in **Figure 3.5(b)**, the measured

outlet pressures were 1.0 ± 0.01 kPa, 5.1 ± 0.09 kPa, and 10.2 ± 0.16 kPa. The error to measured pressure

ratios for 1, 5, and 10 kPa were 1.0%, 1.8%, and 1.6% respectively, demonstrating the μPR's ability to

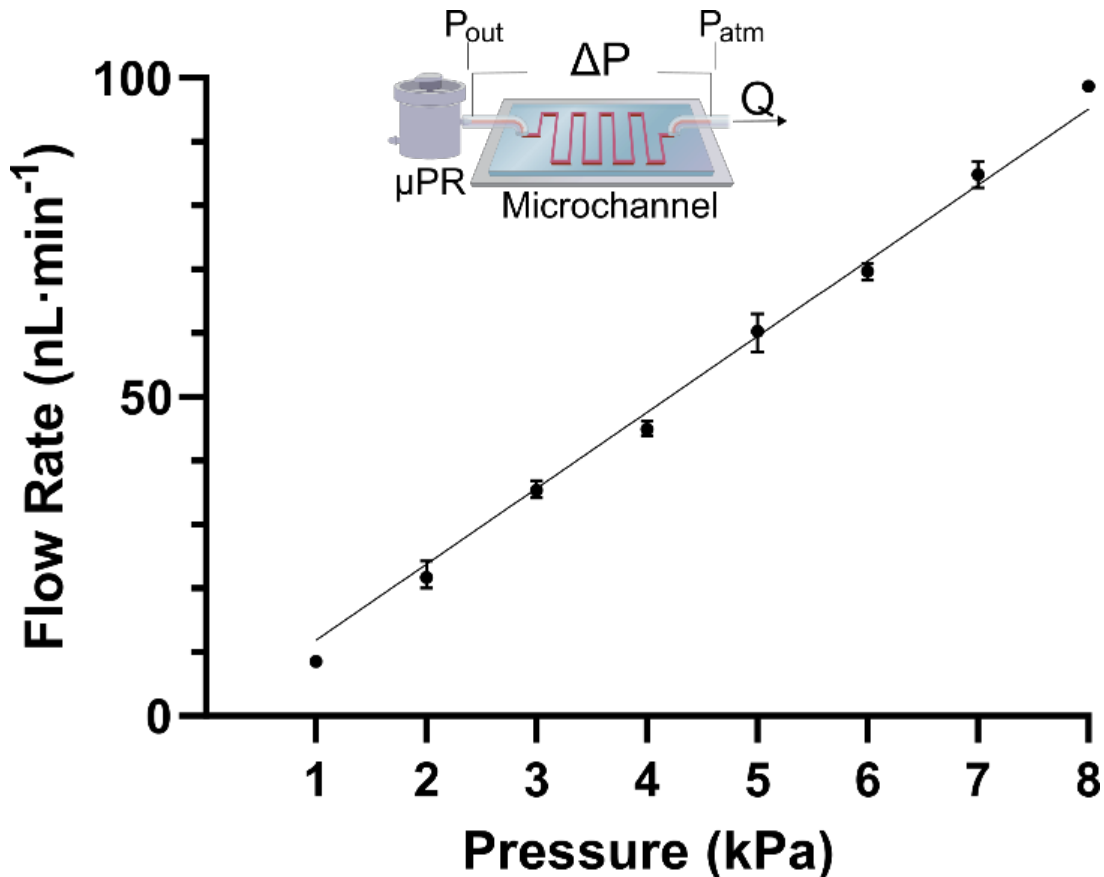provide tunable and stable pressures across the output range.

Figure 3.6: The inset shows the test setup, including the pressure regulator that creates a ΔP across the microchannel. ΔP is determined by the outlet pressure of μPR and the atmospheric pressure at the end of the microchannel. ΔP (1 to 8 kPa) covers flow rates from 9 to 100 nL·min^{-1}, yielding a slope of 12 nL·min^{-1}·kPa^{-1}. The straight line is drawn with the simulated response of flow rates vs. the outlet gauge pressures. $R^2 = 0.999$ is the correlation between the experimental data and the COMSOL simulation results.

Next, we explored how the μPR could be used to provide a stable pressure drop across a microfluidic

channel and produce flow rates practical for cell culture applications. The μPR was designed to support low

flow rates that can be difficult to achieve with commercial pressure regulators (e.g., 10 - 100 nL·min^{-1}) for

cell culture applications. The flow rates were measured in **Figure 3.6** for different outlet pressures to

investigate the μPR's capability of controlling the liquid flow. We introduced pressure drops, ΔP, from 1

to 8 kPa, using the μPR and measured flow rates ranging from 8.50 nL·min^{-1} to 98.7 nL·min^{-1}. We observed

an excellent correlation (R^2=0.999) between the COMSOL simulations and experimental flow rate measurements (ΔP from 1 to 8 kPa). The slope describing the relationship is 12 nL·min^{-1}·kPa^{-1}.

b) Microfluidic culture of Human Umbilical Vein Endothelial Cells (HUVECs)

In microfluidic systems, media perfusion is required because the small media volume in the channel is rapidly depleted of nutrients by metabolically active cells and must be replenished to maintain cell viability. To demonstrate the compatibility of our µPR to control fluid flow and maintain cells, we used the µPR to establish an endothelial monolayer in a tissue barrier model that we previously developed [143]. As shown in **Figure 3.7(a)**, the culture platform consists of two microchannels separated by a nanomembrane. The lower channel was filled with cell media while the top channel was supplied with flows driven by the µPR. The µPR induced a stable pressure drop of 8 kPa across the top culture microchannel, resulting in a constant 1µL·min^{-1} flow rate for introducing cell media from the reservoir into the culture region.

As expected, cells cultured in the device with media flow driven by the µPR were maintained alive and formed a confluent monolayer after 24 hours while the majority of cells in the static control died due to lack of cell media supply (**Figure 3.7(b)**). The live/dead staining showed a 98.5% survival rate in the µPR-supplied device whereas the static control (no media flow) had a 38.2% survival rate. These results confirmed the capability of the µPR to deliver stable flow rates and maintain a long-term culture of cells in microfluidic devices.

(a) Schematic of the cell culture setup
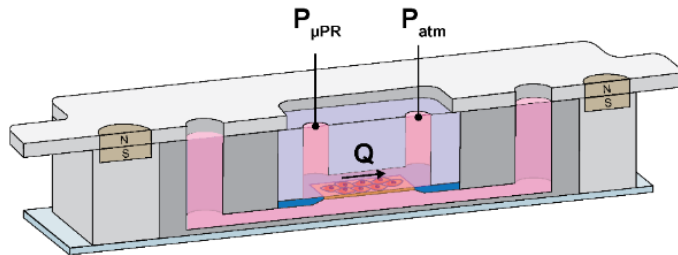
(b) Established endothelial monolayer after 24 hours

(i) Continuous flow by µPR
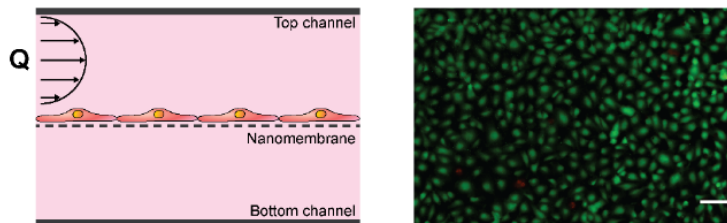
(ii) Control (No flow)
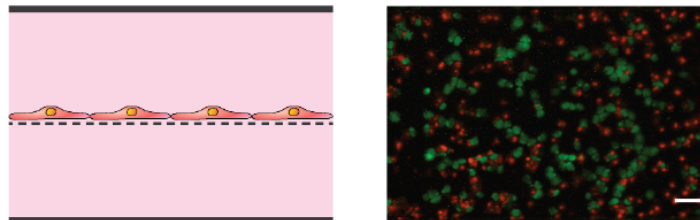
Figure 3.7: (a) The inset schematic illustration of the cell culture platform. A miniature air compressor supplies high-pressure air to µPR, which outputs a stable pressure drop (ΔP) across the top microchannel of the platform. This results in the flow of cell media from the reservoir into the microchannel. The platform consists of two microchannels separated by an ultrathin nanomembrane. Components of the platform can be disassembled after the experiment due to its reversible magnetic latching mechanism. We set the output of 8 kPa from the µPR to drive the culture media flow ($Q = 1$ µL·min^{-1}). **(b)** Cross-sectional view of the endothelial monolayer, and comparison of cultured cells in (i) dynamic culture (with the flow) and (ii) static culture (no flow). The cells were stained with LIVE/DEAD stain and fluorescence images were captured in green (viable cells) and red (dead cells). This demonstrates that the µPR can drive continuous flow vital for long-term cell culture and the formation of a confluent cell monolayer. Scale bars = 100µm.
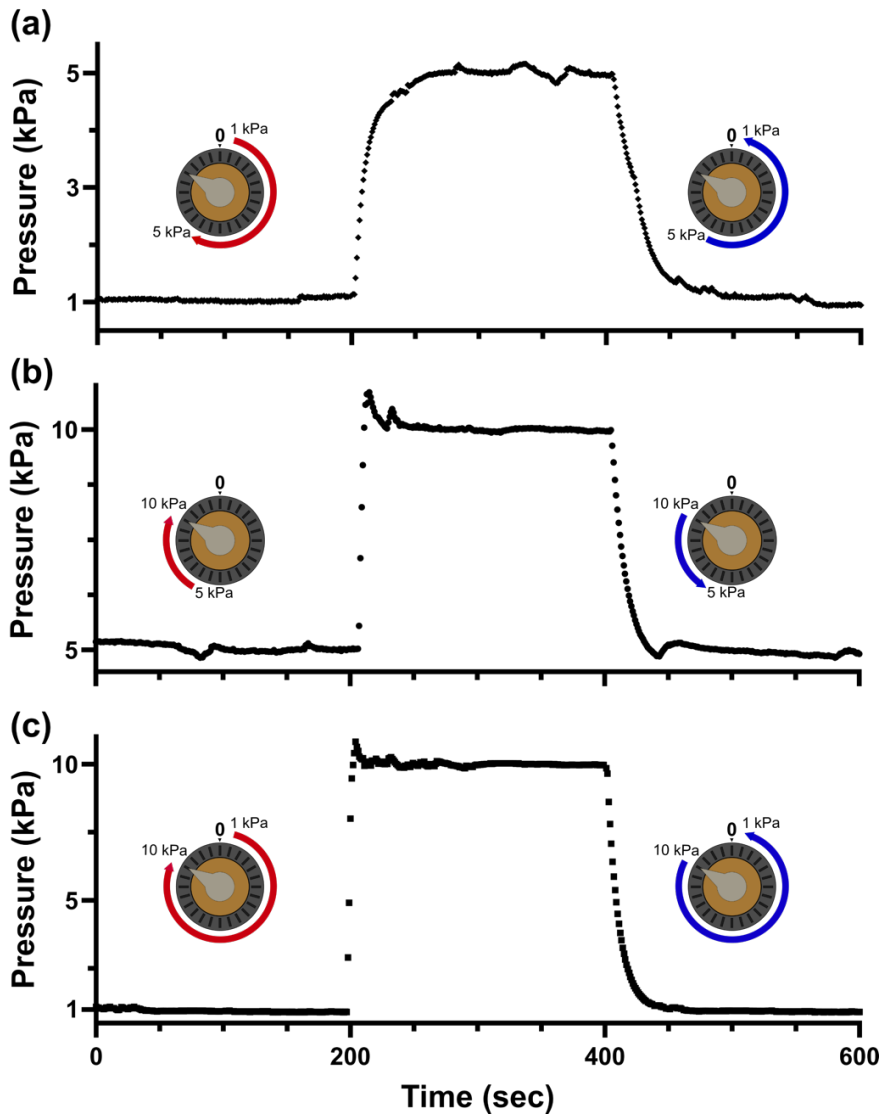
Figure 3.8: Dynamic responses of pressure patterns including, **(a)**. 1 to 5 to 1 kPa, **(b)**. 5 to 10 to 5 kPa, and **(c)**. 1 to 10 to 1 kPa are achieved via control knob turns with the calibration data in **Figure 3.5(a)**. Each pattern features three stages, each with 200 seconds under the real-time observation of the dynamic pressure response.

c) Dynamic pressure control using the control knob

Since the outlet pressure can be easily changed based on the calibrated position of the control knob, we demonstrate μPR's responsiveness to real-time pressure switching. Here we show that dynamic changes can be made to the ranges of pressure – low to high, medium to high, and low to medium. As shown in **Figure 3.8**, we measured dynamic pressure adjustments, each with three stages, that spanned the tested

range **(a)** 1 kPa - 5 kPa - 1 kPa, **(b)** 5 kPa - 10 kPa - 5 kPa, and **(c)** 1 kPa - 10 kPa - 1 kPa. In this experiment, we again used the calibration results as presented in **Figure 3.5(a)** for setpoints of the control knob positions for pressures used in this experiment. **Figure 3.8** shows that our µPR could ramp up and down to reach desired setpoints within one-minute periods, even among the largest dynamic pressure patterns in the experiment.

To highlight the integration of multiple µPRs in a single system, we utilized two µPRs to separately control the flow rates of two liquids within a Y-shaped microfluidic channel and visualized the dynamic equilibrium position of the two-stream laminar flow interface while adjusting one µPR to a new setpoint. We fed red-dyed deionized water to the top inlet port of the Y-channel with the pressure set to 1.0 kPa µPR, P1. Blue-dyed deionized water was fed into the bottom inlet port with pressure regulated by a second µPR, P2; these pressure values were changed during the experiment from a range of 1.0 kPa to 1.8 kPa.
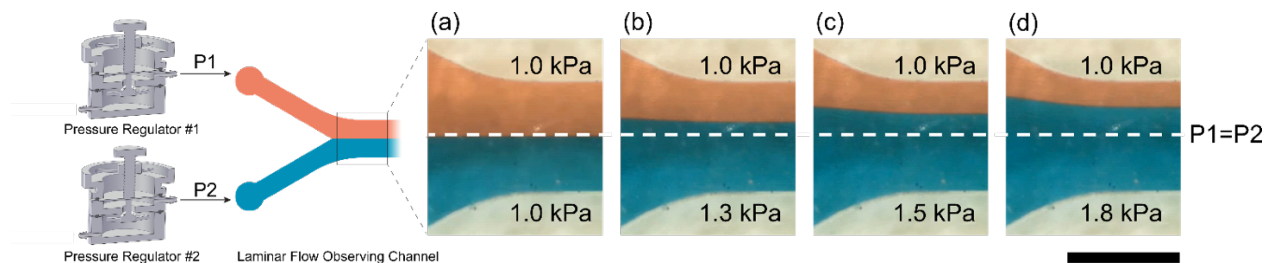
Figure 3.9: Real-time observation of co-laminar liquid flow pressurized with two µPRs. µPR #1 supplies pressure (P1) to one inlet port of the laminar flow observing channel, while µPR #2 supplies pressure (P2) to the other. P1 is set to 1 kPa as control, while P2 is adjusted to (a) 1.0 kPa, (b) 1.3 kPa, (c) 1.5 kPa, and (d) 1.8 kPa via the control knob. Scale bar = 1 mm

As expected, when P1 = P2, the liquid-liquid interface between the red and blue streams was located at the midline of the channel (white dashed line), indicating µPRs' capability of delivering stable flow rates using multiple µPRs. As we changed P2 from 1.0 kPa to 1.8 kPa by turning the control knob, the flow rate in the bottom channel increased and the interface was shifted upward (see **Figure 3.10**). 30 seconds of observation time were allowed for each new P2 set point with the following sequence of pressures: 1.0 kPa, 1.3 kPa, 1.0kPa, 1.5 kPa, 1.0 kPa, 1.8 kPa, and 1.0 kPa, for a total of 3 minutes and 30 seconds. The liquid-liquid interface shifted in response to the P2 pressure adjustment and quickly settled to the new position, and the

interface maintained stable during each of the 30-second pressure monitoring periods. The dynamic response of the μPR flow adjustment demonstrated real-time pressure adjustment and stable dynamic equilibrium positions. The pressure control capabilities of the system and flow profile possibilities were highlighted for more advanced real-time features that require pressure controls.

3.6 Conclusions

The goal of the platform is to provide a portable, simplified microfluidic flow control method while providing stable flows suitable for cell culture applications. While there are commercial solutions for pneumatic pressure control, these pressure regulators have larger footprints (>30mm), a higher outlet pressure range (~35 kPa) with a lower resolution (>3.5 kPa resolution). These approaches also cannot be customized, are expensive (>$100 USD), and require a dedicated laboratory compressed air line. By introducing the μPR along with a mini air pump to create a microfluidic flow control platform, a range of tunable and stable flow rates can be delivered within a portable system. This platform provides a cost-effective pressure control scheme with a range of customization opportunities owing to the increasing availability of hobby and commercial 3D printers. For reference, the total cost of the mini air pump and μPR setup as shown in this work is less than $7 USD, of which the μPR is less than $1.20 as shown below in **Table 3.2**

Item	Stock Number	Quantity	Unit price	Adjusted Price
Dental SG Resin	FLDGOR01	1.24 mL	$299/Liter	$0.37
Viton O-ring (001)	1284N101	1	$5.80/(25 pieces)	$0.23
Oil-resistant Buna-N O-ring	9262K442	2	$17.67/(100 pieces)	$0.35
M2 nut	91828A111	1	$6.14/(100 pieces)	$0.06
M2 bolt	91290A012	1	$16.58/(100 pieces)	$0.17
µPR total				**$1.18**
Mini air pump		1	$10.99/(2 pieces)	$5.50
Total				**$6.68**

Table 3.2 Bill of materials for the µPR and mini air pump set up

In our design, (see **Figure 3.2** and **Figure 3.3)**, the pressure regulating mechanism is similar to that of conventional pressure regulators. However, by incorporating 3D printing techniques, two sets of cantilever springs were integrated as an alternative to large commercial springs to simplify the assembly and help miniaturize the device. By incorporating cantilever springs into the poppet valve design, we created an upward closing force (F_C), as shown in **Figure 3.3**, to prevent possible high-pressure air leakage to the low-pressure chamber through the air passage. This "normally-closed" design allows users to shut off output pressure and momentarily disconnect the cell culture compartments for inspection or modification. Since regulation of P_{out} depends on the closing actions of the poppet valve, a gas-impermeable elastomeric Viton O-ring (shore 60A) was chosen at the poppet for better sealing. This suits our target applications, which are often operated with a low-pressure and flow rate regime. To target the range of 1-10 kPa, we chose the M2 size (0.4-mm pitch, 2-mm diameter) bolt as the control knob and partner it with a 24-position dial. Such a combination provides sufficient pressure resolution (< 1kPa per 15º turn) while retaining user-friendly control. By adjusting some key mechanical parameters, such as k_T and A_d we can achieve different targeted

outlet pressure ranges. **Equation 3.2** shows that k_T can be modified by changing the mechanical properties of the material by either switching to a different material or changing the curing settings of the 3D printer. k_T can also be altered by the geometry of cantilevers. For instance, we can increase the pressure sensitivity when we decrease k_T - which can be achieved by increasing the length of the cantilever springs or decreasing their width or thickness, as shown in **Equation 3.2**.

$$k_T = \frac{3Ebh^3}{4l^3}$$
 (Equation 3.2)

Where E is the Young's modulus of the 3D-printed material, and b, h, l are the width, thickness, and length of each cantilever, respectively.

Although k_T is more sensitive to changes in the thickness (h) of the cantilever than the width (b) (see **Equation 3.2**), the z accuracy (i.e., layer thickness control) of the 3D printer is often less than the x-y axes, resulting in greater variability in the thickness.[145] For example, a 0.1-mm thickness change (from 0.5 to 0.6 mm) of the cantilever springs can result in 70% increase in the spring constant. We anticipate that the 3D printed μPR can be modified to fit different pressure ranges based on the mathematical descriptions. For example, increasing the area of the sensing diaphragm A_d can improve the resolution of the output pressure setpoint but results in a larger device footprint and a smaller upper bound (constrained by maximum cantilever spring force) of the outlet pressure, since the outlet force scales linearly with the diaphragm area but is limited by the top cantilever spring force.

We fabricated our device by stacking 3D-printed components with an O-ring as a key sealing component to separate the high and low air pressure chambers. One may use multi-material 3D printer to print this device in one fabrication step with rigid and flexible parts for robust sealing, but these printers may not be accessible in all laboratories. For single-material printers, print-pause-print techniques may allow placements of soft materials for sealing during the fabrication, but it would add fabrication uncertainties, which defeat the purpose of creating an accessible and replicable platform. Since 3D-printed structures are still associated with dimensional errors for such small device features, we have to calibrate each device to determine the actual pressure control setpoints for usage as the mathematical equations serves only as a

design guideline. The relationship between control knob positions and outlet pressures, once calibrated, can be used to produce the desired outlet pressure. The compact and easy setup of the µPR-based microfluidic flow control platform provides manual control of ΔP based on the calibration. Since the flow control platform depends on the pressure drop to achieve the required flow rates, we implemented an open-end system (pressure at channel outlet = P_{atm}) to limit backpressure effects. During the cell culture experiment, we were able to deliver a constant flow rate of media to the culture platform to maintain a viable environment for HUVECs as compared to the no-flow situation. For more complicated microfluidic networks or closed-end systems, users may add back-pressure regulators to raise the downstream pressure threshold at the end of the microfluidic network to prevent potential backflows, however, this would require a higher range of driving pressures to deliver the same flow rates [146], [147].

With the dynamic control capability demonstrated with the co-laminar flows, we present more possibilities in dynamically controlling the outlet pressure to introduce different media flow rates for culture setup changes using our µPR (e.g., shear stress adjustment for cell alignment purposes) without modifying the channel geometry. In contrast to syringe pumps and commercial pneumatic solutions, the small footprint and minimal peripheral equipment requirements of the µPR-based system and be easily moved in and out of a cell culture incubator. Although this work is focused on creating an ease-of-use, tunable, and simple cell culture platform for single constant flow rates, automated flow control functionalities including pulsed or controlled ramp flows could be introduced using a stepper motor and gear train to program adjustments to the knob positions.

Chapter 4

Battery-less, two-stage pressure regulator flow control platform

4.1 Introduction

As demonstrated in **Chapter 3**, an accessible and portable system was capable of driving cell media flow into a microfluidic cell culture platform (m-μSiM) and successfully kept cells (HUVECs) alive to form a confluent monolayer. We propose a standalone, tunable, power-free continuous perfusion system for cell-based microfluidic devices. This system, based on the work shown in **Chapter 3**, would be designed to deliver flows in perfusion culture with two modes: (1) proliferation and (2) alignment of cells[53], [54], [55]. This power-free system can be easily transferrable between environments, e.g. from incubators to microscopes. This all-in-one design provides user-friendly operation of perfusion culture meanwhile ridding of the wiring complexities most current perfusion methods required (i.e. syringe pumps, microflow controllers, peristaltic pumps).

To address the need for a straightforward yet functional pumping platform that is portable, and power-free, we incorporate a 3D-printed miniature pressurized air tank/liquid reservoir as the high-pressure source. Despite the advantages of a pressurized air tank, the pressure decreases over time, impacting output stability. To maintain stable output pressure, we implement a two-stage pressure regulation mechanism. This two-stage micro pressure regulator (μPR) provides a tunable pressure differential (ΔP) across a stabilizing microchannel, controlling the flow rate in a downstream microfluidic network. 3D printing technology is used to create the pressure regulator, offering benefits such as customization, scalability, and rapid prototyping. The system's fully integrated design allows for easy transfer in and out of incubators for cell culture applications, facilitating periodic observations under optical microscopy.

The two-stage pressure regulator offers finer control over pressure adjustments compared to single-stage regulators. The non-tunable first stage, designed to screw onto the mini pressurized air tank's outlet, handles larger input pressures and provides a robust design. The first stage's outlet connects to the second stage's inlet via a 3D-printed flow control platform with integrated routing. This setup allows the regulator to manage higher input pressures and reduces the impact of supply pressure fluctuations. The sealed liquid reservoir with cell media is then introduced into a cell culture microchannel, enabling perfusion culture.

We anticipate that the dual-stage pressure regulator can reduce the higher pressure from the mini air tank/liquid reservoir (200 kPa gauge pressure) to a tunable range of 1-10 kPa gauge pressure, driving stable fluid flows. Preliminary experiments demonstrated success using microchannels with a cross-sectional area of 60 µm x 200 µm, achieving 16 dyne/cm^2 at 720 µL/hr fluid flow. To meet the designated flow rates (up to 720 µL/hr), the output pressure range of up to 10 kPa is designed to drive a fluidic stabilizing microchannel with dimensions of 60 µm x 200 µm x 7 cm. The maximum dispensed volume for 24 hours of pumping at 720 µL/hr is 16.6 mL. The two-stage regulator is expected to make significant contributions to microfluidics by addressing gaps in continuous flow driving and enabling cell culture applications. This platform offers a simple, portable, and customizable solution for precise flow control, making it accessible to research laboratories with 3D printing capabilities.

Although switching to a pressurized air tank enables a power-free design, the pressure in the tank decreased as a function of time and impacted the stability of the output pressure. To ensure that the output pressure doesn't drift off from its designated mode of perfusion culture due to this supply pressure effect, we introduce a dual-stage micro pressure regulator that operates in a similar fashion as the one shown in **Chapter 3**. As compared to the pressure regulator introduced in **Chapter 3**, we added a non-tunable 1st stage that's designed to be a screw-on to the outlet of the mini pressurized air tank. The resin-based diaphragm is designed to receive a larger input pressure. The outlet of the 1st stage is connected to the inlet of the 2nd stage, which features a similar setup to **Chapter 3**. With this two-stage design, the new pressure regulator not only receives a larger input pressure (required for long-term, power-free pumping) and also

suffers less from the supply pressure effect (due to the exhaust and a constrained volume of the pressurized mini air tank). At the downstream of the pressure regulator, we have a sealed liquid reservoir with cell media, which would be introduced into a cell culture microchannel, where perfusion culture happens.

	Chapter 3	Chapter 4
Power required	Yes	No
Compressed air source	Mini air compressor	Pressurized mini air tank
Pressure regulator type	Single-stage	Two-stage
Input pressure range	40-60 kPa	100-200 kPa
Output pressure range	1-10 kPa	0-10 kPa
Demonstrated flow rate range	10-100 nL/min	0-720μL/hr
Fluid stabilizing microchannel	20 μm x 100 μm x 32 cm	60 μm x 200 μm x 7 cm

Table 4.1 Comparison between the work in **Chapter 3** and **Chapter 4**.

4.2 Concept and theory

We look to create a stand-alone cell culture system that can be carried around. The continuous perfusion system would operate with two modes: (1) cell proliferation of HUVECs to form a confluent monolayer on the porous nanomembrane (2) alignment of HUVECs (coefficient of alignment > 0.5) after 24 hours of media flows. To fulfill the requirements, we need (1) a 3D-printed miniaturized pressurized air tank as the high-pressure source, (2) a two-stage pressure regulator for fine-tuning the flows, (3) a fluidic resistor microchannel to stabilize the flow, and (4) a microfluidic cell culture platform.

4.2.1 Design and Mechanism of a two-Stage μPR based flow driving platform

a) Design principles and pressure regulating mechanism

A two-stage pressure regulation allows reduced pressure fluctuations and lowers the supply pressure effect, in which the outlet pressure deviates from its designated value when the inlet pressure (air tank) lowers due to the exhaustion of flow driving. The pressure regulator follows similarly to the mechanism covered in **Chapter 3**.
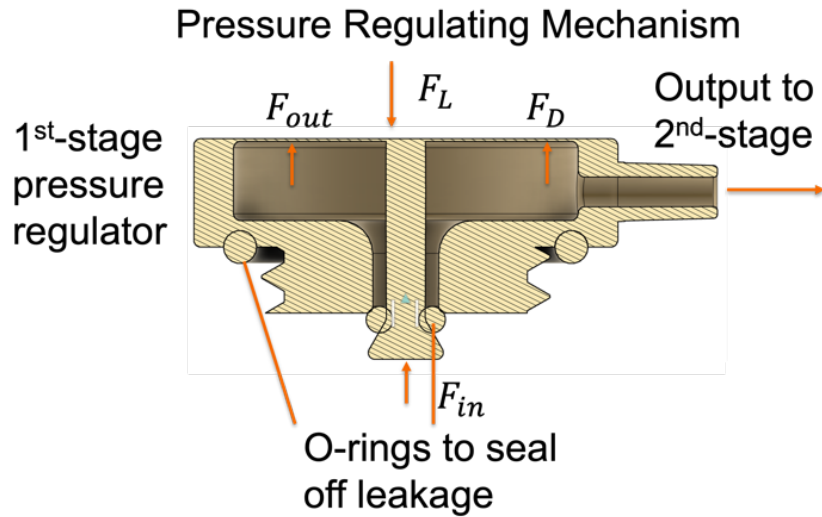
Pressure Regulating Mechanism

Figure 4.1: Depiction of the forces involved in the pressure regulating process. During Phase 1, the air passage is fully closed, while we supply air at a constant high pressure. In Phase 2, the adjustable load (F_L) on the diaphragm opens the air passage. As the diaphragm restoring force (F_D) increases, the air passage between the chambers remains closed. In Phase 3, when F_D surpasses a certain threshold, the air passage opens. Finally, in Phase 4, the pressure in the low-pressure air chamber will reach the desired level indicated by the control knob and the passage will close. Once the pressure is set by the user, the device toggles between Phase 3 and Phase 4 to maintain the desired output pressure.

Phase 1 (Resting phase)

Pressurized liquid is supplied via the air tank/liquid reservoir. There are two closing forces. The inlet pressure force (F_{in}) is an upward force generated by the inlet pressure acting on the poppet. The diaphragm has a restoring spring force (F_D) is an upward force generated by the displacement of the 3D-printed diaphragm. The displacement was due to the installment of the O-ring to the poppet as a valve. These upward forces press the poppet to the seat and close the air passage between chambers. Depends on the stages of the pressure regulator printed, the connecting rod length would vary, leading to different restoring spring forces.

Phase 2 (Loading phase)

As we adjust the load on applied on the diaphragm, F_L is no longer zero. This changes the restoring spring force (F_D), the restoring force ($F_D = k_D \cdot \Delta x_D$) on the sensing diaphragm would slightly increase. During this phase, the air passage is still sealed by upward forces (F_{in} and F_D).

Phase 3:

When we further incease the load, F_L overcomes the upward forces $(F_{in} + F_D)$ and pushes down the pressure-sensing diaphragm and the connecting rod. The motion of the connecting rod unseats the poppet valve and opens the air passage, allowing pressurized liquid to enter the outlet chamber. The pressure (P_{out}) in chamber exerts an upward force F_{out} on the bottom surface of the pressure-sensing diaphragm (area A_d), $P_{out} = F_{out} \cdot A_d^{-1}$.

Phase 4:

P_{out} increases until F_{out} and other upward forces F_{in}, F_D combine to match F_L as shown in **Equation 4.1**. These upward forces lift the poppet valve and block air flow between chambers. This allows us to set P_{out} by changing the force $(F_D = k_D \cdot \Delta x_D)$. Since P_{out} is used to pump liquid flow in a downstream primed microchannel, the exhaust due to pumping decreases P_{out} and triggers µPR to re-enter Phase 3 to allow pressurized liquid to compensate for the pressure loss. The µPR toggles between Phases 3 and 4 to maintain a stable P_{out}.

$$F_L = F_{out} + F_{in} + F_D \qquad \textbf{(Equation 4.1)}$$

The outlet pressure force, $F_{out} = P_{out} \cdot A_d$; P_{out} is the outlet pressure, and A_d is the area of the sensing diaphragm. F_{in} is the inlet pressure force on the exposed area of the poppet, while F_D is the diaphragm restoring force determined by the displacement of the diaphragm.

4.2.2 Supply pressure effect and dual-stage regulator design

Since we have a constrained supply of pressure sources, we need to factor in the system's supply pressure effect on the delivering pressure and driven flow in this system. This effect stems from the force-balance mechanism (**Equation 4.1**) as introduced above. P_{in}, thus F_{in}, decrease due to liquid dispensing over time, and F_{out} would have to increase to maintain the balance. An increased F_{out} scales linearly with P_{out} since the diaphragm area A_d remains constant. We calculate the supply pressure effect by the ratio of the poppet area exposed to the supply pressure and the pressure sensing diaphragm area exposed to the outlet pressure.

For instance, in the single-stage pressure regulator as introduced in our previous work, the theoretical supply

pressure effect is $\frac{(-)Area\ exposed\ to\ the\ supply\ pressure}{Area\ exposed\ to\ the\ outlet\ pressure}$ $= \frac{(-)1.5^2\pi}{4^2\pi}$ =(-)14%. This suggests that when the

supply pressure decreases by 100 kPa due to exhaust, the output rises by 14 kPa. For our targeted range of

output pressure (<10 kPa for this application), this would lead to catastrophic pressure/flow control stability.

Several solutions can be implemented to alleviate this effect. A straightforward way to lessen the supply

pressure effect is simply by increasing the diaphragm area exposed to the outlet pressure. Due to the

constraints in the system footprint, we decide to not adopt this solution. Other options include cascading

multiple stages or creating a "balanced" poppet design (the poppet area originally exposed to the supply

pressure is exposed to the outlet pressure chamber through a built-in air channel). Because of the

manufacturing difficulty of stereolithography parts in a miniature device, the complex air channel routing

and specific sealing requirements over moving pistons make the balanced poppet design a challenging task.

Thus, we decided to insert an extra stage to create a dual-stage pressure regulator. Cascading two stages

with identical supply pressure effects would result in a new effective supply pressure effect of

(-)14%×(-)14%, or ~2%.

4.3 Fabrication of the two-stage µPR based flow driving platform

4.3.1 Material selection

Component selection is based on factors like biocompatibility, chemical resistance, and mechanical

properties. We chose to 3D-print the structural components of the µPR, including the air tank/ liquid

reservoir, 1st stage regulator, 2nd stage regulator, and the entire flow platform, using the Form 2

stereolithography printer (Formlabs Inc., Somerville, MA, USA). We chose surgical guide resin (Formlabs

Inc., Somerville, MA, USA) as the building material due to its gas-impermeable characteristics and Class I

biocompatibility (EN-ISO 10993-1:2009/AC:2010). This would allow us to implement the device for cell

culture applications. We picked Viton fluoroelastomer O-rings (shore 60A) (McMaster Carr, Elmhurst, IL,

USA) as the surface-surface sealing material to prevent pressure leakage between thread interfaces of

chambers and air tank/ liquid reservoir. We encapsulate the devices with parylene-c coating (SCS Coating Systems, Indianapolis, IN, USA) to ensure the biocompatibility when the working fluids would be in contact with the components.

4.3.2 Fabrication process

The fabrication processes include the fabrication of the structural components of the flow driving system (airtank/ liquid reservoir, both stages of the pressure regulator), the flow stabilizing microchannel afterwards, and the nanoporous membrane-based cell culture platform.

a) Structural components of the platform: air tank, stages of the pressure regulator, routing system

We 3D-printed the air tank, two-stages of pressure regulator using the surgical guide resin. R-14 size O-rings are epoxy glued to the groove in the geometry of 1st and 2nd stages, enabling a leak-tight design with thread-on capabilities. The components would then be threaded on for application. Viton fluoroelastomer (shore 60A) O-rings were fitted over the connecting rod from the poppet valve of the 1st and 2nd stages. Natural rubber fittings were placed in the fluid routing connections built in the 3D-printed flow control platform to prevent liquid leakage. A rubber sport ball valve is fit into the opening of the air tank to ensure a refillable, leak-tight design.
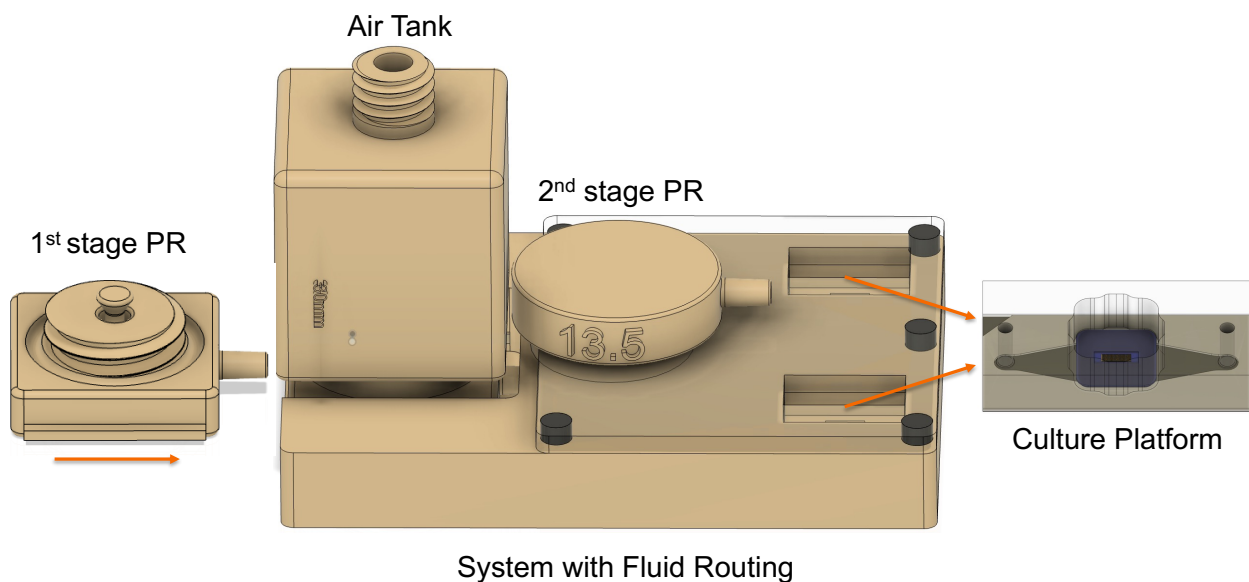

System with Fluid Routing

Figure 4.2 The two-stage pressure-regulator based flow driving platform. The system features 3D printed components: the air tank, 1ˢᵗ stage PR, 2ⁿᵈ stage PR, system with fluid routing. In the system, we have a designated downstream applications (a culture platform that features a nanoporous membrane.)

The system consists of an air tank/liquid reservoir design, a 1ˢᵗ stage pressure regulator, a 2ⁿᵈ stage pressure regulator. The flow after the 2ⁿᵈ stage pressure regulator would go downstream applications, such as the culture platform. We fit a sport ball refill valve to the opening of the air tank. Thread the 1ˢᵗ-stage PR with a commercially available balloon inside the air tank/liquid reservoir. The 1ˢᵗ stage PR is connected to a three-way valve. We then connect the outlet of the three-way valve into the fluidic routing platform and thread on the 2ⁿᵈ-stage PR onto the 3D-printed platform. The threaded reservoir/1ˢᵗ stage PR outlet with a three-way valve has one outlet connected to the system for input for the 2ⁿᵈ stage pressure regulator, and the other hanging as the refill port. The rails designed in the 1ˢᵗ stage PR allows us to easily slide into the fluid routing system and fixed in place.

b) Microfluidic flow-stabilizing channel

Microchannels were fabricated from polydimethylsiloxane (PDMS, Sylgard 184, Dow Inc., Midland, MI, USA) using standard soft-lithography techniques. A 4-inch silicon wafer was spin-coated with SU-8 2100 photoresist (Kayaku Advanced Materials, Westborough, MA, USA), soft-baked, and exposed to UV light through a transparency mask (CAD/Arts Services Inc., Bandon, OR, USA) to define the channel features. The wafer was then post-baked at 95°C, and the photoresist was developed (Kayaku Advanced Materials, Westborough, MA, USA). A PMMA sheet with rectangular openings (75 mm long, 25 mm wide) was attached to the wafer using a pressure-sensitive adhesive (PSA) to create a molding cavity with a defined height. The cavity was filled with degassed PDMS pre-polymer (mixed at a 10:1 base-to-catalyst ratio by mass) and cured on a hotplate at 80°C for 1 hour. After curing, the PDMS block was removed from the mold, and access ports were created using a 1-mm biopsy punch (World Precision Instruments, Sarasota, FL, USA).

c) Nanoporous membrane-based cell culture platform m-µSiM

Ultrathin nanoporous silicon nitride membranes, with a thickness of 100 nm, 15% porosity, and 60 nm pore sizes, were provided by SiMPore Inc. (Rochester, NY, USA). The overall dimensions of the membrane chip, including the silicon support, were 5.4 mm × 5.4 mm × 0.3 mm, featuring a permeable porous window measured at 2 mm × 0.7 mm × 0.1 μm. Components of the microfluidic-silicon membrane system (m-μSiM), such as the transparent cyclic olefin polymer (COP) base, pressure-sensitive adhesive (PSA) channel and support layers, and acrylic layers, were sourced from Aline Inc. (Pasadena, CA, USA). The membrane and m-μSiM components were assembled in a layer-by-layer fashion as shown in our companions' papers. The porous region of the membrane, distinguished by its yellow color, was encircled by a silicon support. This membrane divided the m-μSiM into luminal and abluminal compartments, facilitating the exchange of soluble factors between these compartments across length scales comparable to the approximately 100 nm thick basement membrane found in vivo.

The structural parts of m-μSiM has a core open-well as shown in **Figure 4.2**. This allows us to reconfigure the setup into a fluidic device by adding a flow module into its well. The flow module was fabricated using the standard soft lithography method with PDMS (Sylgard-184, Dow Inc., Midland, MI, USA)[141], [142]. SU-8 2100 (Kayaku Advanced Materials, Westborough, MA, USA) was spin-coated onto a 4" silicon wafer, soft-baked, and exposed to UV light through a transparency mask (CAD/Arts Services Inc., Bandon, OR, USA) to define the channel featuring a rectangular groove with dimensions 60 μm x 200 μm x 5 mm. We post-baked the wafer at 95ºC. The photoresist was then developed (Kayaku Advanced Materials, Westborough, MA, USA). A PMMA sheet with rectangular openings attached to the mold via pressure sensitive adhesive. The mold was then filled with degassed PDMS pre-polymer (10:1 base to catalyst ratio by mass) and cured on a hotplate for 1 hour at 80°C. We removed the PDMS flow modules from the mold and access ports were cored with a 1-mm biopsy punch (World Precision Instruments, Sarasota, FL, USA). The PDMS flow modules were ozone-treated to form a permanent bond with the nanoporous membrane.

4.4 Flow rate control via the dual-stage pressure regulator

4.4.1 Setting up the flow control platform

This step follows the assembly of the system, which includes the air tank with a refill valve, both pressure regulating stages, fluid routing platform. We use a luer lock to 1/8 in' connector to connect fluid lines to the stabilizing microfluidic resistor. The outlet of the microfluidic resistor is connected to a flow sensor (LG-16, Sensirion AG, Stäfa, Switzerland)

We use a 5-mL syringe with an 18G syringe tip to pressurize the air tank/liquid reservoir design. 25 mL of liquid is first filled into the liquid reservoir. Refilling of the liquid reservoir is performed via a three-way valve with luer lock ends. By repeatedly filling in with 5-ml syringe for five times, the amount of fluid can be accurately controlled and filled in the balloon reservoir present in the air tank/reservoir setup. Pressurizing and re-pressurizing of the air tank/liquid reservoir can be performed after the liquid reaches the capacity with the following process. (1) Insert an 18G syringe tip to the refill valve to vent remaining pneumatic pressure inside the air tank (2) Connect a 5-mL syringe with its barrel at the 5-mL mark and presses the barrel until the end of the syringe and pull the syringe out of the three-way valve (3) Repeat step 2 for five times (4) Connect a 5-mL syringe to the hanging 18G syringe tip at the refill valve and press the barrel until the end. (5) Pull out the syringe with tip at the refill valve and repeat step 4.

4.4.2 Leakage test

The 3D-printed pressurized air tank is filled with 200 kPa gauge pressure from air supplied with the Dwyer-110 pressure gauge and a ControlAir Type-90 pressure regulator. Pressure is filled into the air tank via the sport valve, as introduced in the fabrication process, using a syringe tip (size 18G). The air tank's outlet is then connected to a pressure calibrator suitable for pressures (Fluke-717, Fluke, Everett, Washington, USA). The pressure in the air tank is monitored over 72 hours for leakage observation.

4.4.3 Flow rate measurement

The general pressure/flow experimental setup features the pressure regulator and the PDMS stabilizing microchannel (60-μm height, 200-μm width, and 7-cm length). We supply pressure to the 1st stage pressure regulator with a compressed air chamber with 200 kPa gauge pressure. The outlet of the 1st stage regulator

is connected to supply the inlet of the 2nd-stage pressure regulator. The outlet of the 2nd stage was then connected to the inlet of the PDMS microfluidic channel and the outlet of the channel further connected to a flow sensor (LG-16, Sensirion AG., Stäfa, Switzerland). Tygon microtubings (2-mm ID, 5-cm length) were used to connect these components.

4.4.4. Verification of required flow rates to deliver both modes

To ensure the flow rates delivered to the culture platform can provide the two modes of perfusion, we deliver 60 and 600 µl/hr using a syringe pump to PDMS microchannels with dimensions of 60 µm x 200 µm x 5 mm. We would perform LIVE/DEAD stain (Thermo Fisher Scientific, Waltham, MA, USA) to assess cell viabilit. Labeled cells were imaged using an Olympus IX-81 fluorescence microscope with CellSens software (Olympus, Tokyo, Japan) with constant image capture settings across the experimental sets.

4.5 Results and takeaways

<u>a) Fabrication and leakage test</u>

The device is fabricated via the fabrication step as mentioned in the fabrication process. The system assembly can be described in two steps as shown below in Figure 4.3 and Figure 4.4.

The first part of the fabrication included parylene-c coating of all 3D-printed components. This step is performed using SCS coating (SCS Coating Systems, Indianapolis, IN, USA) with 1 gram of parylene dimer with vapor pressure of 30 mTorr.
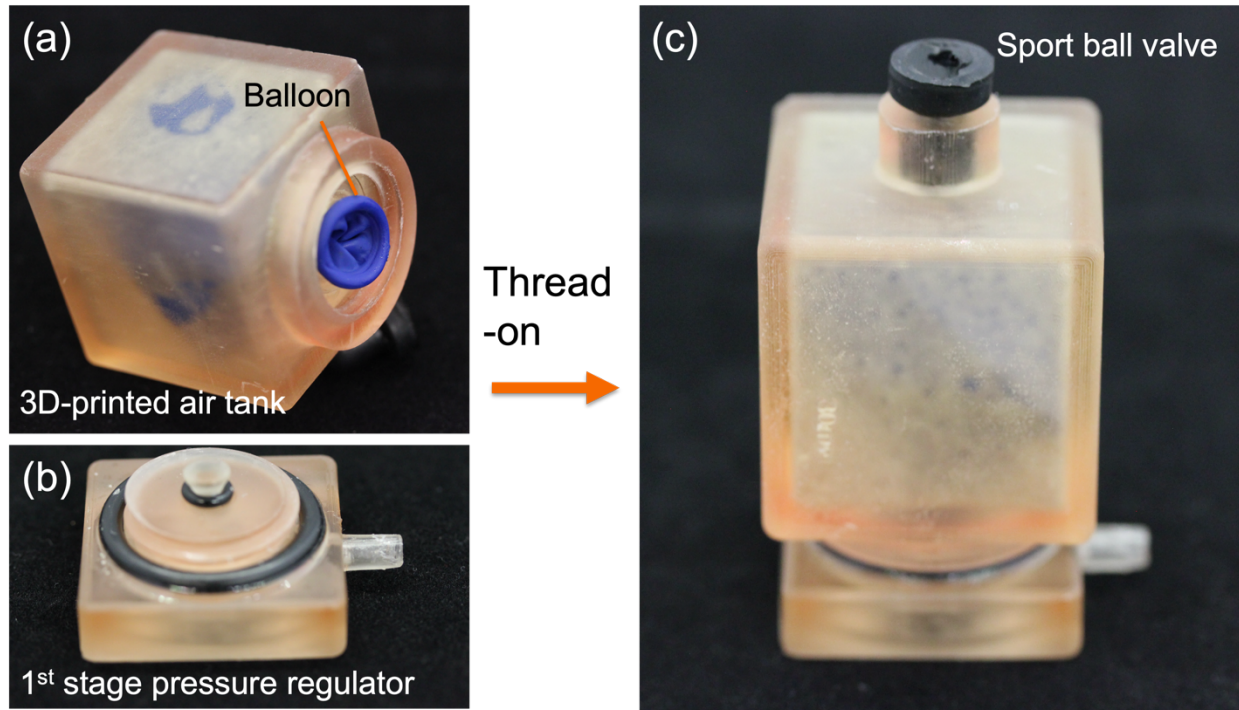
Figure 4.3 The first part of the fabrication process. (a) The 3D-printed air tank with a commercially available balloon. (b) The 1ˢᵗ stage pressure-regulator is has a R1 size natural rubber O-ring as the poppet valve sealing component. A R14 O-ring is fit in the groove for sealing the air tank/ media reservoir. (c) The first part of the system is fabricated by threading the 1ˢᵗ stage pressure regulator to the air tank with the balloon's outlet connected to the poppet valve. A sport ball valve is fit to the design of the 3D printed air tank to enable a refillable design.

A commercial balloon is fit into the 3D printed air tank with its outlet facing outwards. A R-1 size O-ring is fit into the poppet valve of the 1ˢᵗ stage pressure regulator. A R-14 O-ring is epoxy glued to the groove designed in the 1ˢᵗ stage pressure regulator for sealing purposes. The 1ˢᵗ stage pressure regulator is threaded onto the 3D-printed air tank with the balloon's outlet covering the poppet valve. A sport ball valve is fit into the refill port of the 3D-printed air tank for venting and pressurizing.

The leakage test of the air tank would be performed in a setting similar to this step, but without the R-1 poppet valve O-ring and the balloon. The outlet of the pressure regulator is connected to a pressure calibrator (Fluke-717, Fluke, Everett, Washington, USA). The pressure was first supplied to the air tank via the sport valve using a 18G syringe tip. The supplied pressure was controlled to be 200 kPa, using ControlAir Type-90 pressure regulator along with the Dwyer-110 pressure gauge and the confirmation of

the pressure calibrator. The syringe tip was pulled out after pressurizing. After 24 and 72 hours, the readings were recorded. We performed the test on three different air tanks for three times, the recorded air tank pressure was 197.1±1.2 kPa at 24-hr mark and 192.3±4.0 kPa at 72 hr mark. This suggested minimal pressure loss for the sealed air tank.
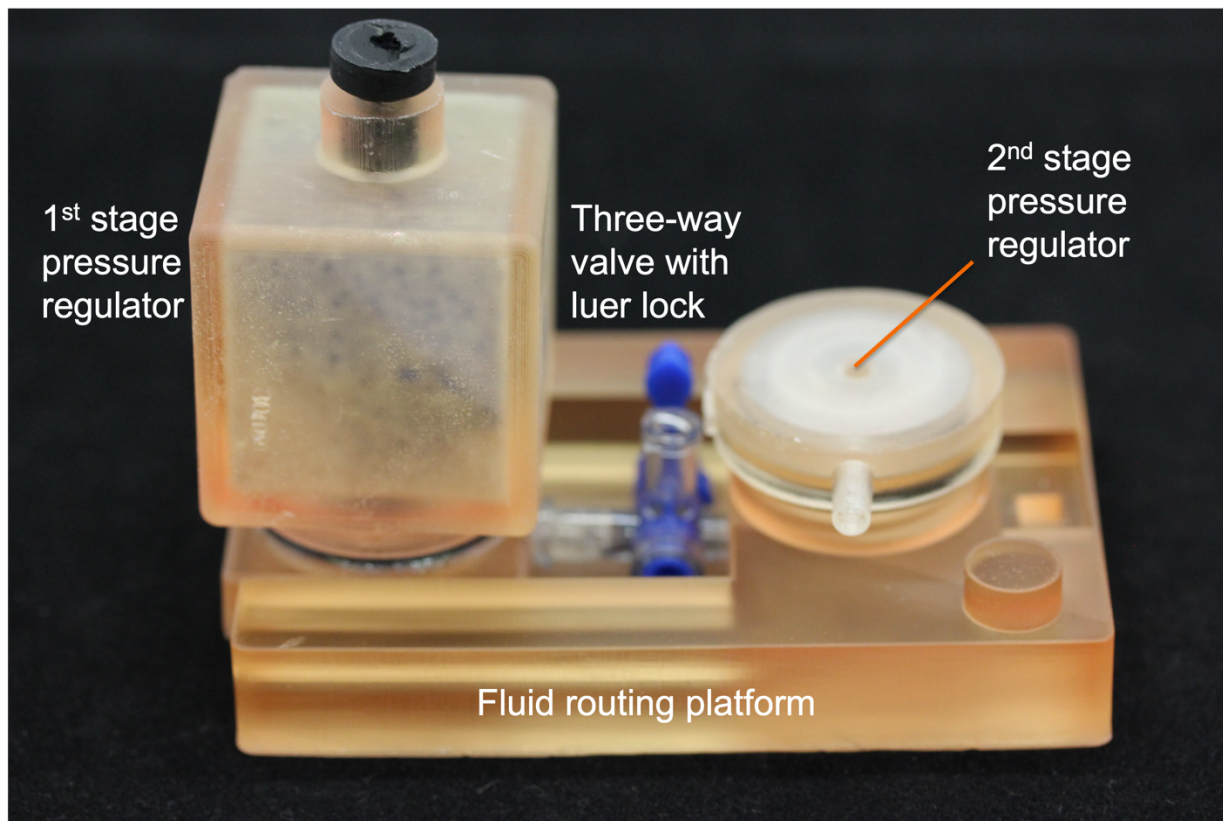
Figure 4.4 The second part of the fabrication process. After the 1st stage pressure-regulator is completed, a three-way valve with two luer lock female ends, and a luer male end is connected. The outlet of the 1st stage pressure regulator is fit to one luer female. The other luer female is hanging for refill uses via syringes. The luer male is fit to the fluid routing platform as the supplied pressurized source for the 2nd stage pressure regulator. The 2nd stage pressure regulator is threaded onto the fluid routing platform. The outlet of the 2nd stage pressure regulator can be connected to desired fluidic stabilizing resistance to users' desire.

The second part of the fabrication included fitting the 1st stage pressure regulator's outlet to a leur female end of a three-way valve. The other luer female is placed to be hanging vertically. This allows users to refill working liquid into the balloon reservoir. The luer male end of the three-way valve is connected to the fluid routing platform as the inlet for the 2nd stage pressure regulator. The 2nd stage pressure regulator followed

a similar threading process onto the fluid routing platform. The outlet of the 2nd stage pressure regulator is connected to a PDMS resistor/ or a coil of microtubing to the users' preference.

b) Power-free pumping cycles of 24 hours

To realize a true stand-alone, power-free platform, we implemented an air tank/ liquid reservoir design that incorporates a leak-free refill port and an outlet connected to the 1st stage of the regulator. Since the system has a constrained pressure source during one pumping cycle, we seek to limit the total dispensed volume of media by the end of a pumping cycle to avoid significant pressure decrease (which may result in undesired flow rate drifts). This requires us to culture cells with smaller flow rates and thus smaller culture channel dimensions.

c) Supply pressure effect and dual-stage regulating

Since we have a constrained supply of pressure sources, we need to factor in the system's supply pressure effect on the delivering pressure and driven flow in this system. This effect stems from the force-balance mechanism. P_{in}, thus F_{in}, decrease due to liquid pumping over time, and F_{out} increases to maintain the balance. An increased F_{out} directly results in an increased P_{out} as the diaphragm area A_d remains constant ($F_{out} = P_{out} \cdot A_d$). The supply pressure effect can be calculated by the ratio of the poppet area exposed to the supply pressure and the pressure sensing diaphragm area exposed to the outlet pressure.

For instance, in the single-stage pressure regulator, the theoretical supply pressure effect is $\frac{(-)Area\ exposed\ to\ the\ supply\ pressure}{Area\ exposed\ to\ the\ outlet\ pressure} = \frac{(-)1.5^2\pi}{4^2\pi} = (-)14\%$. This suggests that when the supply pressure drops by 100 kPa due to exhaust, the output rises by 14 kPa. For our targeted range of output pressure (<10 kPa for this application), this would lead to catastrophic pressure/flow control stability.

Several solutions can be implemented to alleviate this effect. One straightforward way to lessen the supply pressure effect is simply by increasing the diaphragm area exposed to the outlet pressure. Due to the constraints in the system footprint, we decide to not adopt this solution. Other options include cascading multiple stages or creating a "balanced" poppet design (the poppet area originally exposed to the supply pressure is exposed to the outlet pressure chamber through a built-in air channel). Because of the

manufacturing difficulty of using stereolithography parts in a miniature device, the complex air channel routing and specific sealing requirements over moving pistons make the balanced poppet design a difficult task. Thus, we decided to insert an extra stage to create a dual-stage pressure regulator. Cascading two stages with identical supply pressure effects would results in a new effective supply pressure effect of (-)14%×(-)14%, or ~2%.

The dual-stage pressure regulator uses the force-balance mechanism to reduce the higher pressure to a lower controllable range of pressures. The 1st stage needs to be capable of receiving a much higher pressure (200 kPa) to be sufficient to drive liquid flows for 24 hours. Moreover, we need a normally open design for the 1st stage to guarantee a stable pressure supply for the 2nd stage. Thus, we introduce a different design in the 1st stage. We remove the cantilever springs in the inlet pressure chamber to make the device normally open. Furthermore, instead of using polyimide the pressure sensing diaphragm material, we 3D-printed the diaphragm, the connecting rod, and the poppet altogether with the outlet pressure chamber. To ensure the poppet valve can provide necessary sealing during operation, we fit an O-ring to fit between the poppet valve and the air channel of the outlet chamber. We look to optimize the fabrication process for the 2nd stage of the pressure regulator by replacing the commercial bolt/nut pair with 3D-printed threads. Moreover, we add a boss plate with a stainless-steel ball bearing to ensure that the pressure tuning process stays smooth.

d) Air tank/ liquid reservoir validation

In this section, we investigate the supply pressure effect on the stability of the flow delivering pressure to layout the design requirements of the air tank.

The supply pressure effect on the fluidic driving pressure can be summarized as the following equation.

$$P_d(t) = P_d(0) + SPE * \Delta P_{tank}$$ (**Equation 4.2**)

Where $P_d(t)$ is the driving pressure at time t, $P_d(0)$ refers to the initial driving pressure set by the user, SPE is the supply pressure effect, and $\Delta P_{tank} = (P_{tank}(t) - P_{tank}(0))$, is the difference in the pressure of the pressurized air tank over the pumping period t.

The total dispensed volume of cell media (V_d) is represented as the integration of real-time liquid flow rate $Q(\tau)$ over the pumping period t. The liquid flow rate by a differential pressure over a set fluidic resistance can be described as a hydraulic analogy of Ohm's law, $Q(\tau) = P_d(\tau) \cdot R^{-1}$, where R is the resistance of the stabilizing microfluidic resistor, where we assume its fluidic resistance stays constant throughout the period. The relationship between dispensed cell media volume and fluidic driving pressure can be interpreted as follows.

$$V_d(t) = \int_0^t Q(\tau)\, d\tau = \int_0^t P_d(\tau) \cdot R^{-1}\, d\tau = \frac{1}{R} \int_0^t P_d(\tau)\, d\tau \qquad \textbf{(Equation 4.3)}$$

Since the highest pressure present in our system is 200 kPa gauge pressure and the air remains sealed in the liquid reservoir, we implement Boyle's law (pressure*volume = constant) to represent the states of the pneumatic pressures involved in this system.

In this section, we assume:

1. The system includes the pressurized air tank, the air passage between the regulator and the liquid reservoir, and the liquid in the microchannels.

2. All dispensed liquid is collected in an open container exposed to atmospheric pressure.

3. Boyle's law stands in the air line and the liquid reservoir during the pumping period from $\tau = 0$ to $\tau = t$

4. Negligible initial dead volume for pneumatic pressure in the system.

5. The incubator provides a constant temperature environment for the system.

At $\tau = 0$ At $\tau = t$

$$P_{tank}(0) * V_{tank} + P_d(0) * V_d(0) \qquad\qquad P_{tank}(t) * V_{tank} + P_d(t) * V_d(t)$$

$$P_{tank}(0) * V_{tank} \qquad\qquad P_{tank}(t) * V_{tank} + P_d(t) * V_d(t)$$

$$\Rightarrow \quad \left(P_{tank}(0) - P_{tank}(t)\right) * V_{tank} = P_d(t) * V_d(t)$$

$$\Rightarrow \quad -\Delta P_{tank} * V_{tank} = P_d(t) * V_d(t) \qquad\qquad \textbf{(Equation 4.4)}$$

When we combine **Equation 4.2** and **Equation 4.4**, we get

$$\Rightarrow \quad -\Delta P_{tank} * V_{tank} = (P_d(0) + SPE * \Delta P_{tank}) * V_d(t)$$

$$\Rightarrow \quad -\Delta P_{tank} * \left(V_{tank} + SPE * V_d(t)\right) = P_d(0) * V_d(t) \qquad \textbf{(Equation 4.5)}$$

For this dual-stage pressure regulator, the theoretical supply pressure effect is (+)2%, which indicates a descending output pressure when the supply pressure to the regulator drops. To ensure the supply pressure effect wouldn't cause the fluidic driving pressures to drop out of the desired ranges, we start the culture with fluid flow rates for both modes at their higher bounds of pressure ranges mode 2 at 10 kPa.

Here we investigate the flow rate and pressure requirements for different modes on the air tank volume.

Mode 1: Keep the device in perfusion over 24 hours

The minimum flow rate required to be delivered to device can be calculated via the equations covered in Young's work (Young 2010). ECT, or the effective culture time is linearly related to the height of the media level h. Typically, for a 1.2 mm height of media results in 48 hours of effective culture time in culture flasks. By scaling, this indicates the cell media in our culture channel (height of 50 µm) would provide a 2 hours of effective culture time; suggesting that we should pump 12 full exchanges of cell culture media in the channel per day. The total volume of the microchannel including the cored ports is 5 µL. This means the minimum flow rate has to be 60 µL/day, or 2.5 µL/hour or 42 nL/min.

Mode 2: Keep the wall shear stress at the cell culture channel between 5.5-16 dynes/cm^2

The maximum dispensed volume over 24 hours at mode 2 would be pumping at 720 µl/hr at P_d = 10 kPa for our system, or a total dispensed volume ($V_d(24\ h)$) of 16.6 mL.

For design purposes, we substitute $V_d(t)$ with a maximum dispensed volume of 16.6 mL, and the driving pressure at designated fluidic driving pressure $P_d(0)$ = 10 kPa. To stay in mode 2, $P_d(24\ h)$ should not fall under 4 kPa. Since the supply pressure effect constant of the dual-stage system is 2%, the system stays in mode 2 as long as the tank pressure difference (ΔP_{tank}) over 24 hours remains under ($\frac{(P_d(24\ hours)-P_d(0))}{SPE}$) or (-)1.5 kPa/2% = (-)75 kPa. For a fail-safe design, we use $P_d(0)$ for the largest V_{tank}.

We target the system to create two shear stress ranges of cell media flow in a cell culture microchannel - one for proliferation and the other for alignment of cells. In this design, we look to demonstrate this capability using HUVECs and the m-µSiM platform covered in **Chapter 3**. The two modes of flow rates (1) sufficient flow for perfusion at minimum of 42 nL/min and (2) 5.5-16 dynes/cm^2 shear stress range mentioned in the literature to successfully form confluent cell monolayer and alignment of HUVECs after 24 hours of cell media flow, respectively (DeStefano 2017, Sinha 2016). The newly designed culture channel featured dimensions of 50-µm height, 200-µm width, and 5-mm length. With these channel dimensions, we would drive flow rates from 165 up to 720 µL/hr to deliver 5.5-16 dyne/ cm^2 shear stress range for mode 2.
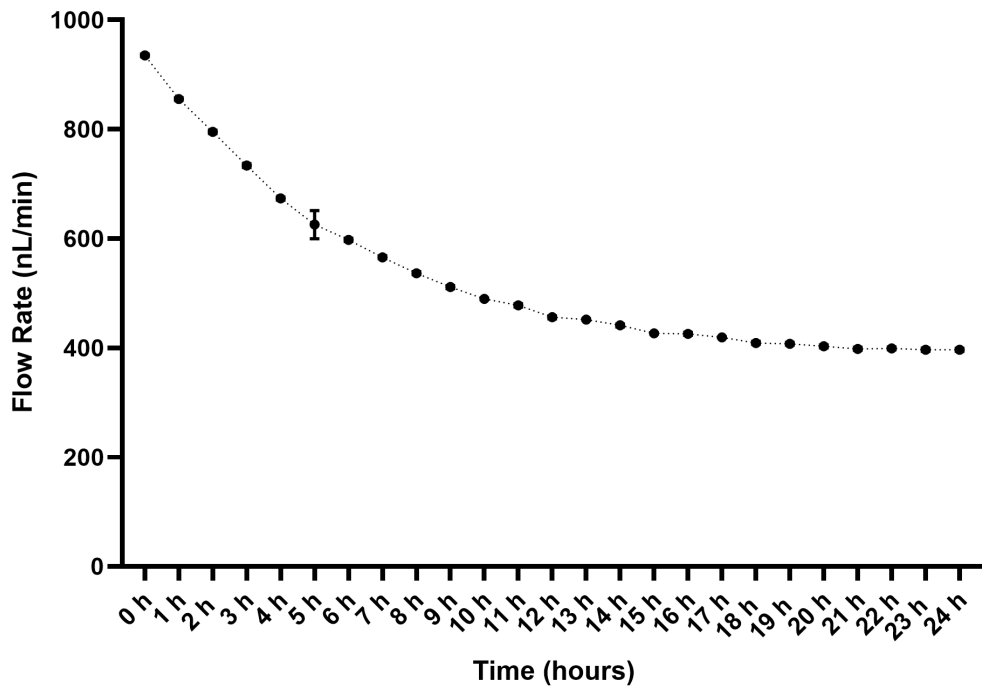
Figure 4.5 Mode 1 flow delivery: device flow rate started from 930 nL/min (or 1.29 dynes/cm^2 wall shear stress) at 0-hr mark and ended at 400 nL/min (0.56 dynes/cm^2 wall shear stress) at 24-hr mark.

As shown above in **Figure 4.5**, we were able to keep the flow above from 930 down to 400 nL/min for the entire 24 hours of delivery. This flow rate is sufficient to keep the cell growth while preventing the cells from experiencing shear stress range that might causes cell alignment.

The device successfully delivered the flow range we are interested in over the 24-hour period, a typical span where researchers observe the cell microenvironments.

Time (hr)	Driving Pressure (kPa)	Flow rate (μL/hr)
0	10	693.3±16.0
0.25	9.8	678.1±15.1
0.5	9.6	666.8±18.5
1	9.4	652.5±20.3
24	3.2	222.4±15.5

Table 4.2 Mode 2 delivery of the flow rate measured results in 693.3 μL/hr, which slowly decays to 222.4 μL/hr after 24 hours of pumping. This indicated the device could deliver shear stress from 7.4-23.1 dynes/cm^2 at the microchannel.

In mode 2 of pumping, the system can deliver shear stress from 7.4-23.1 dynes/cm^2, fulfilling the requirement of shear stress level from 5.5-16 dynes/cm^2. The system can be refilled and re-pressurized with ease; this allows users to deliver desired flow rates without further increasing the pressure level or air tank volume of the system.

4.6 Conclusion

By introducing a two-stage µPR with a built-in, refillable air tank that also works as a liquid reservoir, we have developed a microfluidic flow control platform that delivers a range of tunable and stable flow rates within a portable system size. Our platform offers an accessible, stable, and power-free pressure control scheme with customization opportunities, thanks to the increasing availability of hobbyist and commercial 3D printers.

In this system, the µPR is in direct contact with the working liquid. The inclusion of a built-in, refillable air tank that also serves as a liquid reservoir adds to the portability and convenience of our platform, eliminating the need for an external compressed air line. This air tank allows for continuous and stable flow rates over extended periods, and its refillable nature ensures that the system can be easily maintained and adapted to various experimental needs.

Ease of use is a significant advantage of our platform. 3D-printed structures are prone to dimensional errors, especially for small device features, making the calibration of the µPR's outlet pressure device-specific. Once calibrated, the relationship between control knob positions and outlet pressures can be used to achieve the desired outlet pressure. The µPR's direct contact with the fluid allows for seamless integration into cell culture systems. The compact and easy setup of the µPR-based microfluidic flow control platform provides manual control of ΔP based on calibration. Since the flow control platform relies on the pressure drop to drive the required flow rates, backpressure regulators may be added to the end of the microfluidic network for applications with potential backflow issues. For additional functionalities, we can automate the knob

control process by incorporating stepper motors, unlocking advanced functions such as pulsed and controlled ramp flows.

Our μPR-based system is designed with user-friendliness in mind, particularly focusing on the ease of refilling and transferring the device in and out of a cell culture incubator. This feature makes it easy to periodically observe cultures under optical microscopy without significant disruption. In this work, we were able to maintain a constant flow rate of media to a culture platform, creating a viable environment for HUVECs compared to a no-flow situation. Unlike syringe pumps and commercial pneumatic solutions, the small footprint, built-in air tank, and minimal peripheral equipment requirements of the μPR-based system allow it to be easily moved in and out of a cell culture incubator. This ease of use makes it an attractive option for researchers looking for reliable and flexible microfluidic flow control, with the added benefit of straightforward maintenance and adaptability.

Chapter 5

Contribution and Future Directions for the All-in-One Stand-Alone Microfluidic Cell Culture Platform

5.1 Introduction and Major Contribution of this Thesis

The introduced microfluidic cell culture flow control system allows us to demonstrate continuous cell media delivery to the cellular microenvironment. The devices are compact and portable, making them easy to transfer in and out of the incubator to periodically observe under optical microscope. Moreover, the devices do not require excess electric wiring or pneumatic compressed air lines that need to be connected through the incubators. The system introduced in this thesis enable an accessible device, ready for collaboration with different laboratories and researchers. The system featured an easy-to-fabricate microvalve, and a pumping system consisted of 3D-printed components via a widely deployed commercial SLA 3D printed. This enables the accessibility of the system, allowing users from different labs to conveniently fabricate, assemble, and customize their design. Despite the great advantages of this all-in-one, stand-alone microfluidic cell culture platform, there is still room for further work and improvement. Here, we explore several potential improvements via the following categories to enhance the functionality, precision, and efficiency of battery-less, stand-alone microfluidic cell culture platforms.

5.2 Increase the pumping period for high shear environment

The battery-less system was capable of continuous delivery of cell media to the designated cell culture microenvironment. The refillable pressurized air tank is the key driving source of the fluid flow delivery. However, due to the exhaust of the air during the pumping process, the pressurized air tank inevitably encounters pressure drop when we set the device in long term cell culture applications. A few design optimizations may be incorporated to solve this issue. For instance, since current system consists of 3D-

printed components with SLA process, we printed the diaphragms larger to ensure the pressure regulating ratio match our expectation. Moreover, we reserved extra tolerance during device printing to prevent undesired geometrical failures, such as clogged airways or smaller diaphragm area than expected. This conservative approach of fabrication enables a higher yield rate in the expense of dead volumes in different components. These dead volumes require us to prime the devices with some care prior to use and contribute to the faster exhaust in the pressure drop, thus flow rate decay.

To further minimize the supply pressure effect from the pressurized air tank, an extra stage of the pressure regulator can be modularly connected. The current setup allowed us to cascade multiple pressure regulating stages to the system. Although the response time of multi-stage pressure regulators increase accordingly to the number of stages, we prefer to deliver a stable and continuous flow to the downstream applications over the real-time pressure adjustment capability shown in Chapter 3.

Another design modification that we may incorporate is to increase the supply pressure in the pressurized air tank. With a higher supply pressure, the stand-alone system would be able to deliver a larger flow rate for long-term cell culture without repressurizing the air tank. To realize this design change, we can look toward a different material for the air tank and the first stage pressure regulator. For instance, additive manufacturing featuring titanium via selective laser melting process has been used to create pressure vessels that can withstand 1.03 MPa [148].

5.3 Minimize manual intervention

One way to minimize manual intervention is to realize the aforementioned improvement – prolonging the pumping period without refilling/ repressurizing the air tank. A pre-pressurized liquid cartridge with a one-time valve design can also enhance the refill process. This allows users to conveniently discard and restart pumping without refilling via a syringe and a corresponding tip. This reduces the need for manual intervention, minimizes the risk of human error, and ensures consistent experimental conditions.

5.4 Scalability and Modular Design

We have been working on the device to make them modular and scalable, however there is still room for improvements. Currently, our modular components are 3D-printed with specific interconnect designs. We would investigate the possibility of incorporating commercial interconnects with more universal specifications. Furthermore, maintaining flexibility of the interconnects enable an easier routing of the downstream microfluidic network via plug-and-play of multi-way connectors/ splitters, rather than developing a design-specific microfluidic network with complicated channel routings. By keeping the design specifications aligned with commercially available products, the system can be easily replaced or upgraded, allowing researchers to focus on customizing the biomedical aspects of the platform for specific applications. Scalability ensures that the platform can accommodate different cell types and culture conditions, making it a valuable tool for a wide range of biological and biomedical studies.

5.5 Microfluidic network at downstream

Enhancing the design of the microfluidic channel networks and components can improve the efficiency and functionality of the platform. By optimizing the geometry and carefully investigate the flow routing, we can design a more complex downstream microchannel network that feature multiple cell culture microenvironments [149]. Such systems, referred as multi-organ-on-chips, provide a framework investigate how one microenvironment would interact to another (or more) [150], [151], [152]. Organs-on-chips (OoCs) are systems that contain miniature tissues or cell layers grown inside microfluidic chips. Combining advances in tissue engineering and microfabrication, OoCs have gained interest as a next-generation experimental platform to investigate human pathophysiology and the effect of therapeutics in the body. These systems are developed to study human physiology with specific controlled microenvironments, such as blood-tendon-on-chip[153], lung-on-chip [154], kidney-on-chip[155], and blood-brain-barrier-on-chip[156], [157], [158], [159], [160]. Tissues or cell layers grown in the chips later investigated on their reaction to different stimuli, such as inflammatory factors. To better mimic human physiology, the chips

are designed to control cell microenvironments and maintain tissue-specific functions. This accessible microfluidic cell culture platform with expansion capabilities would be beneficial for the field.

5.6 Conclusion

In conclusion, several improvements can be made to battery-less, stand-alone microfluidic cell culture platforms to enhance their functionality, efficiency, and usability. Using a less dead volume design, increasing the initial pumping pressure, optimizing the scalable/ modular microfluidic design, and incorporating a more complicated microfluidic network are key strategies to achieve these goals. These advancements will not only extend the operational lifespan of the platforms but also broaden their applications in various research fields, ultimately contributing to significant advancements in cell culture technology.

Reference

[1]   K. W. Oh and C. H. Ahn, "A review of microvalves," *Journal of Micromechanics and Microengineering*, vol. 16, no. 5, pp. R13–R39, May 2006, doi: 10.1088/0960-1317/16/5/R01.

[2]   G. M. Whitesides, "The origins and the future of microfluidics," Jul. 27, 2006. doi: 10.1038/nature05058.

[3]   Y. N. Wang and L. M. Fu, "Micropumps and biomedical applications – A review," *Microelectron Eng*, vol. 195, no. April, pp. 121–138, 2018, doi: 10.1016/j.mee.2018.04.008.

[4]   M. Mehling and S. Tay, "Microfluidic cell culture," 2014, *Elsevier Ltd*. doi: 10.1016/j.copbio.2013.10.005.

[5]   A. L. Paguirigan and D. J. Beebe, "Microfluidics meet cell biology: Bridging the gap by validation and application of microscale techniques for cell biological assays," *BioEssays*, vol. 30, no. 9, pp. 811–821, Sep. 2008, doi: 10.1002/bies.20804.

[6]   N. Mavrogiannis, M. Ibo, X. Fu, F. Crivellari, and Z. Gagnon, "Microfluidics made easy: A robust low-cost constant pressure flow controller for engineers and cell biologists," *Biomicrofluidics*, vol. 10, no. 3, May 2016, doi: 10.1063/1.4950753.

[7]   J. Y. Qian, C. W. Hou, X. J. Li, and Z. J. Jin, *Actuation mechanism of microvalves: A review*, vol. 11, no. 2. 2020. doi: 10.3390/mi11020172.

[8]   K. W. Oh and C. H. Ahn, "A review of microvalves," *Journal of Micromechanics and Microengineering*, vol. 16, no. 5, pp. R13–R39, May 2006, doi: 10.1088/0960-1317/16/5/R01.

[9]   P. J. Chen, D. C. Rodger, M. S. Humayun, and Y. C. Tai, "Floating-disk parylene microvalves for self-pressure-regulating flow controls," *Journal of Microelectromechanical Systems*, vol. 17, no. 6, pp. 1352–1361, 2008, doi: 10.1109/JMEMS.2008.2004947.

[10]   A. Debray, T. Nakakubo, K. Ueda, S. Mogi, M. Shibata, and H. Fujita, "A passive micro gas regulator for hydrogen flow control," *Journal of Micromechanics and Microengineering*, vol. 15, no. 9, Sep. 2005, doi: 10.1088/0960-1317/15/9/S05.

[11]   E. Chappel, D. Dumont-Fillon, and S. Mefti, "Passive flow regulators for drug delivery and hydrocephalus treatment," in *Microfluidics, BioMEMS, and Medical Microsystems XII*, SPIE, Mar. 2014, p. 89760S. doi: 10.1117/12.2036084.

[12]   H. Yamada, G. Wennmacher, T. Muto, and Y. Suematsu, "Development of a high-speed on/off digital valve for hydraulic control systems using a multilayered pzt actuator," *International Journal of Fluid Power*, vol. 1, no. 2, pp. 5–10, 2000, doi: 10.1080/14399776.2000.10781087.

[13]   H. Hartshorne, C. J. Backhouse, and W. E. Lee, "Ferrofluid-based microchip pump and valve," *Sens Actuators B Chem*, vol. 99, no. 2–3, pp. 592–600, May 2004, doi: 10.1016/J.SNB.2004.01.016.

[14]   S. P.L, "Valve Handbook," *J Chem Inf Model*, vol. 53, no. 9, pp. 1689–1699, 2013, doi: 10.1036/0071437738.

[15]   T. Pan, S. J. McDonald, E. M. Kai, and B. Ziaie, "A magnetically driven PDMS micropump with ball check-valves," *Journal of Micromechanics and Microengineering*, vol. 15, no. 5, pp. 1021–1026, May 2005, doi: 10.1088/0960-1317/15/5/018.

[16]   C. Fu, Z. Rummler, and W. Schomburg, "Magnetically driven micro ball valves fabricated by multilayer adhesive film bonding INSTITUTE OF PHYSICS PUBLISHING JOURNAL

OF MICROMECHANICS AND MICROENGINEERING Magnetically driven micro ball valves fabricated by multilayer adhesive film bonding," 2003. [Online]. Available: http://iopscience.iop.org/0960-1317/13/4/316

[17] M. C. Hsu, A. Alfadhel, F. Forouzandeh, and D. A. Borkholder, "Biocompatible magnetic nanocomposite microcapsules as microfluidic one-way diffusion blocking valves with ultra-low opening pressure," *Mater Des*, vol. 150, pp. 86–93, 2018, doi: 10.1016/j.matdes.2018.04.024.

[18] D. Y. Sim, T. Kurabayashi, and M. Esashi, "An electrostatically actuated gas valve with an S-shaped film element Related content A bakable microvalve with a Kovar-glass-silicon-glass structure Printed in the UK," 1994.

[19] K. Sato and M. Shikida, "An electrostatically actuated gas valve with an S-shaped film element," *Journal of Micromechanics and Microengineering*, vol. 4, no. 4, pp. 205–209, 1994, doi: 10.1088/0960-1317/4/4/005.

[20] X. Wu, S. H. Kim, C. H. Ji, and M. G. Allen, "A piezoelectrically-driven high flow rate axial polymer microvalve with solid hydraulic amplification," *Proceedings of the IEEE International Conference on Micro Electro Mechanical Systems (MEMS)*, pp. 523–526, 2008, doi: 10.1109/MEMSYS.2008.4443708.

[21] D. C. Roberts, N. W. Hagood, Y. Su, H. Li, and J. A. Carretero, "Design of a Piezoelectrically-Driven Hydraulic Amplification Microvalve for High Pressure, High Frequency Applications," *Proceedings of SPIE*, vol. 3985, no. 617, 2000, doi: 10.1117/12.388857.

[22] T. Watanabe and H. Kuwano, "A microvalve matrix using piezoelectric actuators," Springer-Verlag, 1997.

[23] X. Wu, S. H. Kim, C. H. Ji, and M. G. Allen, "A solid hydraulically amplified piezoelectric microvalve," *Journal of Micromechanics and Microengineering*, vol. 21, no. 9, 2011, doi: 10.1088/0960-1317/21/9/095003.

[24] M. Nafea, A. Nawabjan, and M. S. Mohamed Ali, "A wirelessly-controlled piezoelectric microvalve for regulated drug delivery," *Sens Actuators A Phys*, vol. 279, pp. 191–203, Aug. 2018, doi: 10.1016/j.sna.2018.06.020.

[25] D. C. Roberts *et al.*, "A piezoelectric microvalve for compact high-frequency, high-differential pressure hydraulic micropumping systems," *Journal of Microelectromechanical Systems*, vol. 12, no. 1, pp. 81–92, Feb. 2003, doi: 10.1109/JMEMS.2002.807471.

[26] P. S. Chee, M. N. Minjal, P. L. Leow, and M. S. M. Ali, "Wireless powered thermo-pneumatic micropump using frequency-controlled heater," *Sens Actuators A Phys*, vol. 233, pp. 1–8, Jun. 2015, doi: 10.1016/j.sna.2015.06.017.

[27] H. Takao, K. Miyamura, H. Ebi, M. Ashiki, K. Sawada, and M. Ishida, "A MEMS microvalve with PDMS diaphragm and two-chamber configuration of thermo-pneumatic actuator for integrated blood test system on silicon," *Sens Actuators A Phys*, vol. 119, no. 2, pp. 468–475, Apr. 2005, doi: 10.1016/j.sna.2004.10.023.

[28] C. Das and F. Payne, "Design and characterization of low power, low dead volume electrochemically-driven microvalve," *Sens Actuators A Phys*, vol. 241, pp. 104–112, Apr. 2016, doi: 10.1016/j.sna.2016.01.038.

[29] T. Watanabe, G. C. Biswas, E. T. Carlen, and H. Suzuki, "An autonomous electrochemically-actuated microvalve for controlled transport in stand-alone microfluidic systems," *RSC Adv*, vol. 7, no. 62, pp. 39018–39023, 2017, doi: 10.1039/c7ra07335f.

[30] C. R. Neagqa, J. G. E. Gardienerqa, M. Elwenspoek, and J. J. Kellyb, "An electrochemical active valve," 1997.

[31] D. E. Lee, S. Soper, and W. Wang, "Design and fabrication of an electrochemically actuated microvalve," in *Microsystem Technologies*, Oct. 2008, pp. 1751–1756. doi: 10.1007/s00542-008-0594-3.

[32] D. Kim, Y. W. Hwang, and S. J. Park, "Passive microfluidic gas valves using capillary pressure," *Microsystem Technologies*, vol. 15, no. 6, pp. 919–923, Jun. 2009, doi: 10.1007/s00542-009-0826-1.

[33] B. Li, L. Zhang, S. Bai, J. Jin, and H. Chen, "A brief overview of passive microvalves in microfluidics: Mechanism, manufacturing, and applications," Mar. 01, 2024, *American Institute of Physics*. doi: 10.1063/5.0188807.

[34] C. L. Stevenson, J. T. Santini, and R. Langer, "Reservoir-based drug delivery systems utilizing microtechnology," Nov. 2012. doi: 10.1016/j.addr.2012.02.005.

[35] M. M. Sadeghi, H. S. Kim, R. L. B. Peterson, and K. Najafi, "Electrostatic Micro-Hydraulic Systems," *Journal of Microelectromechanical Systems*, vol. 25, no. 3, pp. 557–569, 2016, doi: 10.1109/JMEMS.2016.2552141.

[36] J. Fong, Z. Xiao, and K. Takahata, "Wireless implantable chip with integrated nitinol-based pump for radio-controlled local drug delivery," *Lab Chip*, vol. 15, no. 4, pp. 1050–1058, Feb. 2015, doi: 10.1039/c4lc01290a.

[37] T. Li, A. T. Evans, S. Chiravuri, R. Y. Gianchandani, and Y. B. Gianchandani, "Compact, power-efficient architectures using microvalves and microsensors, for intrathecal, insulin, and other drug delivery systems," *Adv Drug Deliv Rev*, vol. 64, no. 14, pp. 1639–1649, 2012, doi: 10.1016/j.addr.2012.05.002.

[38]   F. Forouzandeh *et al.*, "A nanoliter resolution implantable micropump for murine inner ear drug delivery," *Journal of Controlled Release*, vol. 298, no. January, pp. 27–37, 2019, doi: 10.1016/j.jconrel.2019.01.032.

[39]   E. Stemme and G. Stemme, "A valveless diffuser/nozzle-based fluid pump," *Sens Actuators A Phys*, vol. 39, no. 2, pp. 159–167, Nov. 1993, doi: 10.1016/0924-4247(93)80213-Z.

[40]   A. T. Evans *et al.*, "A low power, microvalve-regulated drug delivery system using a SI micro-spring pressurized balloon reservoir," in *TRANSDUCERS and EUROSENSORS '07 - 4th International Conference on Solid-State Sensors, Actuators and Microsystems*, 2007, pp. 359–362. doi: 10.1109/SENSOR.2007.4300142.

[41]   A. T. Evans, J. M. Park, S. Chiravuri, and Y. B. Gianchandani, "A low power, microvalve regulated architecture for drug delivery systems," *Biomed Microdevices*, vol. 12, no. 1, pp. 159–168, 2010, doi: 10.1007/s10544-009-9372-y.

[42]   G. M. Walker and D. J. Beebe, "A passive pumping method for microfluidic devices," *Lab Chip*, vol. 2, no. 3, pp. 131–134, 2002, doi: 10.1039/b204381e.

[43]   A. Javadi, M. Habibi, F. S. Taheri, S. Moulinet, and D. Bonn, "Effect of wetting on capillary pumping in microchannels," *Sci Rep*, vol. 3, pp. 1–6, 2013, doi: 10.1038/srep01412.

[44]   M. S. Groen, *Microvalves for precise dosing*. 2015. doi: 10.3990/1.9789036539616.

[45]   M. S. Groen, D. M. Brouwer, R. J. Wiegerink, and J. C. Lötters, "Design considerations for a micromachined proportional control valve," *Micromachines (Basel)*, vol. 3, no. 2, pp. 396–412, 2012, doi: 10.3390/mi3020396.

[46]   Y. T. Kim, B. Kuczenski, P. R. Leduc, and W. C. Messner, "Modulation of fluidic resistance and capacitance for long-term, high-speed feedback control of a microfluidic interface," *Lab Chip*, vol. 9, no. 17, pp. 2603–2609, 2009, doi: 10.1039/b822423d.

[47]   I. Fazal, M. C. Louwerse, H. V. Jansen, and M. C. Elwenspoek, "Design, fabrication and characterization of a novel gas microvalve using micro- and fine-machining," *Journal of Micromechanics and Microengineering*, vol. 16, no. 7, pp. 1207–1214, Jul. 2006, doi: 10.1088/0960-1317/16/7/013.

[48]   A. K. Henning, "Compact pressure- and structure-based gas flow model for microvalves," *Materials and Device Characterization in Micromachining III*, vol. 4175, no. May, p. 74, 2000, doi: 10.1117/12.395614.

[49]   A. Debray *et al.*, "A micro-machined safety valve for power applications with improved sealing," *Journal of Micromechanics and Microengineering*, vol. 16, no. 9, Sep. 2006, doi: 10.1088/0960-1317/16/9/S11.

[50]   D. J. Laser and J. G. Santiago, "A review of micropumps," *Journal of Micromechanics and Microengineering*, vol. 14, no. 6, 2004, doi: 10.1088/0960-1317/14/6/R01.

[51]   Y. N. Wang and L. M. Fu, "Micropumps and biomedical applications – A review," Aug. 05, 2018, *Elsevier B.V.* doi: 10.1016/j.mee.2018.04.008.

[52]   H. T. Nguyen, H. Thach, E. Roy, K. Huynh, and C. M. T. Perrault, "Low-cost, accessible fabrication methods for microfluidics research in low-resource settings," *Micromachines (Basel)*, vol. 9, no. 9, 2018, doi: 10.3390/mi9090461.

[53]   E. W. K. Young and D. J. Beebe, "Fundamentals of microfluidic cell culture in controlled microenvironments," *Chem Soc Rev*, vol. 39, no. 3, pp. 1036–1048, Feb. 2010, doi: 10.1039/b909900j.

[54]   J. G. DeStefano, A. Williams, A. Wnorowski, N. Yimam, P. C. Searson, and A. D. Wong, "Real-time quantification of endothelial response to shear stress and vascular modulators,"

Integrative Biology (United Kingdom), vol. 9, no. 4, pp. 362–374, Apr. 2017, doi: 10.1039/c7ib00023e.

[55] R. Sinha, S. Le Gac, N. Verdonschot, A. Van Den Berg, B. Koopman, and J. Rouwkema, "Endothelial cell alignment as a result of anisotropic strain and flow induced shear stress combinations," *Sci Rep*, vol. 6, Jul. 2016, doi: 10.1038/srep29510.

[56] I. E. Araci, M. Robles, and S. R. Quake, "A reusable microfluidic device provides continuous measurement capability and improves the detection limit of digital biology," *Lab Chip*, vol. 16, no. 9, pp. 1573–1578, Apr. 2016, doi: 10.1039/C6LC00194G.

[57] A. Koh *et al.*, "A soft, wearable microfluidic device for the capture, storage, and colorimetric sensing of sweat.," *Sci Transl Med*, vol. 8, no. 366, p. 366ra165, Nov. 2016, doi: 10.1126/scitranslmed.aaf2593.

[58] W. Zhao, R. Cheng, J. R. Miller, and L. Mao, "Label-Free Microfluidic Manipulation of Particles and Cells in Magnetic Liquids," *Adv Funct Mater*, vol. 26, no. 22, pp. 3916–3932, Jun. 2016, doi: 10.1002/adfm.201504178.

[59] S. M. Yoo and S. Y. Lee, "Optical Biosensors for the Detection of Pathogenic Microorganisms," *Trends Biotechnol*, vol. 34, no. 1, pp. 7–25, Jan. 2016, doi: 10.1016/j.tibtech.2015.09.012.

[60] B. Xue *et al.*, "Electrically Controllable Actuators Based on Supramolecular Peptide Hydrogels," *Adv Funct Mater*, vol. 26, no. 48, pp. 9053–9062, Dec. 2016, doi: 10.1002/adfm.201603947.

[61] D. G. Johnson, M. J. Waldron, R. D. Frisina, and D. A. Borkholder, "Implantable micropump technologies for murine intracochlear infusions," in *2010 Annual International*

Conference of the IEEE Engineering in Medicine and Biology, IEEE, Aug. 2010, pp. 6441–6444. doi: 10.1109/IEMBS.2010.5627335.

[62]   D. Mark, S. Haeberle, G. Roth, F. von Stetten, and R. Zengerle, "Microfluidic lab-on-a-chip platforms: requirements, characteristics and applications," *Chem Soc Rev*, vol. 39, no. 3, p. 1153, Feb. 2010, doi: 10.1039/b820557b.

[63]   S. Xu *et al.*, "Soft microfluidic assemblies of sensors, circuits, and radios for the skin," *Science (1979)*, vol. 344, no. 6179, pp. 70–74, 2014, doi: 10.1126/science.1250169.

[64]   R. Lo, P.-Y. Li, S. Saati, R. N. Agrawal, M. S. Humayun, and E. Meng, "A passive MEMS drug delivery pump for treatment of ocular diseases," *Biomed Microdevices*, vol. 11, no. 5, pp. 959–970, Oct. 2009, doi: 10.1007/s10544-009-9313-9.

[65]   K. Yanagisawa, H. Kuwano, and A. Tago, "Electromagetically driven microvalve," *Microsystem Technologies*, vol. 2, no. 1, pp. 22–25, 1995, doi: 10.1007/BF02739524.

[66]   B. Bae *et al.*, "In vitro experiment of the pressure regulating valve for a glaucoma implant," 2003.

[67]   K. W. Oh, R. Rong, and C. H. Ahn, "Miniaturization of pinch-type valves and pumps for practical micro total analysis system integration," *Journal of Micromechanics and Microengineering*, vol. 15, no. 12, pp. 2449–2455, Dec. 2005, doi: 10.1088/0960-1317/15/12/029.

[68]   J.-W. Choi *et al.*, "Development and Characterization of Micro¯uidic Devices and Systems for Magnetic Bead-Based Biochemical Detection," 2001.

[69]   M. P. Chang and M. M. Maharbiz, "Electrostatically-driven elastomer components for user-reconfigurable high density microfluidics," *Lab Chip*, vol. 9, no. 9, pp. 1274–1281, 2009, doi: 10.1039/b813244e.

[70] E. Yıldırım, M. A. S. Arikan, and H. Külah, "A normally closed electrostatic parylene microvalve for micro total analysis systems," *Sens Actuators A Phys*, vol. 181, pp. 81–86, Jul. 2012, doi: 10.1016/j.sna.2012.05.008.

[71] T. Rogge, Z. Rummler, and W. K. Schomburg, "Polymer micro valve with a hydraulic piezo-drive fabricated by the AMANDA process," in *Sensors and Actuators, A: Physical*, Feb. 2004, pp. 206–212. doi: 10.1016/j.sna.2003.10.056.

[72] J. Xie, J. Shih, and Y.-C. Tai, "INTEGRATED SURFACE-MICROMACHINED MASS FLOW CONTROLLER."

[73] J. Peirs, D. Reynaerts, and H. Van Brussel, "Design of miniature parallel manipulators for integration in a self-propelling endoscope," 2000. [Online]. Available: www.elsevier.nlrlocatersna

[74] G. Waibel *et al.*, "Highly integrated autonomous microdosage system," *Sens Actuators A Phys*, vol. 103, no. 1–2, pp. 225–230, 2003, doi: 10.1016/S0924-4247(02)00349-7.

[75] S. Chen *et al.*, "A normally-closed piezoelectric micro-valve with flexible stopper," *AIP Adv*, vol. 6, no. 4, Apr. 2016, doi: 10.1063/1.4947301.

[76] S. K. Baek, Y. K. Yoon, H. S. Jeon, S. Seo, and J. H. Park, "A wireless sequentially actuated microvalve system," *Journal of Micromechanics and Microengineering*, vol. 23, no. 4, Apr. 2013, doi: 10.1088/0960-1317/23/4/045006.

[77] C. M. Pemble and B. C. Towe, "Miniature shape memory alloy pinch valve," *Sens Actuators A Phys*, vol. 77, no. 2, pp. 145–148, 1999, doi: 10.1016/S0924-4247(99)00157-0.

[78] K. A. Shaikh, S. Li, and C. Liu, "Development of a latchable microvalve employing a low-melting-temperature metal alloy," *Journal of Microelectromechanical Systems*, vol. 17, no. 5, pp. 1195–1203, 2008, doi: 10.1109/JMEMS.2008.2003055.

[79]   M. M. Sadeghi, H. S. Kim, R. L. B. Peterson, and K. Najafi, "Electrostatic Micro-Hydraulic

Systems," *Journal of Microelectromechanical Systems*, vol. 25, no. 3, pp. 557–569, 2016,

doi: 10.1109/JMEMS.2016.2552141.

[80]   A. T. Evans, S. Chiravuri, and Y. B. Gianchandani, "A multidrug delivery system using a

piezoelectrically actuated silicon valve manifold with embedded sensors," *Journal of

Microelectromechanical Systems*, vol. 20, no. 1, pp. 231–238, 2011, doi:

10.1109/JMEMS.2010.2093566.

[81]   I. Fazal, M. Louwerse, H. Jansen, and M. Elwenspoek, "Stepper motor actuated microvalve,"

J Phys Conf Ser, vol. 34, no. 1, pp. 1032–1037, Apr. 2006, doi: 10.1088/1742-

6596/34/1/171.

[82]   I. Fazal, M. C. Louwerse, H. V. Jansen, and M. C. Elwenspoek, "Design, fabrication and

characterization of a novel gas microvalve using micro- and fine-machining," *Journal of

Micromechanics and Microengineering*, vol. 16, no. 7, pp. 1207–1214, Jul. 2006, doi:

10.1088/0960-1317/16/7/013.

[83]   A. Gunda, G. Özkayar, M. Tichem, and M. K. Ghatkesar, "Proportional microvalve using

a unimorph piezoelectric microactuator," *Micromachines (Basel)*, vol. 11, no. 2, Feb. 2020,

doi: 10.3390/mi11020130.

[84]   X. Liu and S. Li, "An Electromagnetic Microvalve for Pneumatic Control of Microfluidic

Systems," *J Lab Autom*, vol. 19, no. 5, pp. 444–453, Oct. 2014, doi:

10.1177/2211068214531760.

[85]   X. Liu and S. Li, "Control method experimental research of micro chamber air pressure via

a novel electromagnetic microvalve," in *Proceedings - 2017 4th International Conference*

on Information Science and Control Engineering, ICISCE 2017, Institute of Electrical and Electronics Engineers Inc., Nov. 2017, pp. 921–925. doi: 10.1109/ICISCE.2017.195.

[86] D. Bosch, B. Heimhofer, G. Mück, H. Seidel, U. Thumser, and W. Welser, "A silicon microvalve with combined electromagnetic/electrostatic actuation," *Sens Actuators A Phys*, vol. 37–38, no. C, pp. 684–692, 1993, doi: 10.1016/0924-4247(93)80116-X.

[87] A. Alfadhel and J. Kosel, "Magnetic Nanocomposite Cilia Tactile Sensor," *Advanced Materials*, vol. 27, no. 47, pp. 7888–7892, Dec. 2015, doi: 10.1002/adma.201504015.

[88] E. I. Paschalis, J. Chodosh, R. A. Sperling, B. Salvador-Culla, and C. Dohlman, "A Novel Implantable Glaucoma Valve Using Ferrofluid," *PLoS One*, vol. 8, no. 6, p. e67404, Jun. 2013, doi: 10.1371/journal.pone.0067404.

[89] R. Sheybani, A. Cobo, and E. Meng, "Wireless programmable electrochemical drug delivery micropump with fully integrated electrochemical dosing sensors," *Biomed Microdevices*, vol. 17, no. 4, pp. 1–13, 2015, doi: 10.1007/s10544-015-9980-7.

[90] P. W. Barth, "Silicon microvalves for gas flow control," pp. 276–279, 1995.

[91] D. Reynaerts, J. Peirs, and H. Van Brussel, "a Sma-Actuated Implantable System for Delivery of Liquid Drugs," *5th International Conference on New Actuators*, no. June, pp. 26–28, 1996.

[92] A. Debray *et al.*, "A micro-machined safety valve for power applications with improved sealing," *Journal of Micromechanics and Microengineering*, vol. 16, no. 9, 2006, doi: 10.1088/0960-1317/16/9/S11.

[93] C. G. Cooney and B. C. Towe, "A thermopneumatic dispensing micropump," *Sens Actuators A Phys*, vol. 116, no. 3, pp. 519–524, 2004, doi: 10.1016/j.sna.2004.05.015.

[94] E. Stemme and G. Stemme, "A valveless diffuser/nozzle-based fluid pump," *Sens Actuators A Phys*, vol. 39, no. 2, pp. 159–167, Nov. 1993, doi: 10.1016/0924-4247(93)80213-Z.

[95] T.-S. Leu and P.-Y. Chang, "Pressure barrier of capillary stop valves in micro sample separators," *Sens Actuators A Phys*, vol. 115, no. 2–3, pp. 508–515, Sep. 2004, doi: 10.1016/J.SNA.2004.02.036.

[96] H. Andersson, W. van der Wijngaart, P. Griss, F. Niklaus, and G. Stemme, "Hydrophobic valves of plasma deposited octafluorocyclobutane in DRIE channels," *Sens Actuators B Chem*, vol. 75, no. 1–2, pp. 136–141, Apr. 2001, doi: 10.1016/S0925-4005(00)00675-4.

[97] H. Andersson, W. van der Wijngaart, and G. Stemme, "Micromachined filter-chamber array with passive valves for biochemical assays on beads," *Electrophoresis*, vol. 22, no. 2, pp. 249–257, Jan. 2001, doi: 10.1002/1522-2683(200101)22:2<249::AID-ELPS249>3.0.CO;2-4.

[98] W. Y. Sim, H. J. Yoon, O. C. Jeong, and S. S. Yang, "A phase-change type micropump with aluminum flap valves," *Journal of Micromechanics and Microengineering*, vol. 13, no. 2, pp. 286–294, Mar. 2003, doi: 10.1088/0960-1317/13/2/317.

[99] C.-J. Park, D.-S. Yang, J.-J. Cha, and J.-H. Lee, "Polymeric check valve with an elevated pedestal for precise cracking pressure in a glaucoma drainage device," *Biomed Microdevices*, vol. 18, no. 1, p. 20, Feb. 2016, doi: 10.1007/s10544-016-0048-0.

[100] V. Narayanamurthy *et al.*, "Advances in passively driven microfluidics and lab-on-chip devices: A comprehensive literature review and patent analysis," *RSC Adv*, vol. 10, no. 20, pp. 11652–11680, Mar. 2020, doi: 10.1039/d0ra00263a.

[101] C. H. Mastrangelo, "Suppression of stiction in MEMS," *Materials Research Society Symposium - Proceedings*, vol. 605, pp. 105–116, 2000, doi: 10.1557/proc-605-105.

[102] T. K. Jain, M. K. Reddy, M. A. Morales, D. L. Leslie-Pelecky, and V. Labhasetwar, "Biodistribution, Clearance, and Biocompatibility of Iron Oxide Magnetic Nanoparticles in Rats," *Mol Pharm*, vol. 5, no. 2, pp. 316–327, Apr. 2008, doi: 10.1021/mp7001285.

[103] X. Y. Liu, J. M. Nothias, A. Scavone, M. Garfinkel, and J. M. Millis, "Biocompatibility investigation of polyethylene glycol and alginate-poly-l-lysine for islet encapsulation," *ASAIO Journal*, vol. 56, no. 3, pp. 241–245, 2010, doi: 10.1097/MAT.0b013e3181d7b8e3.

[104] J. S. Song, S. Lee, S. H. Jung, G. C. Cha, and M. S. Mun, "Improved biocompatibility of parylene-C films prepared by chemical vapor deposition and the subsequent plasma treatment," *J Appl Polym Sci*, vol. 112, no. 6, pp. 3677–3685, Jun. 2009, doi: 10.1002/app.29774.

[105] J. S. Song, S. Lee, S. H. Jung, G. C. Cha, and M. S. Mun, "Improved biocompatibility of parylene-C films prepared by chemical vapor deposition and the subsequent plasma treatment," *J Appl Polym Sci*, vol. 112, no. 6, pp. 3677–3685, Jun. 2009, doi: 10.1002/app.29774.

[106] R. Inamoto, T. Miyashita, K. Akiyama, T. Mori, and N. Mori, "Endolymphatic sac is involved in the regulation of hydrostatic pressure of cochlear endolymph," *American Journal of Physiology-Regulatory, Integrative and Comparative Physiology*, vol. 297, no. 5, pp. R1610–R1614, Nov. 2009, doi: 10.1152/ajpregu.00073.2009.

[107] A. K. Gaigalas, L. L. Wang, A. Schwartz, G. E. Marti, and R. F. Vogt, "Quantitating fluorescence intensity from fluorophore: Assignment of MESF values," *J Res Natl Inst Stand Technol*, vol. 110, no. 2, p. 101, Mar. 2005, doi: 10.6028/jres.110.010.

[108] W. Zeng, I. Jacobi, D. J. Beck, S. Li, and H. A. Stone, "Characterization of syringe-pump-driven induced pressure fluctuations in elastic microchannels," *Lab Chip*, vol. 15, no. 4, pp. 1110–1115, 2015, doi: 10.1039/c4lc01347f.

[109] K. W. Bong, S. C. Chapin, D. C. Pregibon, D. Baah, T. M. Floyd-Smith, and P. S. Doyle, "Compressed-air flow control system," *Lab Chip*, vol. 11, no. 4, pp. 743–747, Feb. 2011, doi: 10.1039/c0lc00303d.

[110] T. Ward, M. Faivre, M. Abkarian, and H. A. Stone, "Microfluidic flow focusing: Drop size and scaling in pressure versus flow-rate-driven pumping," *Electrophoresis*, vol. 26, no. 19, pp. 3716–3724, 2005, doi: 10.1002/elps.200500173.

[111] C. K. Byun, K. Abi-Samra, Y. K. Cho, and S. Takayama, "Pumps for microfluidic cell culture," Feb. 01, 2014, *Wiley-VCH Verlag*. doi: 10.1002/elps.201300205.

[112] L. P. Pardo, M. A. S. Peterlini, L. N. Tume, and M. L. G. Pedreira, "Impact of different syringe pumps on red cells during paediatric simulated transfusion," *Nurs Crit Care*, 2020, doi: 10.1111/nicc.12561.

[113] F. Kurth *et al.*, "Organs-on-a-chip engineering," in *Organ-on-a-chip: Engineered Microenvironments for Safety and Efficacy Testing*, Elsevier, 2019, pp. 47–130. doi: 10.1016/B978-0-12-817202-5.00003-6.

[114] D. Kusahara, M. Pedreira, A. Avelar, and M. Peterlini, "Performance of a linear peristaltic infusion pump during red blood cells administration and the influence of infusion rates," *Intensive Care Med Exp*, vol. 3, no. S1, Dec. 2015, doi: 10.1186/2197-425x-3-s1-a548.

[115] X. Wang, C. Cheng, S. Wang, and S. Liu, "Electroosmotic pumps and their applications in microfluidic systems," 2009. doi: 10.1007/s10404-008-0399-9.

[116] N. Aoki and K. Mae, "Effects of channel geometry on mixing performance of micromixers using collision of fluid segments," *Chemical Engineering Journal*, vol. 118, no. 3, pp. 189–197, May 2006, doi: 10.1016/j.cej.2006.02.011.

[117] D. Dutta, A. Ramachandran, and D. T. Leighton, "Effect of channel geometry on solute dispersion in pressure-driven microfluidic systems," Jul. 2006. doi: 10.1007/s10404-005-0070-7.

[118] P. Thurgood *et al.*, "A self-sufficient micro-droplet generation system using highly porous elastomeric sponges: A versatile tool for conducting cellular assays," *Sens Actuators B Chem*, vol. 274, pp. 645–653, Nov. 2018, doi: 10.1016/j.snb.2018.07.168.

[119] P. Thurgood *et al.*, "Self-sufficient, low-cost microfluidic pumps utilising reinforced balloons," *Lab Chip*, vol. 19, no. 17, pp. 2885–2896, 2019, doi: 10.1039/c9lc00618d.

[120] X. Wang, D. T. T. Phan, D. Zhao, S. C. George, C. C. W. Hughes, and A. P. Lee, "An on-chip microfluidic pressure regulator that facilitates reproducible loading of cells and hydrogels into microphysiological system platforms," *Lab Chip*, vol. 16, no. 5, pp. 868–876, 2016, doi: 10.1039/c5lc01563d.

[121] M. Marimuthu and S. Kim, "Pumpless steady-flow microfluidic chip for cell culture," *Anal Biochem*, vol. 437, no. 2, pp. 161–163, Jun. 2013, doi: 10.1016/j.ab.2013.02.007.

[122] N. Sasaki *et al.*, "A palmtop-sized microfluidic cell culture system driven by a miniaturized infusion pump," *Electrophoresis*, vol. 33, no. 12, pp. 1729–1735, Jul. 2012, doi: 10.1002/elps.201100691.

[123] G. S. Jeong *et al.*, "Siphon-driven microfluidic passive pump with a yarn flow resistance controller," *Lab Chip*, vol. 14, no. 21, pp. 4213–4219, Nov. 2014, doi: 10.1039/c4lc00510d.

[124] E.-C. Yeh, C.-C. Fu, L. Hu, R. Thakur, J. Feng, and L. P. Lee, "Self-powered integrated microfluidic point-of-care low-cost enabling (SIMPLE) chip," *Sci Adv*, vol. 3, no. 3, Mar. 2017, doi: 10.1126/sciadv.1501645.

[125] A. Podwin, R. Walczak, and J. Dziuban, "A 3D printed membrane-based gas microflow regulator for on-chip cell culture," *Applied Sciences (Switzerland)*, vol. 8, no. 4, Apr. 2018, doi: 10.3390/app8040579.

[126] K. W. Bong, S. C. Chapin, D. C. Pregibon, D. Baah, T. M. Floyd-Smith, and P. S. Doyle, "Compressed-air flow control system," *Lab Chip*, vol. 11, no. 4, pp. 743–747, Feb. 2011, doi: 10.1039/c0lc00303d.

[127] M. Kudasik, N. Skoczylas, J. Sobczyk, and J. Topolnicki, "Manostat - An accurate gas pressure regulator," *Meas Sci Technol*, vol. 21, no. 8, 2010, doi: 10.1088/0957-0233/21/8/085402.

[128] D. Anjewierden, G. A. Liddiard, and B. K. Gale, "An electrostatic microvalve for pneumatic control of microfluidic systems," *Journal of Micromechanics and Microengineering*, vol. 22, no. 2, Feb. 2012, doi: 10.1088/0960-1317/22/2/025019.

[129] K. Yoshida, S. Tanaka, Y. Hagihara, S. Tomonari, and M. Esashi, "Normally closed electrostatic microvalve with pressure balance mechanism for portable fuel cell application," *Sens Actuators A Phys*, vol. 157, no. 2, pp. 290–298, Feb. 2010, doi: 10.1016/j.sna.2009.11.030.

[130] S. Begolo, D. V. Zhukov, D. A. Selck, L. Li, and R. F. Ismagilov, "The pumping lid: Investigating multi-material 3D printing for equipment-free, programmable generation of positive and negative pressures for microfluidic applications," *Lab Chip*, vol. 14, no. 24, pp. 4616–4628, Dec. 2014, doi: 10.1039/c4lc00910j.

[131] "Beswick Engineering Pressure Regulator." [Online]. Available: https://www.beswick.com/catalog/product-category/regulators/

[132] N. Mavrogiannis, M. Ibo, X. Fu, F. Crivellari, and Z. Gagnon, "Microfluidics made easy: A robust low-cost constant pressure flow controller for engineers and cell biologists," *Biomicrofluidics*, vol. 10, no. 3, May 2016, doi: 10.1063/1.4950753.

[133] M.-C. Hsu *et al.*, "A miniaturized 3D printed pressure regulator (µPR) for microfluidic cell culture applications," *Sci Rep*, vol. 12, no. 1, 2022, doi: 10.1038/s41598-022-15087-9.

[134] P. Thurgood *et al.*, "Self-sufficient, low-cost microfluidic pumps utilising reinforced balloons," *Lab Chip*, vol. 19, no. 17, pp. 2885–2896, Sep. 2019, doi: 10.1039/c9lc00618d.

[135] "Dolomite Mitos Fluika Pump." [Online]. Available: https://www.dolomite-microfluidics.com/product/mitos-fluika-pump/

[136] E. Systems, "Elveflow Microfluidic Flow Controller." [Online]. Available: https://www.elveflow.com/microfluidic-products/microfluidics-flow-control-systems/ob1-pressure-controller/

[137] A. T. Evans, J. M. Park, S. Chiravuri, and Y. B. Gianchandani, "A low power, microvalve regulated architecture for drug delivery systems," *Biomed Microdevices*, vol. 12, no. 1, pp. 159–168, Feb. 2010, doi: 10.1007/s10544-009-9372-y.

[138] A. K. Henning *et al.*, "Microfluidic MEMS for Semiconductor Processing," 1998.

[139] A. Podwin *et al.*, "Lab-on-chip platform for culturing and dynamic evaluation of cells development," *Micromachines (Basel)*, vol. 11, no. 2, pp. 1–11, 2020, doi: 10.3390/mi11020196.

[140] M. Coakley and D. E. Hurt, "3D Printing in the Laboratory: Maximize Time and Funds with Customized and Open-Source Labware," *J Lab Autom*, vol. 21, no. 4, pp. 489–495, Aug. 2016, doi: 10.1177/2211068216649578.

[141] A. Ahmed *et al.*, "Microengineered 3D Collagen Gels with Independently Tunable Fiber Anisotropy and Directionality," *Adv Mater Technol*, vol. 6, no. 4, Apr. 2021, doi: 10.1002/admt.202001186.

[142] V. V. Abhyankar, M. Wu, C. Y. Koh, and A. V. Hatch, "A reversibly sealed, easy access, modular (SEAM) microfluidic architecture to establish in vitro tissue interfaces," *PLoS One*, vol. 11, no. 5, May 2016, doi: 10.1371/journal.pone.0156341.

[143] M. Mansouri *et al.*, "The Modular µSiM Reconfigured: Integration of Microfluidic Capabilities to Study in vitro Barrier Tissue Models under Flow", doi: 10.1101/2022.03.28.486107.

[144] M. C. Mccloskey *et al.*, "The Modular µSiM: a Mass Produced, Rapidly Assembled, and Reconfigurable Platform for the Study of Barrier Tissue Models In Vitro", doi: 10.1101/2022.03.28.486095.

[145] G. W. Melenka, J. S. Schofield, M. R. Dawson, and J. P. Carey, "Evaluation of dimensional accuracy and material properties of the MakerBot 3D desktop printer," *Rapid Prototyp J*, vol. 21, no. 5, pp. 618–627, Aug. 2015, doi: 10.1108/RPJ-09-2013-0093.

[146] F. Menzel, T. Klein, T. Ziegler, and J. M. Neumaier, "3D-printed PEEK reactors and development of a complete continuous flow system for chemical synthesis," *React Chem Eng*, vol. 5, no. 7, pp. 1300–1310, Jul. 2020, doi: 10.1039/d0re00206b.

[147] D. L. Walmsley and E. Sellier, "Design and development of a 3D-printed back-pressure regulator," Dec. 01, 2020, *Nature Publishing Group*. doi: 10.31224/osf.io/3t9bq.

[148] G. Seiffert, C. Hopkins, and C. Sutcliffe, "Comparison of high-intensity sound and mechanical vibration for cleaning porous titanium cylinders fabricated using selective laser melting," *J Biomed Mater Res B Appl Biomater*, vol. 105, no. 1, pp. 117–123, Jan. 2017, doi: 10.1002/jbm.b.33535.

[149] J. H. Sung *et al.*, "Recent Advances in Body-on-a-Chip Systems," Jan. 02, 2019, *American Chemical Society*. doi: 10.1021/acs.analchem.8b05293.

[150] C. M. Leung *et al.*, "A guide to the organ-on-a-chip," Dec. 01, 2022, *Springer Nature*. doi: 10.1038/s43586-022-00118-6.

[151] S. Ahadian *et al.*, "Organ-On-A-Chip Platforms: A Convergence of Advanced Materials, Cells, and Microscale Technologies," Jan. 24, 2018, *Wiley-VCH Verlag*. doi: 10.1002/adhm.201700506.

[152] K. Achberger *et al.*, "Merging organoid and organ-on-a-chip technology to generate complex multi-layer tissue models in a human retina-on-a-chip platform," 2019, doi: 10.7554/eLife.46188.001.

[153] R. F. Monteiro *et al.*, "Writing 3D In Vitro Models of Human Tendon within a Biomimetic Fibrillar Support Platform," Nov. 08, 2023, *American Chemical Society*. doi: 10.1021/acsami.2c22371.

[154] D. Huh, "A human breathing lung-on-a-chip," in *Annals of the American Thoracic Society*, American Thoracic Society, Mar. 2015, pp. S42–S44. doi: 10.1513/AnnalsATS.201410-442MG.

[155] E. M. Shaughnessey, S. H. Kann, H. Azizgolshani, L. D. Black, J. L. Charest, and E. M. Vedula, "Evaluation of rapid transepithelial electrical resistance (TEER) measurement as a

metric of kidney toxicity in a high-throughput microfluidic culture system," *Sci Rep*, vol. 12, no. 1, p. 13182, Aug. 2022, doi: 10.1038/s41598-022-16590-9.

[156] R. Augustine, A. H. Aqel, S. N. Kalva, K. S. Joshy, A. Nayeem, and A. Hasan, "Bioengineered microfluidic blood-brain barrier models in oncology research," Jul. 01, 2021, *Neoplasia Press, Inc.* doi: 10.1016/j.tranon.2021.101087.

[157] R. Booth and H. Kim, "Characterization of a microfluidic in vitro model of the blood-brain barrier (μBBB)," *Lab Chip*, vol. 12, no. 10, pp. 1784–1792, Apr. 2012, doi: 10.1039/c2lc40094d.

[158] D. H. Elbrecht, C. J. Long, and J. J. Hickman, "Transepithelial/endothelial Electrical Resistance (TEER) theory and ap-plications for microfluidic body-on-a-chip devices Keywords TEER Body-on-a-chip Barrier tissue Blood-brain barrier Organ Endothelial cells Epithelial cells Human-on-a-chip," 2016. [Online]. Available: www.rarediseasesjournal.com

[159] M. Mansouri *et al.*, "The Modular μSiM Reconfigured: Integration of Microfluidic Capabilities to Study in vitro Barrier Tissue Models under Flow", doi: 10.1101/2022.03.28.486107.

[160] T. S. Khire *et al.*, "Microvascular Mimetics for the Study of Leukocyte–Endothelial Interactions," *Cell Mol Bioeng*, vol. 13, no. 2, pp. 125–139, Apr. 2020, doi: 10.1007/s12195-020-00611-6.